Thin-film Silicon Solar Cells—Photonic Design, Process and Fundamentals

by

Xing Sheng

B.E., Tsinghua University (2007)

Submitted to the Department of Materials Science and Engineering
on December 20, 2011, in partial fulfillment of the requirements for the degree of

Doctor of Philosophy in Electronic, Photonic and Magnetic Materials

at the

MASSACHUSETTS INSTITUTE OF TECHNOLOGY

February 2012

Author .....
Department of Materials Science and Engineering
December 20, 2011

Certified by .....
Lionel C. Kimerling
Thomas Lord Professor of Materials Science and Engineering
Thesis Supervisor

Accepted by .....
Gerbrand Ceder
Chair, Departmental Committee on Graduate Students

Thin-film Silicon Solar Cells—Photonic Design, Process and Fundamentals

by

Xing Sheng

Submitted to the Department of Materials Science and Engineering
on December 20, 2011, in partial fulfillment of the
requirements for the degree of
Doctor of Philosophy in Electronic, Photonic and Magnetic Materials

Abstract

The photovoltaic technology has been attracting widespread attention because of its effective energy harvest by directly converting solar energy into electricity. Thin-film silicon solar cells are believed to be a promising candidate for further scaled-up production and cost reduction while maintaining the advantages of bulk silicon. The efficiency of thin-film Si solar cells critically depends on optical absorption in the silicon layer since silicon has low absorption coefficient in the red and near-infrared (IR) wavelength ranges due to its indirect bandgap nature. This thesis aims at understanding, designing, and fabricating novel photonic structures for efficiency enhancement in thin-film Si solar cells.

We have explored a previously reported a photonic crystal (PC) based structure to improve light absorption in thin-film Si solar cells. The PC structure combines a dielectric grating layer and a distributed Bragg reflector (DBR) for efficient light scattering and reflection, increasing light path length in the thin-film cell. We have understood the operation principles for this design by using photonic band theories and electromagnetic wave simulations. we discover that this DBR with gratings exhibit unusual light trapping in a way different from metal reflectors and photonic crystals. The light trapping effects for the DBR with and without reflector are numerically investigated.

The self-assembled anodic aluminum oxide (AAO) technique is introduced to non-lithographically fabricate the grating structure. We adjust the AAO structural parameters by using different anodization voltages, times and electrolytes. Two-step anodization is employed to obtain nearly hexagonal AAO pattern. The interpore periods of the fabricated AAO are calculated by fast Fourier transform (FFT) analysis. We have also demonstrated the fabrication of ordered patterns made of other materials like amorphous Si (a-Si) and silver by using the AAO membrane as a deposition mask. Numerical simulations predict that the fabricated AAO pattern exhibits light trapping performance comparable to the perfectly periodic grating layer.

We have implemented the light trapping concepts combining the self-assembled AAO layer and the DBR in the backside of crystalline Si wafers. Photoconductivity measurements suggest that the light absorption is improved in the near-IR spectral range near the band edge of Si. Furthermore, different types of thin-film Si solar cells, including a-Si, microcrystalline Si (μc-Si) and micromorph Si solar cells, are investigated. For demonstration, the designed structure is integrated into a 1.5 μm thick μc-Si solar cell. We use numerical simulations to obtain the optimal structure parameters for the grating and the DBR, and then we fabricate the optimized structures using the AAO membrane as a template. The

prototype devices integrating our proposed backside structure yield a 21% improvement in efficiency. This is further verified by quantum efficiency measurements, which clearly indicate stronger light absorption in the red and near-IR spectral ranges.

Lastly, we have explored the fundamental light trapping limits for thin-film Si solar cells in the wave optics regime. We develop a deterministic method to optimize periodic textures for light trapping. Deep and high-index-contrast textures exhibit strong anisotropic scattering that is outside the regime of validity of the Lambertian models commonly used to describe texture-induced absorption enhancement for normal incidence. In the weak absorption regime, our optimized surface texture in two dimensions (2D) enhances absorption by a factor of $2.7\pi n$, considerably larger than the classical πn Lambertian result and exceeding by almost 50% a recent generalization of Lambertian model for periodic structures in finite spectral range. Since the πn Lambertian limit still applies for isotropic incident light, our optimization methodology can be thought of optimizing the angle/enhancement tradeoff for periodic textures. Based on a modified Shockley-Queisser theory, we conclude that it is possible to achieve more than 20% efficiency in a 1.5 μm thick crystalline Si cell if advanced light trapping schemes can be realized.

Thesis Supervisor: Lionel C. Kimerling
Title: Thomas Lord Professor of Materials Science and Engineering

Acknowledgments

The PhD life at MIT is an arduous yet enjoyable process. I want to thank everyone who shows me beautiful scenes in this journey.

My thesis advisor, Prof. Lionel Kimering (Kim), is the most important person in my PhD career. Although he uses a hands-off style to manage the group, he always has a big vision about every project and indicates the most significant points in the research. Every time when I had new but exotic ideas, Kim was happy to discuss with me, using his experiences to point out a clear path for success. As a senior scientist who has worked in both industry and academia for decades, he tries his best to establish a solid bridge between science and technology. In the group, he gave me freedom to pursue my interests, cultivating my independent thinking and great enthusiasm towards investigating novel science and technology. Kim, I really want to thank you for all the support and guidance. You will be a role model throughout my scientific career.

Every member in my thesis committee have made significant contributions to improve and perfect my research and thesis. Dr. Jurgen Michel is a knowledgable scientist, always making critical suggestions for my research. I also regard him as my key research supervisor, and we had many extensive discussions to overcome various challenges in the projects. I also received numerous advices about self-assembled techniques when discussing with Prof. Caroline Ross and her group. Prof. Steven Johnson is the most passionate scholar about mathematics and electromagnetism. He not only generously shared many open source softwares with the whole world, but also used his sharp mind to contribute several key points in my research.

I was very lucky to work within the EMAT group. Every Ematter is a good friend and a good colleague to work with, and I believe everyone will continuously make great success in their future career and life. Dr. Anuradha Agarwal, Dr. Anat Eshed and Dr. Xiaoman Duan are always taking care of students' research and life like our warm-hearted mothers. Dr. Lirong Broderick and Prof. Yasha Yi are the pioneers of the solar cell research in our group, and I feel very lucky to become their successor and still work with them. Prof. Juejun Hu and Prof. Jifeng Liu are great collaborators and mentors, who are using their diligence and brilliant ideas to demonstrate how to survive in academia. Dr. Kevin McComber had been my office mate for almost 4 years. I learned a lot from him about American

cultures and life, and I respect his responsibilities for many social activities. I really enjoy working and talking with everyone in the group: Prof. Kazumi Wada, Dr. Pao-Tai Lin, Dr. Lin Zhang, Dr. Rong Sun, Dr. Jing Cheng, Dr. Xiaochen Sun, Dr. Jianfei Wang, Dr. Jonathan Bessette, Dr. Winnie Ye, Dr. Donghwan Ahn, Dr. Tim Zens, Prof. Clara Dimas, Michiel Vanhoutte, Vivek Raghunathan, Rodolfo Camacho-Aguilera, Louisa Chiao, Yan Cai, Neil Patel, Vivek Singh, Brian Albert, Brian Pearson, Zhaohong Han, Wei Yu and Corentin Monmeyran. Finally, Ms. Lisa Sinclair shows her warm heart and patience when administrating the EMAT. She is the hero who makes the group a success.

In addition to the experimental setup in our own labs, facilities in MTL and CMSE provided most of the fabrication and materials characterization tools. Mr. Kurt Broderick is a machine expert and a nice friend. I spent many tough days and nights in his lab (EML) preparing my devices. Mr. Yun Seog Lee in Prof. Tonio Buonassisi's lab helped me on lots of hands-on solar cell measurements. I would also like to thank MIT Ab-initio Research Group for sharing their numerical simulation programs and computing clusters. Wenjun Qiu, Dr. Peter Bermel and Dr. Ardavan Oskooi gave me many useful instructions on photonic device simulations.

Without funding, I could not be admitted to MIT or involved in any research projects here. I want to thank Ms. Angelita Mireles for managing the records for all DMSE graduate students. I really appreciate the financial supports in the past few years from all of our sponsors, including DuPont-MIT fellowship, MIT presidential fellowship, MIT Energy Initiative, Masdar Institute and Robert Bosch LLC. Especially, I have to thank our collaborators, Dr. Inna Kozinsky from Robert Bosch LLC, Dr. Rao Gutlapalli Venkata and Dr. Andre Hedler in Bosch Solar Thin Film GmbH. Inna provided persistent management on our 2.5-year MIT-Bosch project, holding various valuable discussions with us. Rao and Andre generously shared their solar cell samples and experiences with the state-of-the-art PECVD techniques.

Besides scientific research, I also get very interested in educating younger students with my knowledge. In the teaching class, Prof. Edwin Thomas and Prof. Samuel Allen shared us their experiences about being a good professor and a good teacher. Prof. Lorna Gibson, Prof. Yoel Fink and Kim gave me the opportunities to be a teaching assistant in their courses, fulfilling my teaching minor. Most importantly, I have to thank those undergraduate students in my classes. It was their suggestions and advices that really taught me how

to teach.

Student groups at MIT and Boston always provide me with great joy and relax, making my PhD life more colorful. I want to thank MIT Graduate Student Council (GSC), DMSE Graduate Materials Council (GMC), MIT Chinese Student and Scholar Association (CSSA), MIT Chinese Association of Science and Technology (CAST), Boston Tsinghua Alumni Association (THAA) and Boston Jiangxi Group, for all the great parties, delicious foods, and most importantly, interactions with various old and new friends. Especially, I will thank Mr. Hang Yu and Mr. Liang-Yi Chang. We joined DMSE at the same time and have become good friends since then. We have lots of great time together, discussing about research, culture and life.

Finally, I have to thank all my friends and family members in my homeland China, especially my parents who gave me all their patience and perseverance to make me become a grownup man. And my beloved wife Lan Yin, thank you for the support without any regrets. We have been known each other for more than 8 years and married for 3 years. We have experienced all the happiness and unhappiness together, and we will never separate.

What has been will be again,
what has been done will be done again;
there is nothing new under the sun.
—*Ecclesiastes 1:9*

Contents

List of Figures

List of Tables

Chapter 1

Introduction

1.1 Overview of solar cells

1.1.1 Solar energy

Along with the world population growth and economic development, energy consumption has become a global challenge for many years. Over the last few decades, while the consumption of energy grew substantially, the world has been remaining highly dependant on fossil fuel based energy sources, like coal, oil and natural gas [11]. On the other hand, primary fossil fuel sources and major nuclear fuels like uranium have limited reserves and cannot be generated in a short time. Figure 1-1 illustrates the reserves for various energy resources [1]. As reported in 2009, the annual world energy consumption is about 16 TW $\cdot$ year (equal to about 3×10^{19} J), which will increase to about 28 TW $\cdot$ year in 2050. For non-renewable energy resources including coal, petroleum, natural gas and uranium, the total amounts of reserves known today are 900 TW $\cdot$ year, 240 TW $\cdot$ year, 215 TW $\cdot$ year and 300 TW $\cdot$ year, respectively. Therefore, these sources can only support us for very limited time (about a hundred years). Moreover, consumption of fossil and nuclear fuels puts a great pressure on the environmental sustainability, causing pollution and greenhouse effects globally.

Renewable energy technologies should be advanced to meet the future energy demand and reduce the dependence on non-renewable fuels. Among all the renewable options for energy sources including solar, wind, hydropower, biomass, wave, etc, the solar energy is orders of magnitude larger than all the others combined and can easily meet the world demand. Therefore, solar energy will probably be the ultimate energy source that can

potentially supply most of the world energy consumption in the future. Various technologies have been developed to utilize the solar energy, like photovoltaic [12], photothermal [13] and photoelectrochemical systems [14]. In this thesis, we mainly focus on the photovoltaic (solar cell) technology, which directly converts light into electricity through the photovoltaic effect in semiconductors.

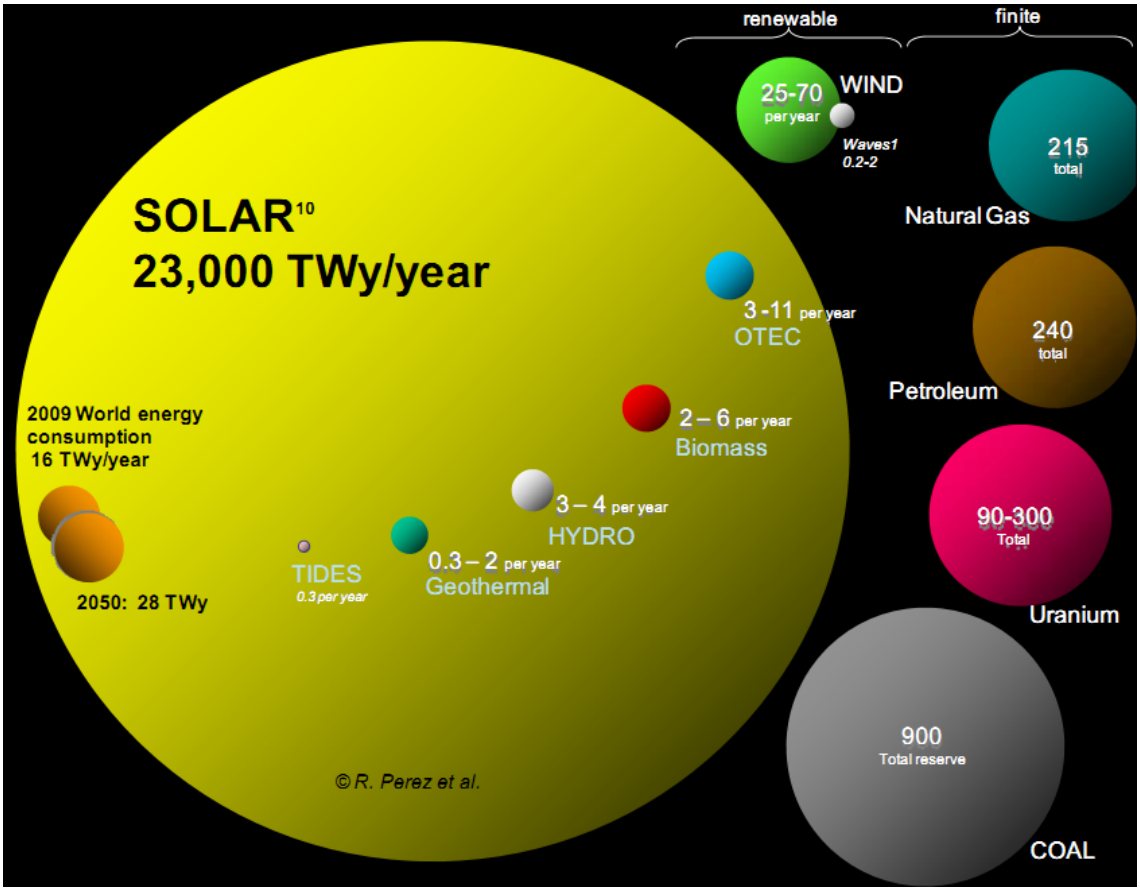

Figure 1-1: Annual world energy consumption, in comparison with various energy resources [1]. For renewable energies, yearly potential is shown, while total reserves are shown for non-renewable resources.

1.1.2 Photovoltaic effect

Figure 1-2 shows the basic structure for a photovoltaic cell (solar cell) circuit, which includes a pn junction made of semiconductor materials, metal contacts and external loads. When light is incident on the solar cell, several steps are involved to convert the photon energy into electricity:

1. Light goes into the device, and gets absorbed by the semiconductor;

2. Absorbed photon energy excites free electron-hole pairs;

3. Due to the build-in electric field in the depletion region of the pn junction, minority carriers are swept across the junction and become majority carriers (shown in Figure 1-3);

4. The photo generated free carriers are collected by contacts and flow into the external circuit, forming electric energy.

The above steps establish the photovoltaic (PV) effect. An example of the measured solar cell JV curves are shown in Figure 1-4. When the cell is in the dark, the curve exhibits a typical diode behavior, and cross the origin ($J = 0$ when $V = 0$). When light is incident on the cell, photocurrent can be generated and a net output electrical power can be obtained. From the measured JV curve under illumination, we can obtain several important figures of merit for solar cells:

1. Short-circuit current density J_{sc}, which is the current density when voltage is zero;

2. Open-circuit voltage V_{oc}, which is the voltage when current is zero;

3. Maximum output power, which is the point in the JV curve where output power $P = J \cdot V$ is maximum;

4. Cell efficiency $\eta = P_{out}/P_{in}$, which is the maximum power divided by the incident light power. For AM1.5G spectrum, the input power is 0.1 W/cm^2;

5. Fill factor, which is defined to be $FF = \frac{P_{out}}{J_{sc} \cdot V_{oc}}$.

1.1.3 Conventional c-Si solar cells

Suitable semiconductors should be chosen to make efficient and cost-competitive solar cells. Nowadays, more than 85% of the PV market is dominated by crystalline silicon (c-Si) solar cells, including polycrystalline Si (poly-Si) and monocrystalline Si (mono c-Si) (Figure 1-5). This is mainly resulted from several advantages of c-Si:

1. Silicon is one of the most abundant elements on the earth, suitable for large-scale production;

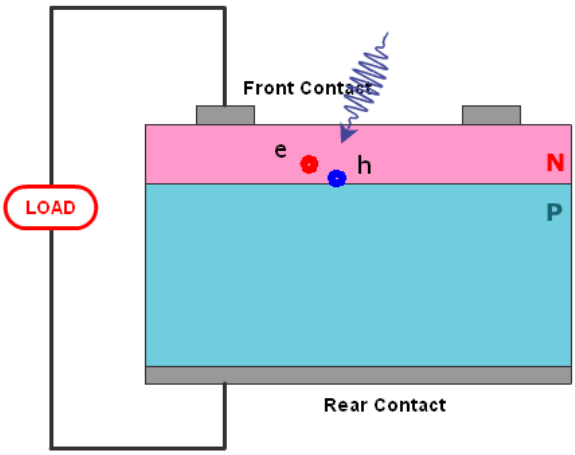

Figure 1-2: Schematic structure for a solar cell, including a semiconductor pn junction, metal contacts and external loads. Source: `http://www.pveducation.org/pvcdrom`

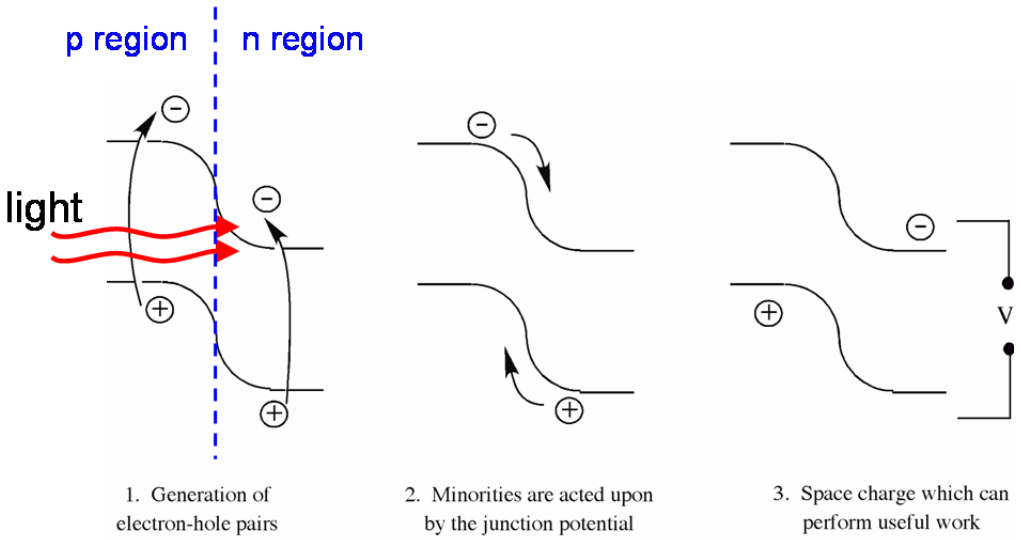

Figure 1-3: Band structures and solar cell operation.

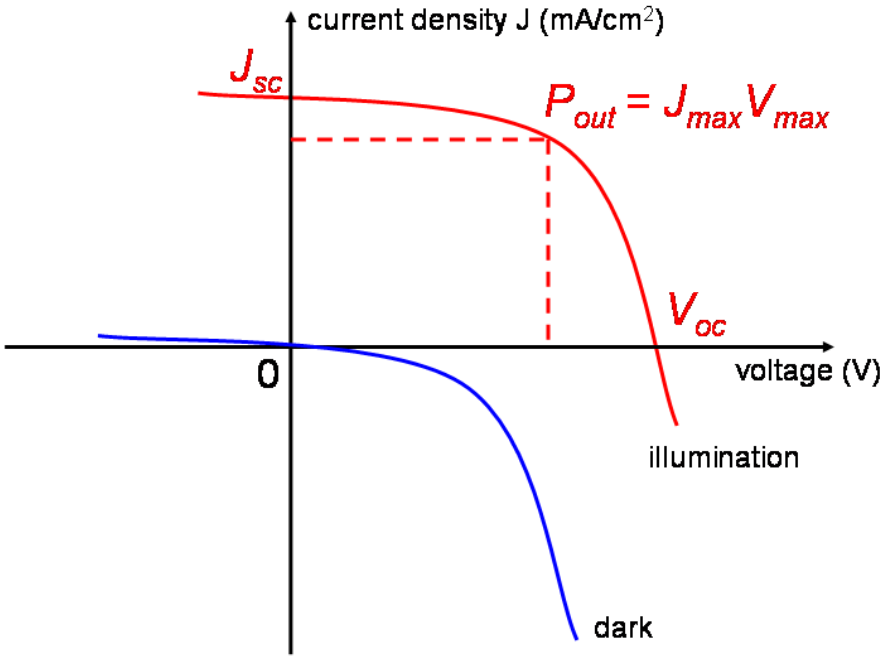

Figure 1-4: Schematic of measured JV curves under dark or illumination. Important figures of merit are indicated.

2. c-Si has an almost ideal bandgap ($E_g = 1.12$ eV) to achieve high device efficiency, obtaining optimal trade-off between photon absorption and output voltage;

3. c-Si has been widely used in microelectronic industry. The technologies for Si device process, including material purification, deposition, doping and metallization, are very mature and can be easily adapted to solar cell production;

4. Silicon is a safe material for human-being and environmentally benign.

Traditional c-Si based solar module manufacturing involves numerous steps, like Si refining and purification, ingot growth, wafer slicing, diffusion, texturing, coating, metallization and packaging [15].

1.2 Thin-film Si solar cells: opportunities and challenges

1.2.1 Motivations for thin-film Si

Despite the advantages of c-Si and significant growth of solar cell production in recent years, cumulative solar energy production only accounts for less than 1% of the global energy

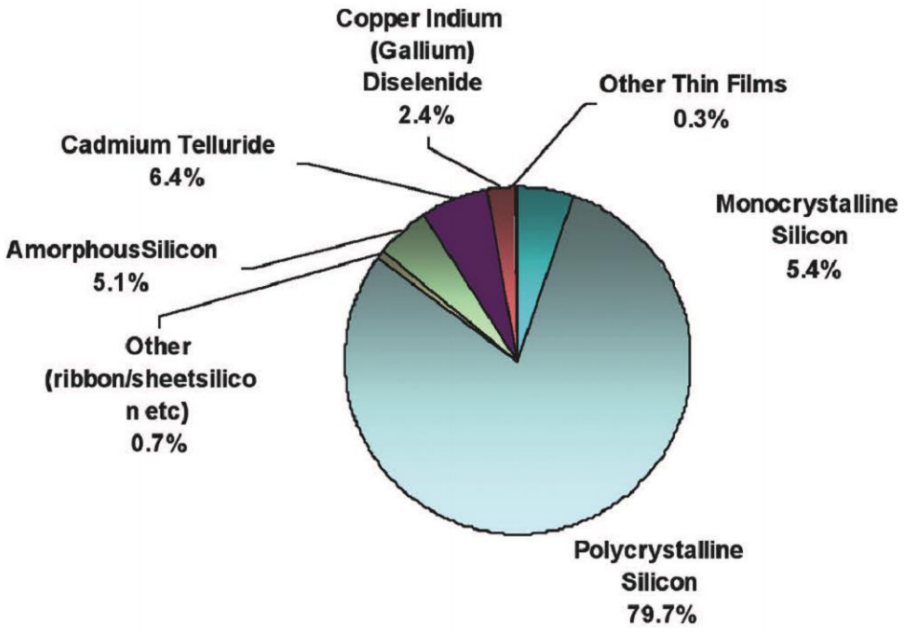

Figure 1-5: Solar cell market share in 2010 [2].

supply [11]. The major obstacle for further scale-up production and application of PV systems is the manufacturing cost, which is still much higher than the cost of grid electricity. Almost half of the cost of c-Si based PV technique comes from the starting material, which is the several-hundreds-micron thick silicon wafer, and this part of cost is very difficult to reduce [16]. Thin-film solar cells, which have an active layer of only several micrometers thick, are believed to be a promising candidate for further cost reduction. Various types of thin-film solar cells based on materials like thin-film Si, III-V semiconductors, CdTe, CuInGaSe and organic materials are proposed and being extensively studied [17]. Among all these thin-film based PV technologies, thin-film Si solar cells, including single crystalline Si (c-Si), amorphous Si (a-Si), polycrystalline Si (poly-Si) and microcrystalline Si (μc-Si) cells, are believed to be the most promising candidates for low-cost terawatts scale production while maintaining the advantages of bulk silicon. Typical thin-film Si solar cell structures are illustrated in Figure 1-6. The active device is a thin Si based pn junction, sandwiched between transparent conductive oxide (TCO) layers as front and back contacts. Thick substrates are required to support the thin-film device. In the superstrate configuration (Figure 1-6(a)), a glass plate is placed on top of the device, while in the substrate approach (Figure 1-6(b)) glass, steel or other cheap materials can be used as substrates. Another advantage of thin-film Si cells is that the photon generated free carriers only need a very

short diffusion length to reach the contact layers. Therefore, low quality materials such as a-Si, poly-Si and μc-Si can be used while maintaining a high collection efficiency.

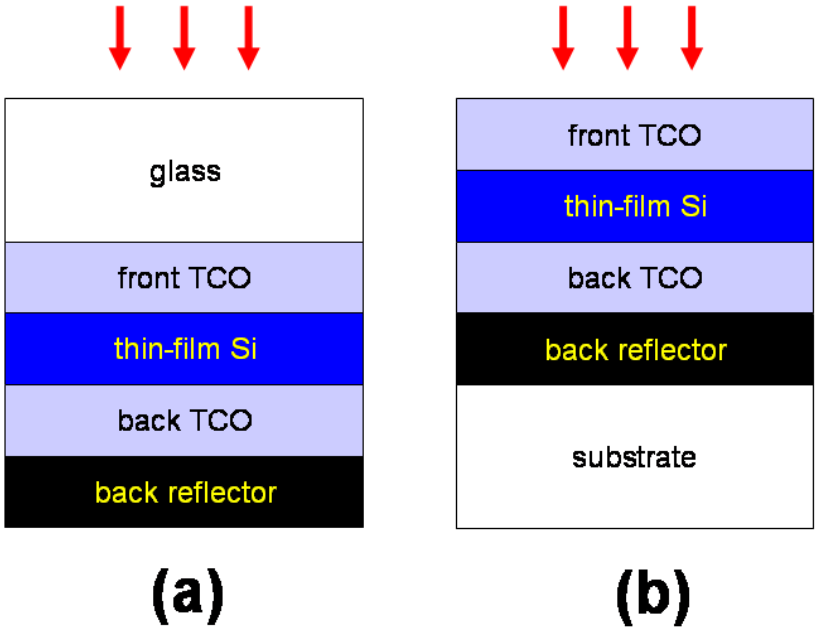

Figure 1-6: Thin-film Si cell structures with superstrate (a) and substrate (b) configurations. Surface textures are not illustrated.

Nowadays, thin-film Si solar cells still show inferior performances compared to their bulk c-Si based counterpart. The world record efficiency for c-Si cells is about 25.0% [10], while the best efficiency for 2 μm thick poly-Si cells is only about 10% [18]. The relatively low efficiency is mainly caused by limited photon absorption and high recombination in the low quality materials. To make competitive solar modules, the cell efficiency should be further improved by implementing new design and fabrication methods. Meanwhile, fundamental questions should be understood in order to explore the underlying physics about cell performance limits.

1.2.2 Light trapping and efficiency limits

The efficiency of solar cells critically depends on optical absorption in the active Si layers. Due to its indirect bandgap nature, c-Si has low absorption coefficient in the red and near-infrared (IR) wavelength ranges. As shown in Figure 1-7, a 300 μm thick Si device can absorb most of the photons with wavelengths below 1000 nm. However, a 2 μm thick

Si cell cannot effectively absorb photons in the range between 600 nm and 1000 nm in a single pass, leading to a lower cell efficiency. Therefore, an effective light trapping design is indispensable to achieve high efficiency modules.

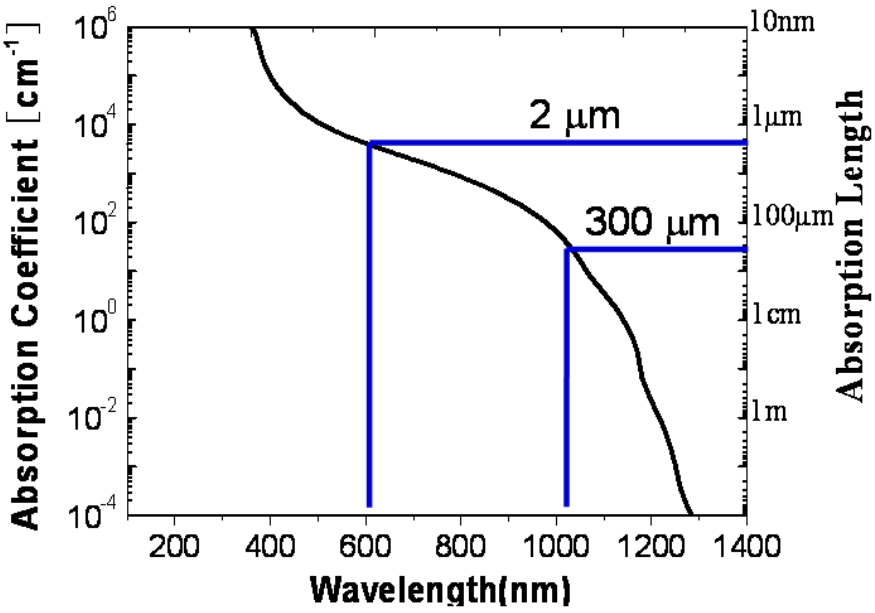

Figure 1-7: Absorption coefficient α and absorption length L for Si as a function of wavelength. The absorption length is defined as $L = \alpha^{-1}$.

To address this problem, various methods are used in current technology, for example, traditional light trapping schemes such as textured transparent conductive oxide (TCO) and metal reflector [3]. An example of such a structure is shown in Figure 1-8. These methods are difficult to precisely control and optimize the textured surface both experimentally and numerically. In addition, some other issues should be considered such as enhanced surface recombination due to the roughness of silicon layer [19] and parasitic loss at the TCO/metal interface [20].

Recently, one, two and three dimensional photonic crystals have also been proposed to enhance the light trapping [4]. One example of a device with such a photonic crystal structure is illustrated in Figure 1-9. The photonic crystal can form a forbidden photonic bandgap in a specific wavelength range, obtaining an almost 100% reflectivity. In addition, 2D and 3D photonic crystals can induce light diffraction because of the periodicity in lateral direction, scattering light into oblique incident angles. Furthermore, other advantages of

such photonic crystals are that they can be optimized numerically, and fabricated by deterministic approaches. However, fabrications of the photonic crystal design often involves in expensive techniques like photo lithography [21], which is very difficult to be implemented experimentally at a low cost. Recently, self-assembled 3D photonic crystals based on close packed nanospheres have been used to improve the light absorption in dye-sensitized solar cells. However, the method can only provide a photonic crystal with a low refractive index contrast since only limited materials like low-index TiO_2, SiO_2 or polystyrene could be used [22]. Therefore, a practical light trapping design is still in demand to obtain higher performances than traditional texturing techniques as well as easier fabrication than photonic crystals.

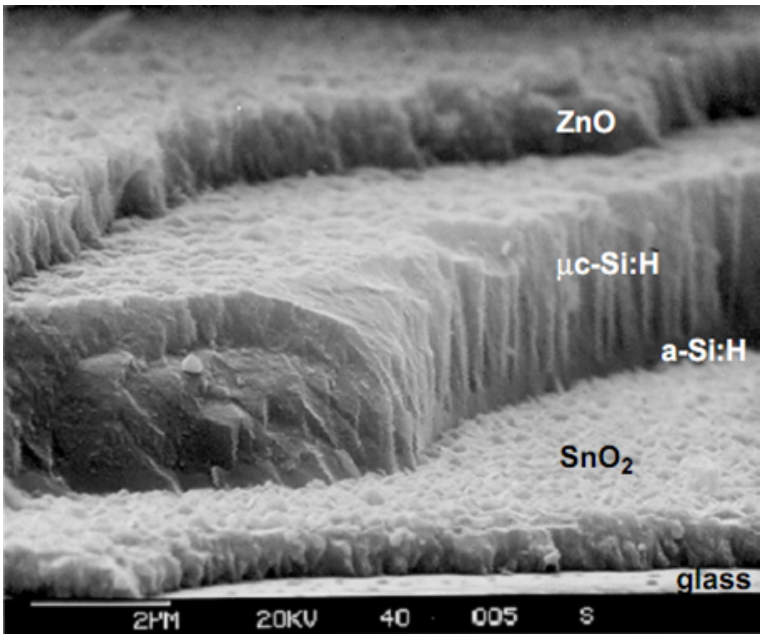

Figure 1-8: SEM image showing a micromorph Si cell with textured TCO surface for light trapping [3].

In addition, it is still unclear whether the various photonic crystal approaches can achieve significantly better light trapping performance compared to the conventional random texture approach. Also, some fundamental questions have not yet been solved for light trapping in thin-film Si solar cells. What is the ultimate limit for the absorption in the thin-film silicon, and what is the optimal design that can reach this limit? The Lambertian limit [23] has long been believed to be the ultimate light trapping limit and the benchmark for designing light trapping structures. However, the derivation of Lambertian limit (see Appendix A)

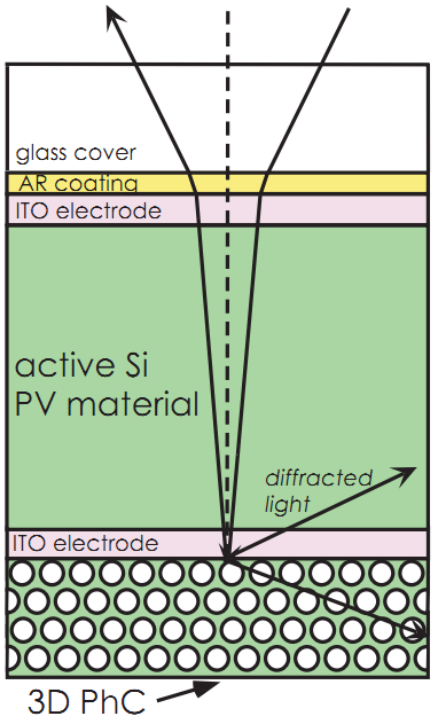

Figure 1-9: Light trapping design using photonic crystal back reflectors [4].

has very restrictive assumptions (for example, isotropic incident light and infinitely wide spectral range) and may not be suitable for some specific regimes.

Another fundamental question is the ultimate efficiency limit for a thin-film Si solar cell. Shockley-Queisser limit [24] predicts that the maximum efficiency for an ideal single junction solar cell under one sun illumination is about 31%. However, this theory assumes all the photons with energy above the semiconductor bandgap are totally absorbed and no non-radiative recombination occurs in the junction. For a thin-film Si device, these assumptions are no longer valid. Thin-film Si only has limited bandedge absorption even if light trapping design is considered. In addition, non-radiative recombination ratio is significant in Si due to its indirect bandgap nature. Therefore, a theoretical prediction should be provided to analyze the practical efficiency limit for thin-film Si solar cells considering optimal light trapping and ideal material quality.

1.3 Outline of the thesis

This thesis aims to design a novel light trapping scheme to enhance the cell efficiency, and explore the fundamental performance limits for thin-film Si solar cells.

In Chapter 2, we present a photonic crystal (PC) based structure for light trapping in the backside of thin-film Si solar cells. It consists of a distributed Bragg reflector (DBR) and a grating layer. We understand the operation principles of the PC based structure by simulating the photonic band diagram and field propagation in the device. We introduce the criteria of material selection and parameter design for the PC structure. We review our previous work on this design and present the existing challenges.

Chapter 3 introduces a self-assembled technique using anodic aluminum oxide (AAO) as a useful method for grating fabrication. We demonstrate that this AAO structure can be experimentally controlled and adjusted in an electrochemical condition. Organized patterns made of various materials can be obtained by using AAO as a template material. Furthermore, we numerically investigate the effect of disorder in AAO on cell light trapping performances and compare it with a perfectly periodic structure.

In Chapter 4, we experimentally implement DBR and self-assembled AAO on the backside of a thick Si based photoconductor for light trapping. The enhanced photo response in the bandedge of Si demonstrates that the self-assembled structure can effectively increase light path length.

In Chapter 5, we first review different types of thin-film Si technologies, including a-Si, μc-Si and micromorph Si solar cells. We then numerically optimize the structural parameters of the PC structure integrated in a 1.5 μm μc-Si solar cell, and show that more than 30% relative efficiency increase can be obtained by using the optimal structural parameters. Finally, we fabricate the grating pattern by self-assembled AAO templates, and obtain up to 20% increase in cell efficiency measurement.

Chapter 6 discusses the fundamental performance limits for thin-film Si solar cells. We develop an optimization based method to explore the optimal periodic textures for light trapping. We then compare our optimized grating with random textures as well as analytical models. We prove that our designed structures can exceed the prediction of conventional models in restricted regimes. Furthermore, a modified Shockley-Queisser model is proposed to predict the optimal efficiency for thin-film Si cells, including non-radiative recombination and light trapping effects.

Chapter 8 summarizes the major results and accomplishments in this thesis, and discusses the directions in future work.

Chapter 2

Photonic crystals for light trapping

In this chapter, we introduce a photonic crystal (PC) based design for light trapping application in thin-film Si solar cells. The design combines a distributed Bragg reflector (DBR) and gratings. It works as a scattering element as well as a reflector, significantly increasing the light path length inside the active device. First, analysis based on electromagnetic wave theory is utilized to understand the principles of the PC design. Then the previous work is reviewed and existing challenges are discussed.

2.1 Principles of design

2.1.1 Distributed Bragg reflector (DBR)

By its definition, a crystal is a solid material in which the elements (atoms, ions and/or molecules) form an ordered pattern in all the spatial dimensions. Properties of materials, especially electronic properties, critically depend on their crystal structures. This is because the electron waves have wavelengths comparable to the lattice parameters. Similarly, if we can create a periodic structure which has lattice parameters comparable to the optical wavelengths, it will significantly affect the propagation of optical waves. Such periodic structures are called photonic crystals [25]. Depending on the dimensions of the periodicity, they can be one-dimensional, two-dimensional or three-dimensional (1D, 2D or 3D) photonic crystals.

A distributed Bragg reflector (DBR) can be regarded as a 1D photonic crystal, which consists of multiple layers of alternating materials with different refractive indices. The

effect of DBR was first discovered by Lord Rayleigh [26]. If the thickness of each layer is chosen to be a quarter of the wavelength in this medium, constructive inferences are formed and the structure works as a high quality reflector. As a practical example shown in Figure 2-1, the DBR consists of 10 layers of material 1 and material 2, with refractive indices of $n_1 = 1.45$ and $n_2 = 2.0$, respectively. If the target central wavelength is $\lambda = 750$ nm, The thickness of each layer can be calculated as $d_1 = \lambda/4n_1 = 130$ nm and $d_2 = \lambda/4n_2 = 94$ nm. We can calculate the reflection spectrum by using transfer matrix method [27], assuming light is normally incident on the DBR from air. As illustrated in Figure 2-2, very high reflectivity can be obtained in the wavelength range from 0.7 μm to 0.85 μm, even though it is not a perfect photonic crystal (only 10 pairs of layers are used). This wavelength range with a high reflectivity is called optical stopband.

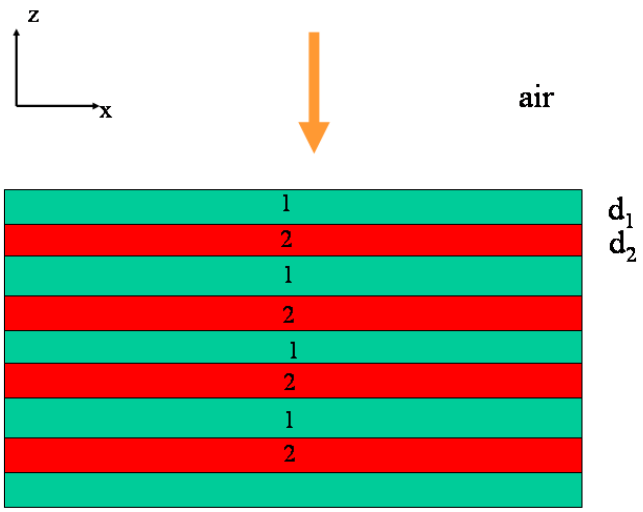

Figure 2-1: Schematic structure of a DBR, with normal incident light from air.

The above DBR structure, however, is not an omni-directional reflector. In Figure 2-3, we compare the reflection spectra of the same structure at the incident angle of 60 degree for both TE and TM polarizations with the response for normal incidence. Here TE means electric field is perpendicular to the incident plane, while TM means magnetic field is perpendicular to the incident plane. For both TE and TM waves, the stopbands shift to shorter wavelength (higher frequency). In addition, the reflectance for TM wave decreases significantly.

The above phenomena can be further understood through photonic band diagram.

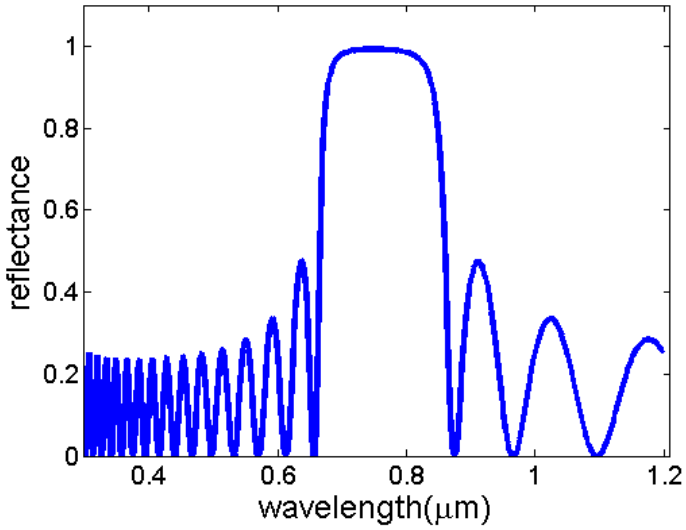

Figure 2-2: Calculated reflection spectrum of the structure shown in Figure 2-1, from 0.3 μm to 1.2 μm.

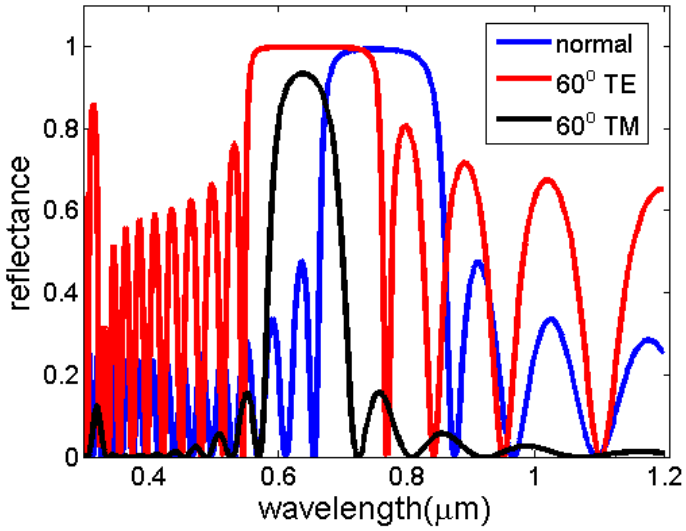

Figure 2-3: Calculated reflection spectra of the structure shown in Figure 2-1 for different incident angles and polarizations.

The band diagram of the periodic structure in Figure 2-1 is computed by preconditioned conjugate-gradient minimization of the block Rayleigh quotient in a planewave basis, using a freely available software package [28].[1] Figure 2-4 illustrates the first two photonic bands for the structure in Figure 2-1 for both TE and TM modes. The two black lines are called light lines, corresponding to the solution of plane waves propagate in the air (frequency $\nu = ck_x$). The region between the light lines ($\nu > ck_x$) are called the light cone. The modes out of the light cone are forbidden to propagate in the air. The two bands (blue and green colors) are the sets of modes that can be supported inside the periodic structure. The white region between the two bands and also inside the light cone is called photonic bandgap, which means that any solutions in this region can only exist in the free space (air) but not inside the photonic crystal structure. In other words, any light incident on the structure will be totally reflected back to the air. Normal incidence corresponds to $k_x = 0$, while oblique incidence corresponds to $k_x \neq 0$. It can be clearly observed that if k_x gets larger, the bandgap gradually disappears for TM wave, while the bandgap shifts to large frequency (short wavelength) for TE wave, which are consistent with the calculated reflection spectra shown in Figure 2-3. Therefore, there is no complete gap for any wavelength (frequency) ranging across the entire k_x regime inside the light cone for both TE and TM modes.

In order to obtain a complete photonic bandgap in a specific wavelength range, we need to change the material system. According to the perturbation theory [25], higher refractive index contrast should result in a larger bandgap, thus increase the possibility to achieve a complete gap. To verify this, we change the refractive index of material 2 to $n_2 = 3.6$, and the corresponding thickness $d_2 = \lambda/4n_2 = 52$ nm. The band diagram for the modified structure can be seen in Figure 2-5. In this case, the size of the bandgap is greatly increased, and we can find frequency ranges in which there are no solutions across the entire k_x region inside the light cone for both TE and TM wave. Those ranges are called complete gaps. In addition, the TE gap is wider than the TM gap. The existence of complete bandgaps can be verified by simulating the reflection spectra from air for normal incidence as well as oblique angles, as we do in Figure 2-3. Illustrated in Figure 2-6, nearly 100% reflectance can still be obtained if the incident angle is changed. Although the stopband shrinks for TM wave at oblique angles (consistent with the band diagram), a fairly wide gap is still maintained (around 600 nm to 900 nm).

[1] The software can be downloaded from `http://ab-initio.mit.edu/mpb`.

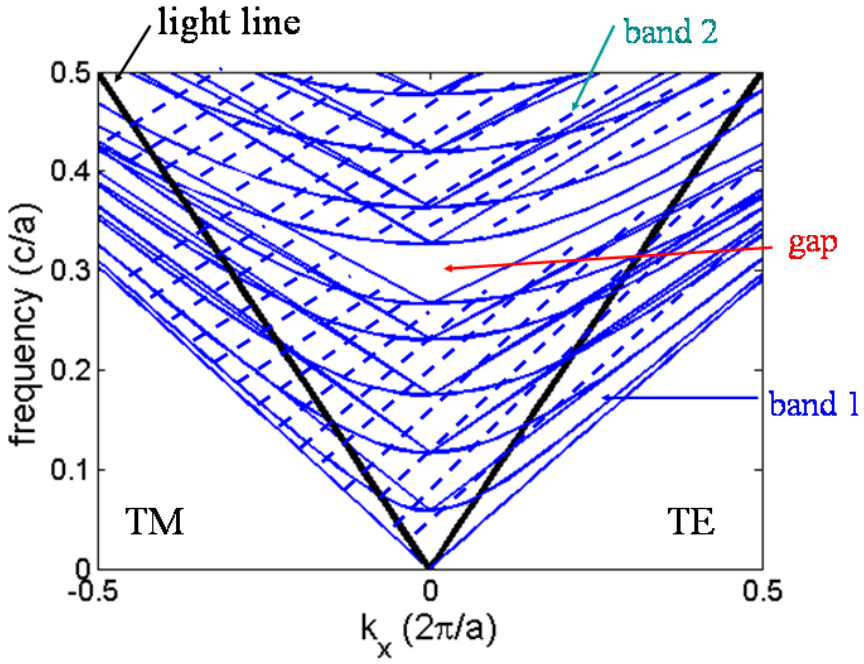

Figure 2-4: Photonic band diagram for the structure shown in Figure 2-1. $a = d_1 + d_2$ is the lattice constant of the DBR.

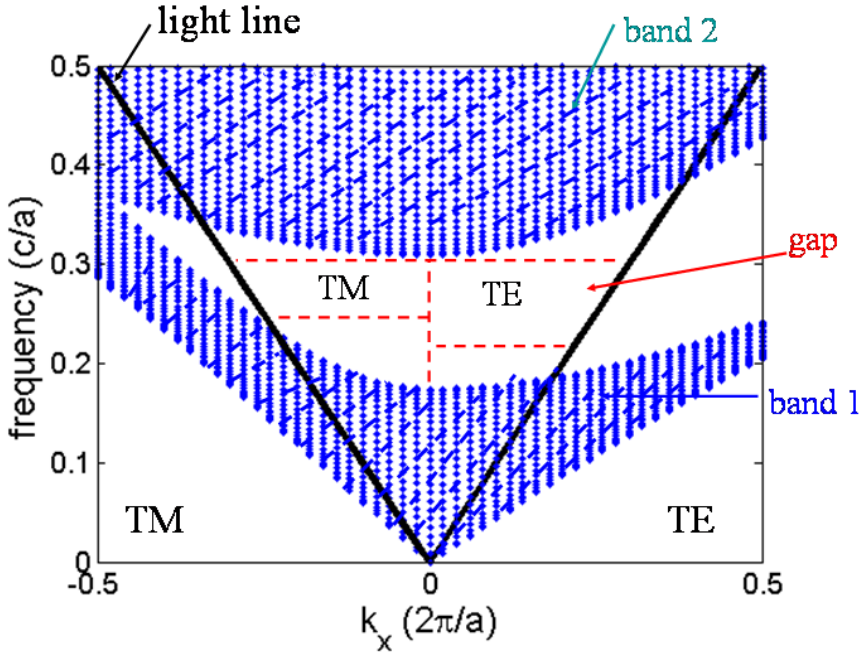

Figure 2-5: Photonic band diagram for the modified structure shown in Figure 2-1. n_2 is changed from 2.0 to 3.6.

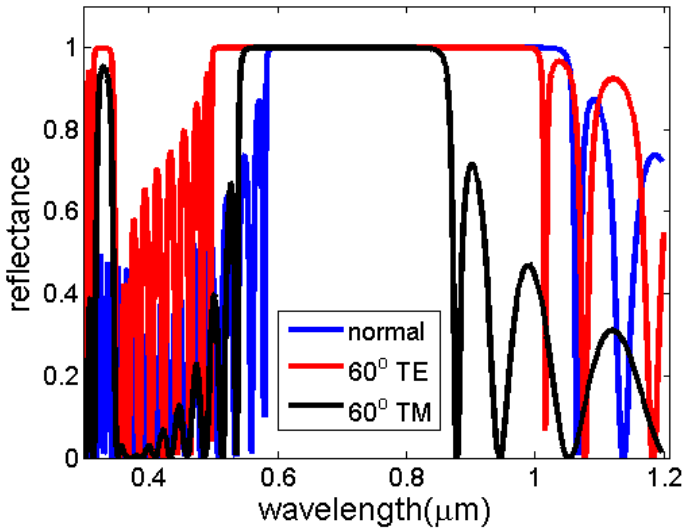

Figure 2-6: Calculated reflection spectra of the structure shown in Figure 2-1 (with $n_2 = 3.6$) for different incident angles and polarizations.

The performance of the above DBR structure is compared with aluminum (Al) or silver (Ag), which are conventionally used as reflectors for visible and infrared light. The optical constants (n and κ) of Al and Ag can be found in Ref. [29]. The reflectance of DBR is compared with Ag and Al reflector for different polarizations and incident angles, shown in Figure 2-7, Figure 2-8 and Figure 2-9. Although metals like Al and Ag can obtain a high reflectivity in a broader spectral range than DBR, they show inferior performance in a specific range. For example, at 0.8 μm for normal incidence, Ag and Al have reflectivity of about 98% and 85%, respectively, while DBR shows almost 100% reflectivity. Furthermore, the reflectance decreases for TM wave at oblique incidence. These results indicate that a properly designed DBR works as an even better reflector than metals, if it is used for a specific spectral range.

2.1.2 Combined photonic crystal

Because of its high reflectivity, the above DBR structure can be implemented with a thin-film Si solar cell to boost the cell performance. As shown in Figure 2-10(b), the DBR can double the light path length inside a planar Si device, thus increase the light absorption. However, doubling the light path length might be not enough for thin film Si due to its low absorption. Other mechanisms should be introduced to further increase the light path

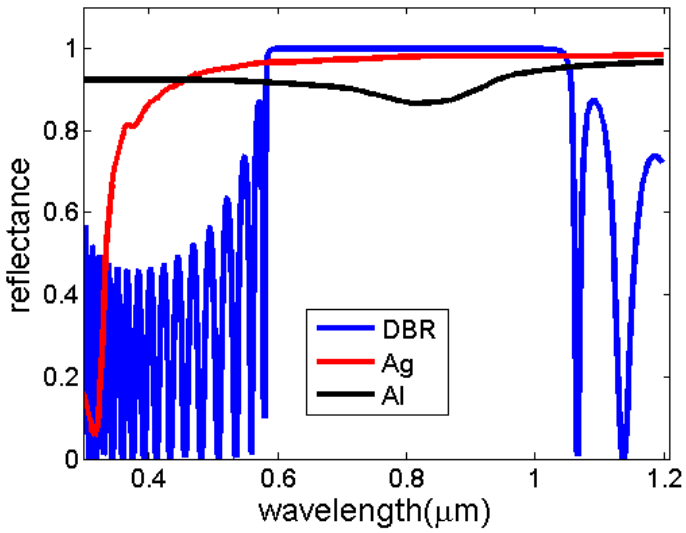

Figure 2-7: Calculated reflection spectra of the structure shown in Figure 2-1 (with $n_2 = 3.6$), compared with Ag and Al reflector at normal incidence.

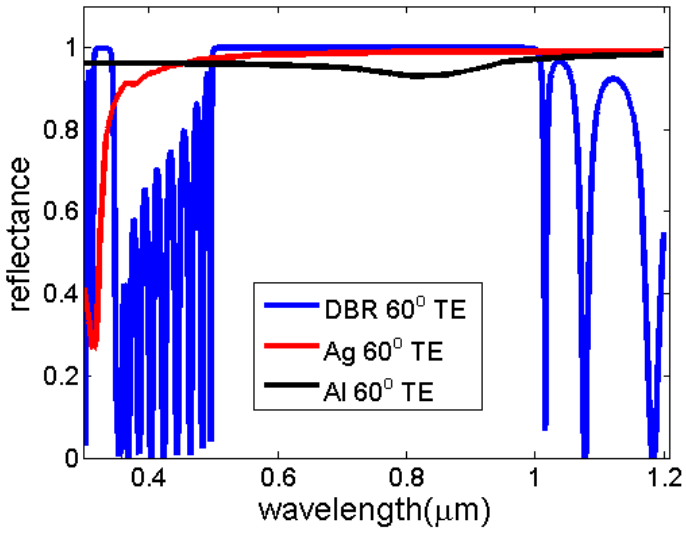

Figure 2-8: Calculated reflection spectra of the structure shown in Figure 2-1 (with $n_2 = 3.6$), compared with Ag and Al reflector. Incidence at 60 degree, TE polarization.

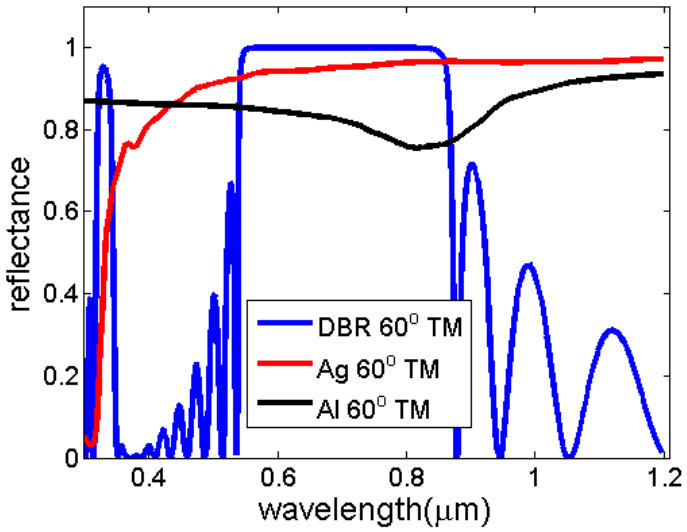

Figure 2-9: Calculated reflection spectra of the structure shown in Figure 2-1 (with $n_2 = 3.6$), compared with Ag and Al reflector. Incidence at 60 degree, TM polarization.

length. Illustrated in Figure 2-10(c), periodic textures (or gratings) are placed between the thin film Si and DBR. Periodic surface textures can induce diffraction, which leads to light propagation in oblique angles. Therefore, light absorption can be further enhanced and higher current density can be achieved.

When we discuss the properties of the DBR structure like that in Figure 2-1, we assume the structure is continuous in x direction. One question is, can the photonic band gap be maintained if we introduce a periodicity in x direction, as the PC structure in Figure 2-10? Due to the periodic boundary condition, all the bands are folded into the first Brillouin zone in k_x direction. For the band diagram in Figure 2-5, if we choose the grating period Λ, the first Brillouin zone will be in the range $-\pi/\Lambda < k_x < -\pi/\Lambda$. Figure 2-11 shows how the band diagram will change when $\Lambda = 0.7$ μm. Due to the band folding, both TE and TM band gaps will disappear. Therefore, *the DBR will no longer be a perfect reflector if the grating is introduced, and light can propagate in the DBR.*

This discovery means that part of light cannot be reflected back into the thin-film Si and will be lost into the DBR. To quantitatively understand this effect, we simulate a simple device structure. In this structure, a square grating layer and DBR are in the back of a thin film Si with a thickness of 2 μm. The DBR is 5 pairs of SiO_2 and Si, with $n_1 = 1.45, d_1 = 130$ nm and $n_2 = 3.6, d_2 = 52$ nm. The grating layer has a thickness of

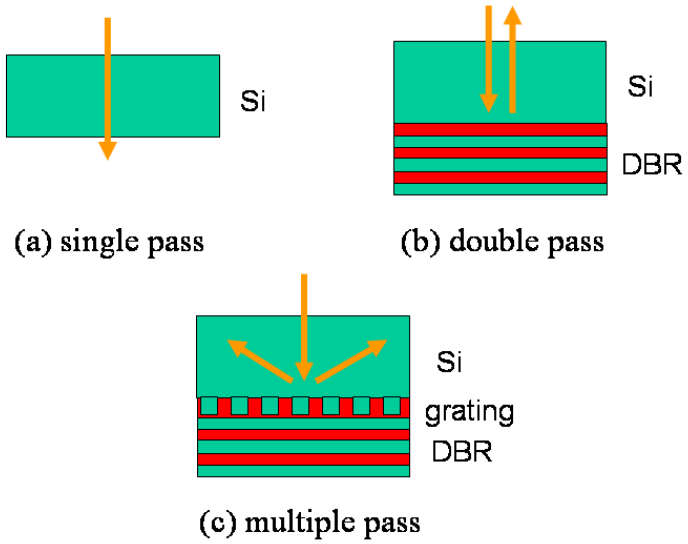

Figure 2-10: Schematics of a planar thin film Si solar cell with different back structures. (a) Device without any back structure. Incident light only has single pass inside the device; (b) Device with DBR. Normal incident light can be reflected and can have double pass; (c) Device with grating and DBR. Light can be scattered into oblique angles and have multiple pass.

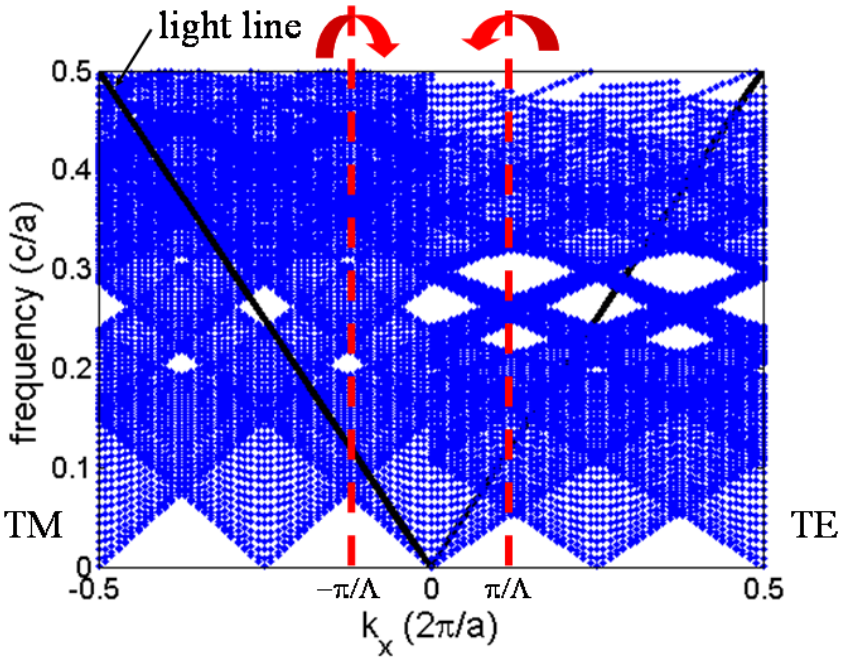

Figure 2-11: Sketch of band diagram for the PC structure. The grating period is $\Lambda = 0.7$ μm. The DBR structure is the same as in Figure 2-5. Because of the band folding, bandgap disappears.

150 nm, consisting of SiO_2 and Si. Here we just want to evaluate the reflectance of the DBR without considering the absorption loss in the structure, so we can assume all the materials are transparent. The reflectance spectra of this structure for normal incident light with both TE and TM polarizations are plotted in Figure 2-12. However, high reflectances are still maintained from 0.6 μm to 1.0 μm, in spite of the existence of some small dimples (for example, at $\lambda = 0.7$ μm for TM wave, and $\lambda = 1.0$ μm for TE wave.). These results seem to be inconsistent with the analysis of the photonic band diagram, since we learn that there is no bandgap when a grating with a period $\Lambda = 0.7$ μm is introduced. Why the high reflectivity can still be maintained?

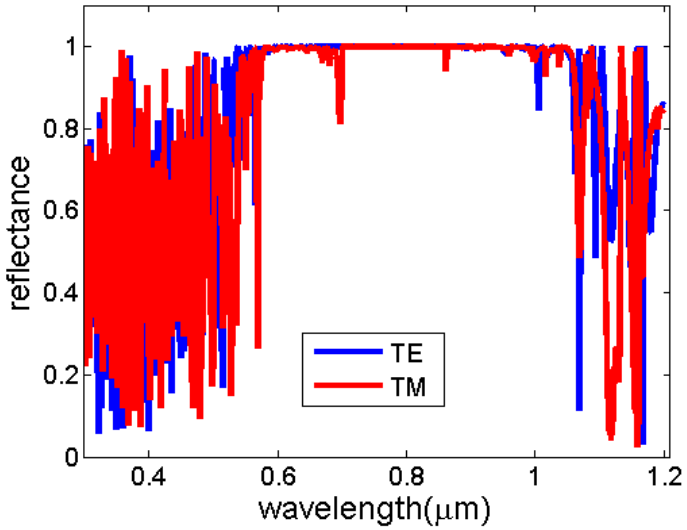

Figure 2-12: Reflectance spectra of a simple thin film Si structure with a grating and DBR in the backside. The incoming light is normal incident, with both TE and TM polarizations.

In Figure 2-13 we consider wave propagation in different DBR structures. When a guided wave is incident at the interface between a semi-infinite DBR and air interface (Figure 2-13(a)), it is totally reflected backwards, only evanescently decaying into the air. We can also understand this by the rule of reciprocity, considering that a wave incident from the air will be perfectly reflected if its wavelength falls into the photonic bandgap. If the DBR has a finite thickness D with a grating on top (Figure 2-13(b)), the wave can be coupled into the bottom air because of the band folding shown in Figure 2-11. However, the photonic local density of state (LDOS) at the interface exponentially decreases as its distance D from the grating increases [30]. When the DBR is thick enough, the coupling into the bottom

air become negligible. Therefore, the reflection at the finite DBR / air interface can still approach 100%, similar to the case in the semi-infinite DBR (Figure 2-13(a)).

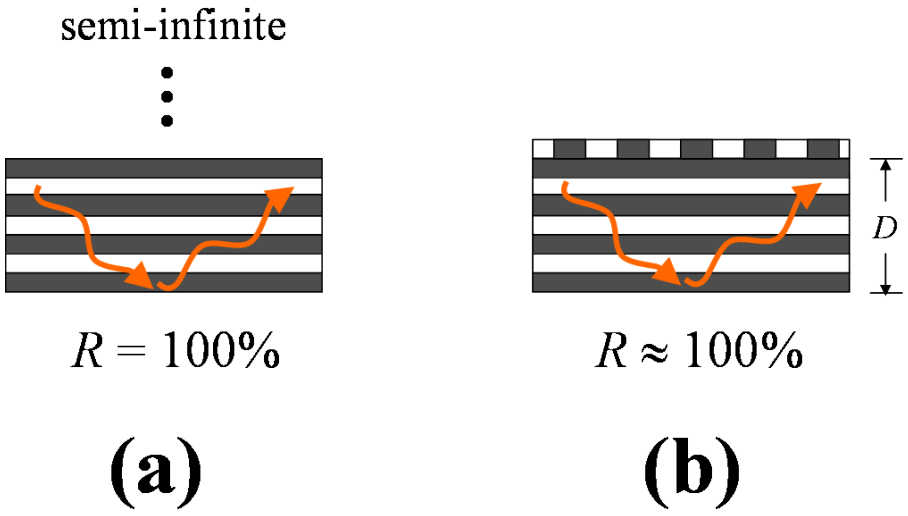

Figure 2-13: Guided wave propagating in a semi-infinite DBR structure (a) and finite DBR with a grating on top (a).

To further illustrate the above results, we simulate the wave propagations inside the device structures. We establish a simple device model to elucidate the mechanisms, illustrated in Figure 2-14. The reference structure in Figure 2-14(a) is a planar 1.5 μm thin-film c-Si cell with an anti-reflective coating (ARC) made of 70 nm thick silicon nitride. For comparison, the cells with grating and DBR are illustrated in Figure 2-14(b) and Figure 2-14(c). The DBR consists of 5 pairs of alternating SiO_2 and a-Si, with thicknesses mentioned in previous paragraphs. The 1D grating layer shown in Figure 2-14(c) is also made by SiO_2 and a-Si, with a thickness of 100 nm, period 700 nm and duty cycle 0.5. The optical constants for all the materials are found in [29]. We assume the incident light is a TE polarized continuous plane wave with a wavelength of 0.8 μm. The electric field distribution at a steady state is also plotted in Figure 2-14. Simulations are performed with the finite-difference time-domain (FDTD) method [31], using a freely available software package [32].[2] In the reference cell without any reflectors, light pass through the thin-film Si cell into the air environment. If planar DBR is placed in the backside, the formed photonic bandgap reflect the incident light back into the thin-film Si, doubling the optical path length. When the grating layer is embedded between the Si and DBR, the field distribution in the thin film Si

[2]The software can be downloaded from `http://ab-initio.mit.edu/meep`.

indicates that scattering occurs. Furthermore, the electric field is not only scattered backwards but also forwards into the DBR, due to the band folding introduced by the periodic grating. Therefore, the field does not evanescently decay in the DBR, but forms propagation modes, which is consistent with the predictions of the folded band diagram. However, there is no field can penetrate into the bottom air layer. *Almost all the waves are totally reflected back at the DBR/air interface.* This explains the high reflectivity we observe in Figure 2-12, which does not contradict the band diagram.

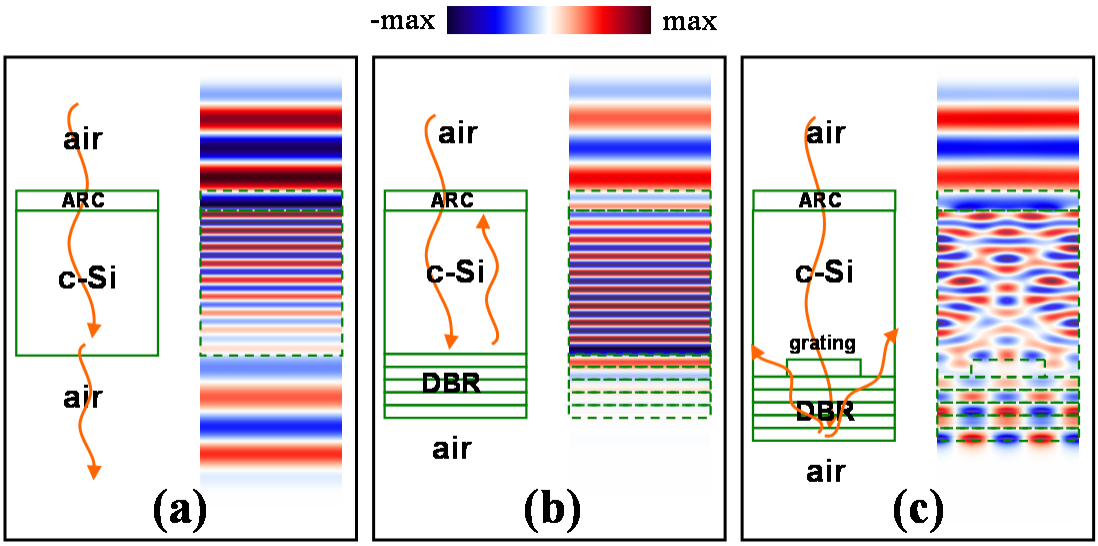

Figure 2-14: Simulated electric field distribution (incident light wavelength is 800 nm) in planar 1.5 μm thin-film c-Si cells with different light trapping schemes: (a) with an anti-reflective coating (ARC) only; (b) with ARC and DBR; (c) with ARC, grating and DBR.

2.1.3 Materials selection

To integrate the PC design with thin-film Si cells for light trapping, proper materials and structural parameters should be selected. The criteria for materials selection are:

1. The two materials for making DBR and grating should have high refractive index contrast, so that the DBR can provide a large photonic bandgap (for example, from 0.7 μm to 1.1 μm), and the grating can provide strong scattering effect;

2. As we learn from the previous section, the electromagnetic fields are distributed in the whole device structure, including the active Si layer, grating and the DBR. Therefore, the materials for grating and DBR should be transparent enough to reduce the

parasitic absorption, which does not contribute to generation of electron-hole pairs;

3. The material deposition and structure fabrication should be compatible with the solar cell fabrication process, and not involve complicated steps such as high temperature annealing and wet chemical etching which severely degrade the active device performances.

As we show previously, SiO_2 ($n_1 = 1.45$) and Si ($n_2 = 3.6$) should be very good candidates, since they can provide large index contrast and feasibility of fabrication. One problem is that crystalline Si (c-Si) has a bandgap of 1.1 eV, corresponding to a wavelength of 1.15 μm. Therefore, parasitic absorption will be induced in the PC for the wavelength range (for example, from 0.7 μm to 1.1 μm) in which we want to achieve light trapping. A better choice would be amorphous Si (a-Si), which has a similar refractive index with c-Si [29] and a larger bandgap. Therefore, a-Si is more transparent than c-Si in the near-IR range.

2.2 Effects of DBR on light trapping

In previous sections, we demonstrate that the planar DBR and the combined PC (DBR with periodic gratings) provide high reflection with totally different mechanisms. Therefore, the DBR structures with and without grating play different roles on the light trapping in thin-film Si cells. Here we study the influence of the DBR on the light trapping performance for thin-film Si cells. We still use the numerical model shown in Figure 2-14 and assume the normal incident light is from 750 nm to 900 nm. Photocurrent density J_{ph} is introduced to characterize the light trapping effect:

$$J_{ph} = e \int_{750\text{ nm}}^{900\text{ nm}} A(\lambda) S(\lambda) d\lambda \tag{2.1}$$

where $A(\lambda)$ is the absorption spectra in the active 1.5 μm c-Si layer calculated by FDTD methods and $S(\lambda)$ is the standard AM1.5G solar spectrum [33]. Here we assume each absorbed photon can generate one electron-hole pair. We vary the number of dielectric pairs in the DBR and calculate the J_{ph} for different cell structures in Figure 2-14. We also simulate semi-infinite DBR by embedding alternating SiO_2 and a-Si layers into the perfectly matched layer (PML) absorbing boundary in FDTD. The results are illustrated

in Figure 2-15. For the device without grating, the first few layers of DBR significantly improve the J_{ph} by inducing strong reflection. After implementing 3 pairs of SiO_2 and a-Si, the light reflection saturates and additional DBR pairs cannot further improve the absorption (Figure 2-15(a)). This is because the optical field evanescently decays in the cell with planar DBR as shown in Figure 2-14(b). However, light is scattered into the DBR when the grating layer is added. Since reflection occurs at the bottom DBR surface, loss is introduced in the DBR due to the absorption of a-Si [29]. When DBR becomes thicker, the loss in the DBR dominates. Therefore, the cell structure with a 10-pair DBR or semi-infinite DBR collects less photocurrent compared to the cell with a 3-pair DBR in Figure 2-15.

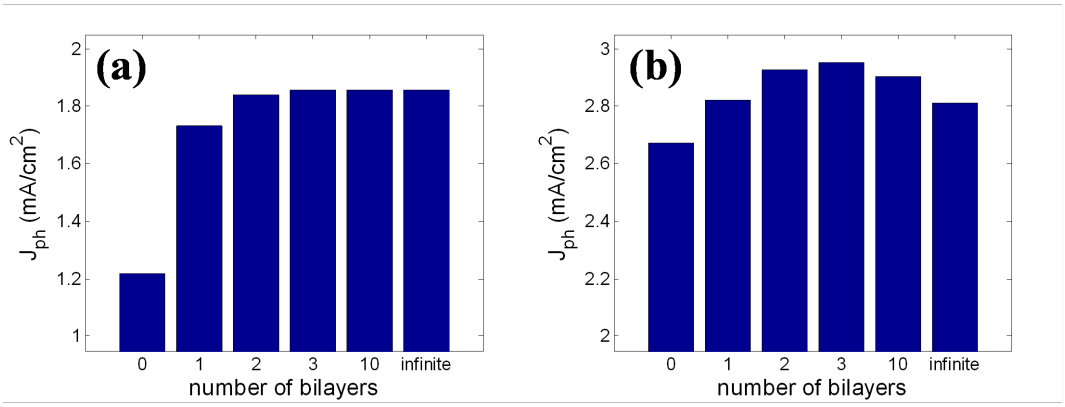

Figure 2-15: Influence of the number of DBR pairs on the integrated J_{ph} (normal incidence from 750 nm to 900 nm) of the c-Si solar cells in Figure 2-14(b) and (c): (a) without grating; (b) with grating.

2.3 Previous work

In this section, we briefly summarize the previous work about PC structure for light trapping, which has been done in our group. The PC structure was integrated in silicon-on-insulator (SOI) based devices and showed improvement on cell efficiencies [34]. Although the PC concept was successfully demonstrated, lots of challenges still remain.

Figure 2-16 illustrates the detailed steps in the process flow of making thin-film Si solar cells with PC structure. Silicon-on-insulator (SOI) wafers were used as the starting materials for fabrication. The thickness of the active thin-film Si layer was 5 μm. Processing of the SOI active layer included grating formation with interference lithography, followed by reactive ion etching, DBR deposition using plasma enhanced chemical vapor deposition

(PECVD), bonding the active layer to a new handle wafer, removal of original handle wafer, ARC formation on the newly exposed Si surface, lateral p-i-n junction creation by ion implantation, and metallization with interdigitated top contacts. The TEM image of the fabricated PC structure is shown in Figure 2-17. The structural parameters of the grating (such as grating period and thickness) is determined by numerical simulations and optimizations [4,35]. The first few layers of the DBR is wavy but the rest gradually become flat in the PECVD process. Due to high temperature annealing, the deposited amorphous Si layers were crystallized and became polycrystalline, which was revealed by the black and white contrast in the TEM image. The cells without any reflector and only with DBR were also fabricated for comparison.

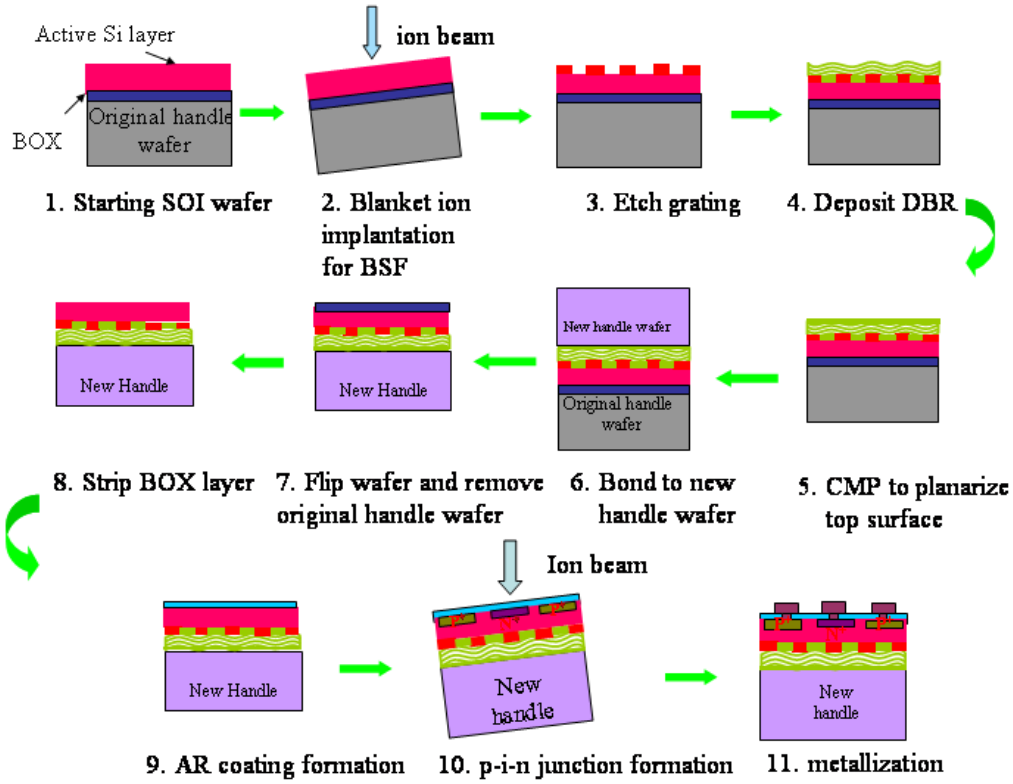

Figure 2-16: Process flow of fabricating the SOI based solar cells with PC structure.

Figure 2-18(a) depicts the measured external quantum efficiency (EQE) spectra. At short wavelengths, the EQE spectra significantly overlap but diverge as wavelength increases past 640 nm. The reference sample displays the lowest curve; the introduction of DBR back reflector makes the curve higher in the longer wavelengths; and the wavy DBR plus grating sample displays several shoulders and the largest area, corresponding to strongly enhanced

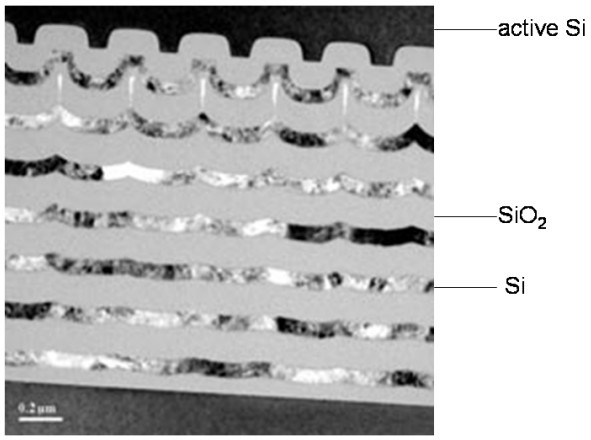

Figure 2-17: TEM image of the fabricated PC structure in the backside of thin film Si cells, including the submicron grating defined by interference lithography and multilayered SiO_2 and Si layers as DBR. The scale bar is 0.2 μm.

absorption. For comparison, the simulated absorption spectra are shown in Figure 2-18(b), which confirms that the measured EQE closely matches simulation in trend and magnitude. Current-voltage (IV) measurements demonstrate that each back structure improves absorption and cell efficiency, with the wavy PC cell achieved the highest J_{sc} of 17.45 mA/cm^2, corresponding to 18.9% enhancement over the reference cell versus 28.3% theoretically. The measured power conversion efficiency η vary from 7.68% for the reference cell to 8.82% for the wavy PC cell, corresponding to a relative efficiency enhancement of 14.8% [21].

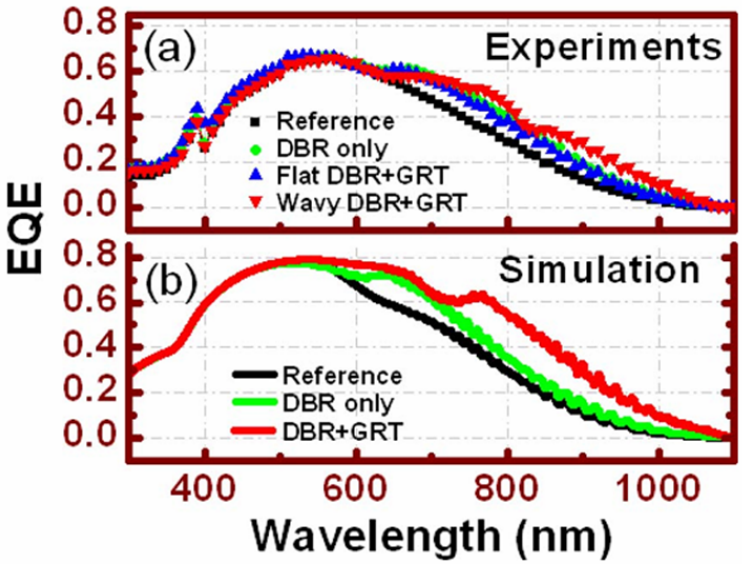

Figure 2-18: EQE for 5 μm thick Si solar cells with differing back structures. (a) Measured EQE. (b) Simulated absorption spectra.

Those previous results have experimentally demonstrated that PC based backside reflector, combining grating and DBR, can significantly enhance absorption in the red and near infrared spectral regime in thin film Si solar cells, as we can expect. However, there are still many issues and challenges related to the existing design and fabrication:

1. The active devices are based on SOI wafers, which are suitable for high efficiency cells, but not suitable for practical low-cost and large-area Si solar cell production;

2. The process flow involves many fabrication steps which are CMOS compatible but not standard for photovoltaic production, such as ion implantation, high temperature annealing, wafer bonding and chemical-mechanical polishing. Especially, interference lithography was used to fabricate the submicron grating layer. This technique can achieve well defined features, however, it cannot be used for large-scale fabrication;

3. This previous design used 1D grating, instead of 2D grating. As we discuss in Appendix A, 2D grating can obtain higher light trapping performances than 1D grating, since it can make diffracted light couple into more waveguide modes.

Therefore, there are still much room to improve both the design and fabrication technologies, in order to obtain low-cost and highly efficient thin film Si solar cells. The device structure and process should be re-designed to accommodate manufacturing. Especially, a cheap technique should be introduced to replace the lithographic method for periodic grating fabrication. In the following chapter, we will propose a simple method based on a self-assembled material called anodic aluminum oxide (AAO), which is suitable to fabricate large-area periodic submicron grating structures.

Chapter 3

Self-assembled anodic aluminum oxide (AAO)

In our designed PC light trapping structure, the periodic grating layer is one of the key components. As we mentioned in the previous chapter, a low-cost, scalable technique should be employed to fabricate this wavelength-scale periodic structure comprising two materials with different refractive indices. In this chapter, we introduce a self-assembled template material called anodic aluminum oxide (AAO), which has an ordered porous structure spontaneously formed in an electrochemical process. The structural parameters of the AAO can be controlled by different experimental conditions. In addition, we analyze the AAO structure by the fast Fourier transform (FFT) and numerically verify that it can be used as the grating layer.

3.1 Introduction of AAO

3.1.1 Anodization of aluminum

Anodization, also called anodic oxidation, is an electrochemical process that is used to form an oxide layer on the surface of metal parts. The schematic of a typical anodization setup is illustrated in Figure 3-1. It has a circuit structure similar to electrodeposition and electrolysis, consisting of power supply, anode, cathode and electrolyte. In the process, the metal parts for treatment form the anode. Cathode is usually made of inert conductors such as platinum or graphite. Usually, electrolytes are acidic solutions like phosphoric

acid and oxalic acid, but sometimes non-acidic solutions can also be used. Depending on the applications, the power supply can provide DC or AC power, operating in a constant voltage mode or a constant current mode. As the anode, the sample, which is aluminum metal in our case, is being oxidized and form an aluminum oxide layer on the surface. The anodization process has a variety of applications including metal passivation, protection coating, coloring and mechanical hardening [36].

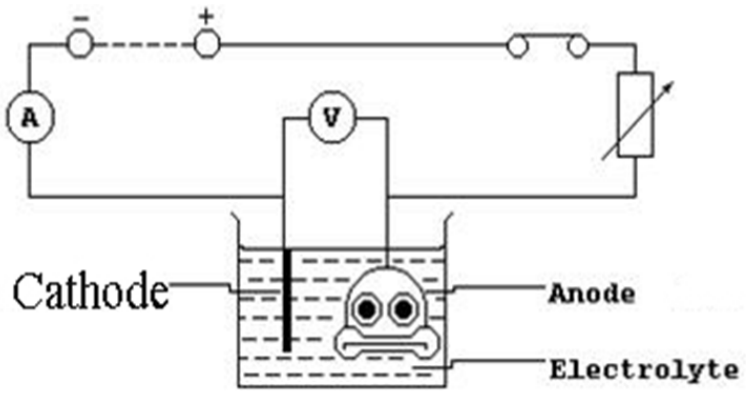

Figure 3-1: Electrochemical setup for anodization.

The chemical reactions during aluminum anodization involves a series of complicated process, and they are highly dependent on the electric power and the type of electrolyte. The simplified reactions for aluminum anodization in acids can be expressed as [5]:

$$\begin{aligned} &\text{In cathode: } 2\,H^+ + 2\,e^- \longrightarrow H_2 \\ &\text{In anode: } 2\,Al + 3\,H_2O \longrightarrow Al_2O_3 + 6\,H^+ + 6\,e^- \end{aligned} \tag{3.1}$$

3.1.2 Structure of AAO

If proper experimental conditions (electrolytes and applied voltage, for example) are selected, the formed AAO layer can exhibit a special porous structure (shown in Figure 3-2). In the porous AAO structure, straight pores are grown during the anodization, forming a close-packed near-hexagonal lattice. In the bottom of the AAO, the pores do not directly touch the un-treated Al substrate, while an Al_2O_3 barrier layer is formed in between.

Therefore, each cell in the hexagonal lattice forms a "U"-type structure. It is very difficult to fabricate an AAO structure with a perfect hexagonal lattice, while in experiments we usually obtain a porous structure with some disorder and randomness. The AAO structure can be characterized by several structural parameters, including pore period (or interpore distance), pore diameter and pore thickness.

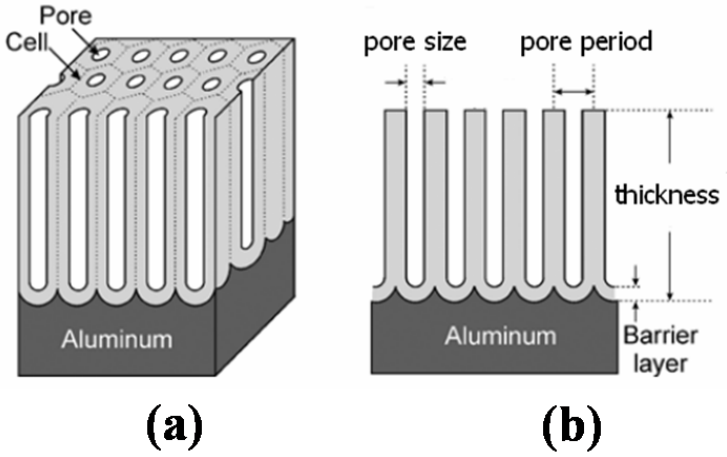

Figure 3-2: (a) Idealized structure of AAO layer on the Al surface; (b) Cross-sectional view of AAO.

Growth of the AAO layer occurs in the bottom of the pore, mainly in the interface barrier between Al metal and AAO. With the assistance of applied electric field, the top part of the barrier is dissolved in the acid, while the bottom part of the barrier is grown because of the oxidation of Al metal. If these two processed are in equilibrium, the AAO grown is in steady-state and pore can become thicker and continuously penetrate into the metal. Various models have been developed to explain the mechanisms of pore initiation and growth [5].

3.1.3 Controlling the structures of AAO: experimental results

Before implementing the AAO porous structure in a solar cell, we plan some experiments to evaluate the anodization process and obtain some guidance to control the structural parameters of AAO. Our experimental setup is photographed in Figure 3-3. The power supply is EPS 301 purchased from GE healthcare, which can provide a constant DC voltage

ranging from 0 V to 300 V. The cathode and the anode are connected to the power supply via copper wires. The cathode is made of platinum wires, and the anode is Al metal. We can use pure Al foil (polished) or Al films deposited on a non-reactive substrate (for example, at a voltage lower than 200 V we can use intrinsic silicon wafer). Here we deposit 3 μm Al film on a silicon substrate by electron beam evaporation for anodization. Both the cathode and anode are dipped into the electrolyte made of 4% (by weight) phosphoric acid. The beaker containing the electrolyte is placed on a cooling plate (Ladd Research) and the temperature is maintained at 5 °C to prevent electrical breakdown. A magnetic stirrer is used to facilitate thermal and chemical diffusion. We can control the applied DC voltage and anodization time. After anodization, we can keep the AAO sample in the electrolyte for different amounts of time, thus phosphoric acid can slowly dissolve the AAO and widen the pores.

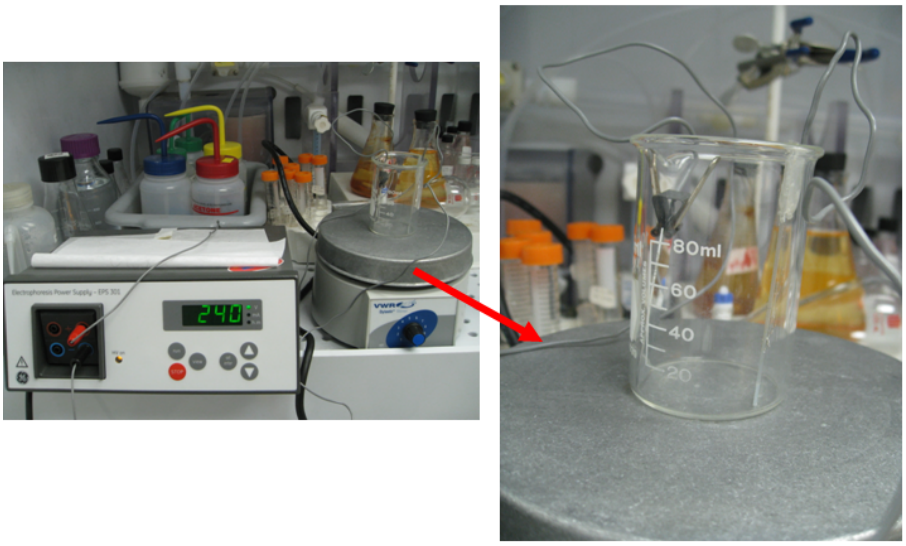

Figure 3-3: The electrochemical setup used for Al anodization in the lab.

Effect of applied voltage on pore period

First, we investigate the effect of different applied DC voltages on the pore period. We use 40 V, 80 V and 150 V, and anodization time is kept 1 hour for 3 different samples. The SEM images are shown in Figure 3-4. As we can see from the images, the AAO structures

have irregular pore distributions. Therefore, here we can only do a rough estimation of the pore period. In the following sections, we will explore the methods to obtain a more regular AAO structure and develop a more reliable method to calculate the average pore periods. We estimate the pore periods and plot them as a function of applying voltage. It is shown that the period (Λ) is proportional to the voltage (V) and we can get the relationship:

$$\Lambda \approx V \cdot 2.5 \text{ nm/V} \tag{3.2}$$

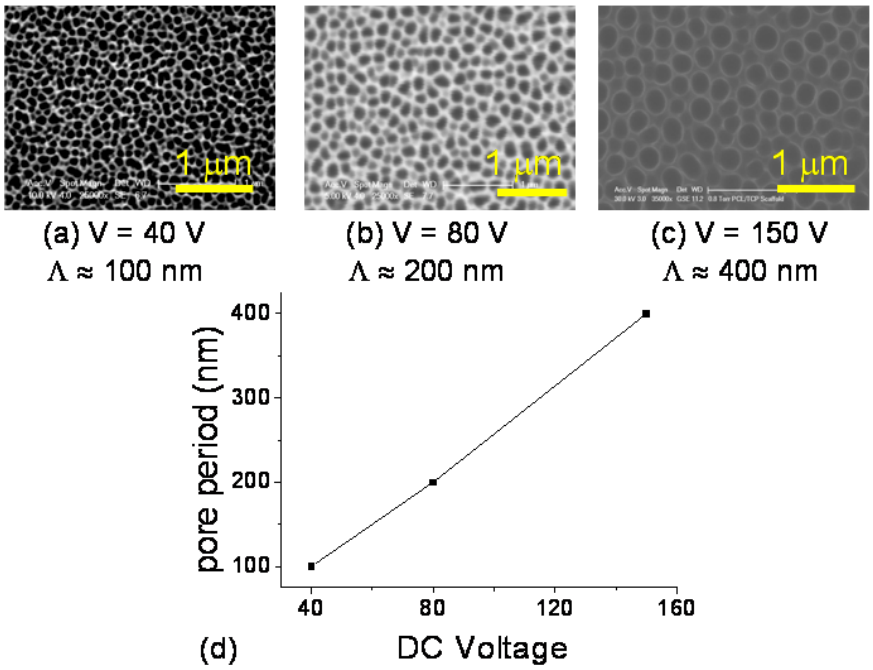

Figure 3-4: SEM images of the AAO structure (top view) after applying different voltages: (a) 40 V; (b) 80 V; (c) 150 V; (d) Plot of the relationship between pore period and voltage.

This result is consistent with literature reports. Figure 3-5 plots the relationship of applying voltage and pore period, as well as the suitable electrolytes that can be used in different voltage ranges [37]. We can observe that the voltage is the most important factor that determines the pore period, while the period is not so sensitive to the temperature and types of electrolytes. The reason for choosing different electrolytes in different voltage ranges is manifold: (1) A specific electrolyte can only obtain steady AAO growth in a specific voltage range; (2) A specific electrolyte helps form regular hexagonal pattern in a specific voltage range; (3) In higher voltage, weaker acid should be used so that electrical breakdown can be prevented. Figure 3-5 provides us a guideline on how to fabricate the optimal AAO

structure for light trapping in different solar cells based on numerical simulations.

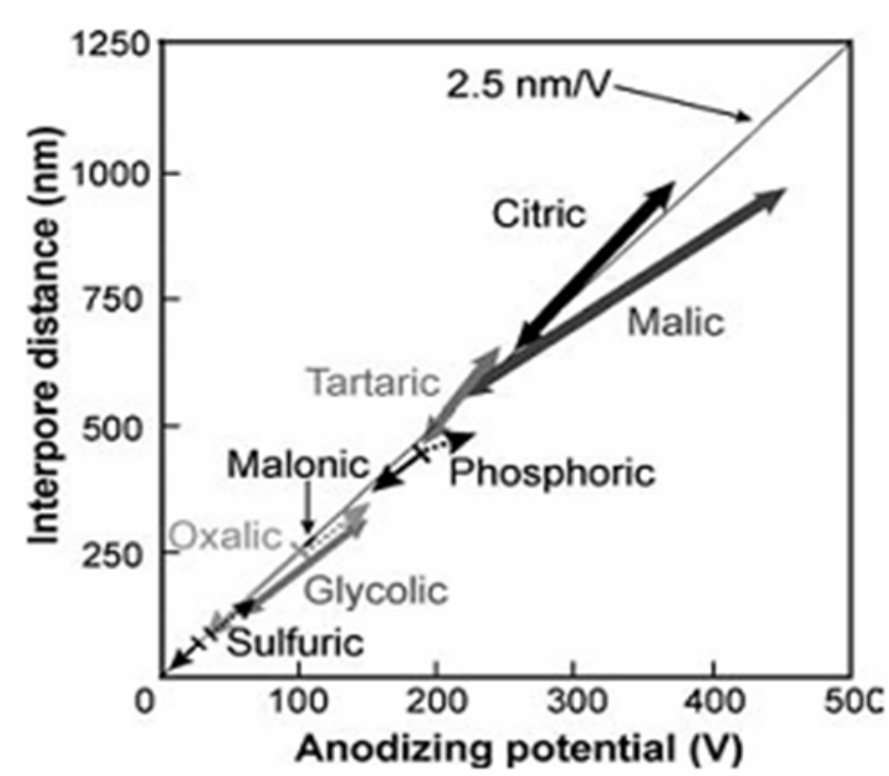

Figure 3-5: Influence of applying voltage on the pore period in various electrolytes [5].

Effect of anodization time on pore thickness

For steady-state AAO growth, the pore thickness is proportional to the anodization time if other experimental conditions such as temperature and applying voltage are kept constants. This is verified in Figure 3-6, which illustrate the cross-sectional SEM images of the AAO structure after different amounts of anodization time. Here we use a constant voltage of 150 V. The estimated growth rate is estimated to be around 20 nm/min. However, unlike the pore period, the pore thickness is also sensitive to the concentration and type of electrolytes, as well as the solution temperature [5]. Therefore, the growth rate we obtained here should not be used as a general rule but needs to be calibrated in different experimental conditions.

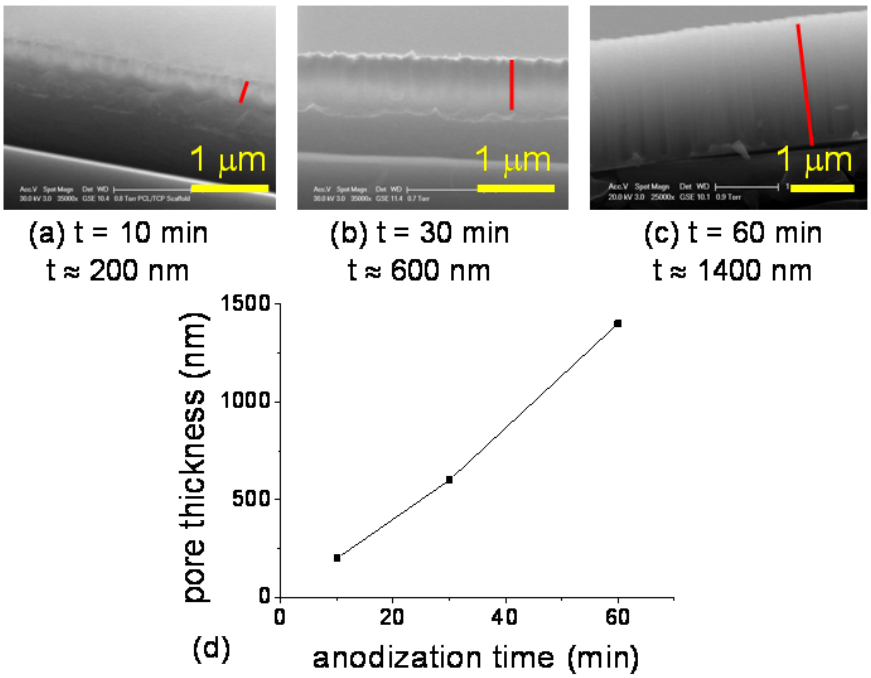

Figure 3-6: SEM images of the AAO structure (cross sectional view) after amounts of different anodization time: (a) 10 min; (b) 30 min; (c) 60 min; (d) Plot of the relationship between pore thickness and anodization time.

Effect of post etch time on pore diameter

After the anodization process, the AAO sample can be left in the electrolyte for pore widening, since the aluminum oxide can slowly dissolve in the acidic solution. Figure 3-7 plots the effect of post etching. Before the post etching, all the samples are anodized for 1 hour at a voltage of 150 V. The solution temperature is kept at 5 °C. As time goes, the pore gets larger, while the pore period remain unchanged. The pore widening rate is estimated to be around 66 nm/h. Similar to the pore growth, this rate is also highly dependent on other parameters like acid concentration and temperature.

3.1.4 Two step anodization

The SEM images shown above reveal that it is challenging to get a highly ordered pore distribution during the anodization, since the pore initiation is more or less random. However, the pore growth is not perfectly straight. During the pore growth, the pores re-organize themselves and become more regularly aligned. A two step method has been developed to obtain a more organized AAO pattern [38]. The schematic process flow is illustrated in

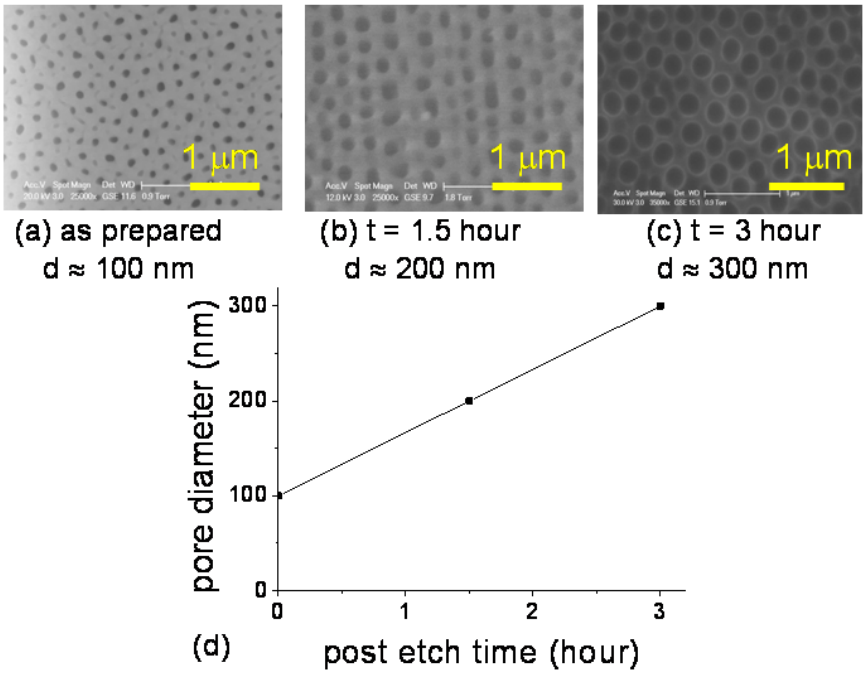

Figure 3-7: SEM images of the AAO structure (top view) after different amounts of post etch time: (a) As prepared, 0 h; (b) 1.5 h; (c) 3 h; (d) Plot of the relationship between pore diameter and post etch time.

Figure 3-8. The first anodization step forms irregular pore pattern as we saw previously. Subsequently, the AAO layer can be removed by dipping the sample in a mixed solution of of chromic acid (1.8 wt%) and phosphoric acid (6 wt%) for 5 hours at 50 °C. The solution can selectively dissolve Al_2O_3, obtaining an ordered dimple pattern on the Al surface. Then we can repeat the anodization process within the same condition as the first one. During the second anodization, pores are initiated at the center of each dimple, forming a much more regular pore distribution, as shown in Figure 3-8(c). The ordered AAO structures can be more easily characterized and have a wider applications for functional devices.

3.2 Analysis of AAO structure by fast Fourier transform (FFT)

The AAO obtained after two step anodization exhibits a nearly hexagonal pore distribution, so its structural parameters, especially the pore period, can be more easily and precisely calculated. For demonstration, here we analyze two different AAO samples obtained under different experimental conditions. Both of the samples are fabricated through two step

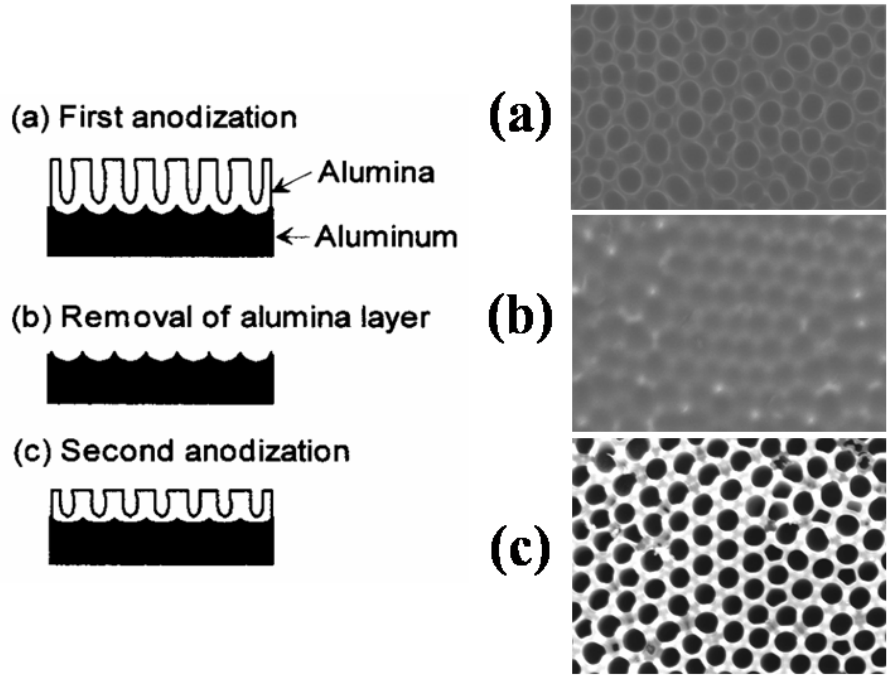

Figure 3-8: Schematic process flow for two step anodization and the corresponding SEM images. (a) First anodization, forming irregular pore distribution; (b) Removal of the AAO layer, remaining a regularly patterned Al surface with nearly hexagonal dimples; (c) Second anodization, forming a much more regular porous structure.

anodization process. One is anodized in phosphoric acid at 150 V, and the other is in citric acid at 280 V. The AAO removal process for different samples are the same, which is in a mixed solution of of chromic acid (1.8 wt%) and phosphoric acid (6 wt%) for 5 hours at 50 °C. The experimental parameters are listed in Table 3.1. Then the samples are dipped in 5 wt% phosphoric acid for suitable amounts of time to obtain the proper pore diameters.

Table 3.1: Experimental conditions for fabricating two different AAO samples.

sample	electrolyte	voltage (V)	temperature (°C)
1	4 wt% phosphoric acid	150	5
2	0.2 M citric acid	280	20

The SEM images of the obtained AAO samples are illustrated in Figure 3-9(a) and Figure 3-10(a). The corresponding 2D fast Fourier transform (FFT) images are calculated by MATLAB FFT toolbox. The obtained FFT patterns show multiple ring configurations, which are very similar to the TEM diffraction patterns for polycrystalline materials. The appearance of higher order rings suggests that the AAO structures exhibit short-range order periodicity. To derive the pore period of AAO, the averaged radial intensity distribution is

plotted as a function of reciprocal distance from the center [39]. From the first diffraction peak at g, the averaged period Λ of the near-hexagonal AAO can be determined to be [40]

$$\Lambda = \frac{2}{\sqrt{3}g} \tag{3.3}$$

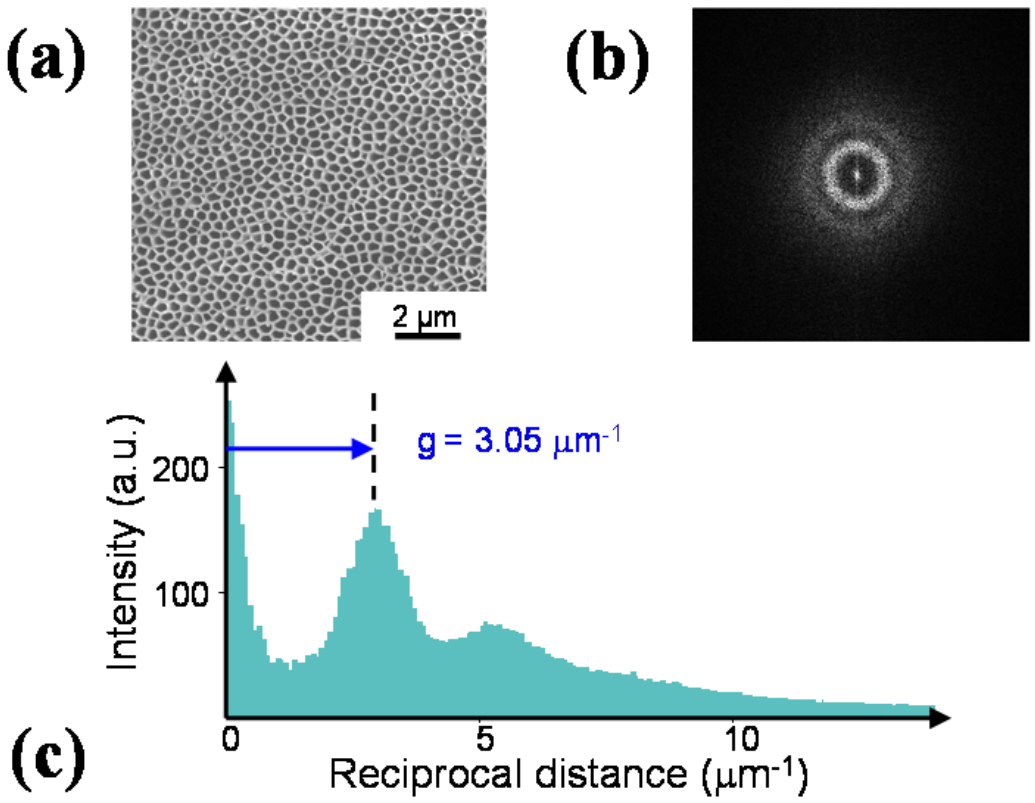

Figure 3-9: (a) SEM image of sample 1; (b) Corresponding 2D FFT image; (c) Rotational averaged radial intensity profile as a function of reciprocal distance from origin, based on the FFT result in (b).

The calculated period based on FFT analysis can be compared with the empirical equation $\Lambda \approx V \cdot 2.5$ nm/V, and tabulated in Table 3.2. We observe that the calculation results show good agreements with the empirical predictions.

Table 3.2: Calculated pore period Λ based on FFT analysis, compared with the empirical equation $\Lambda \approx V \cdot 2.5$ nm/V.

sample	voltage (V)	empirical Λ (nm)	g (μm^{-1})	calculated Λ (nm)
1	150	375	3.05	379
2	280	700	1.72	672

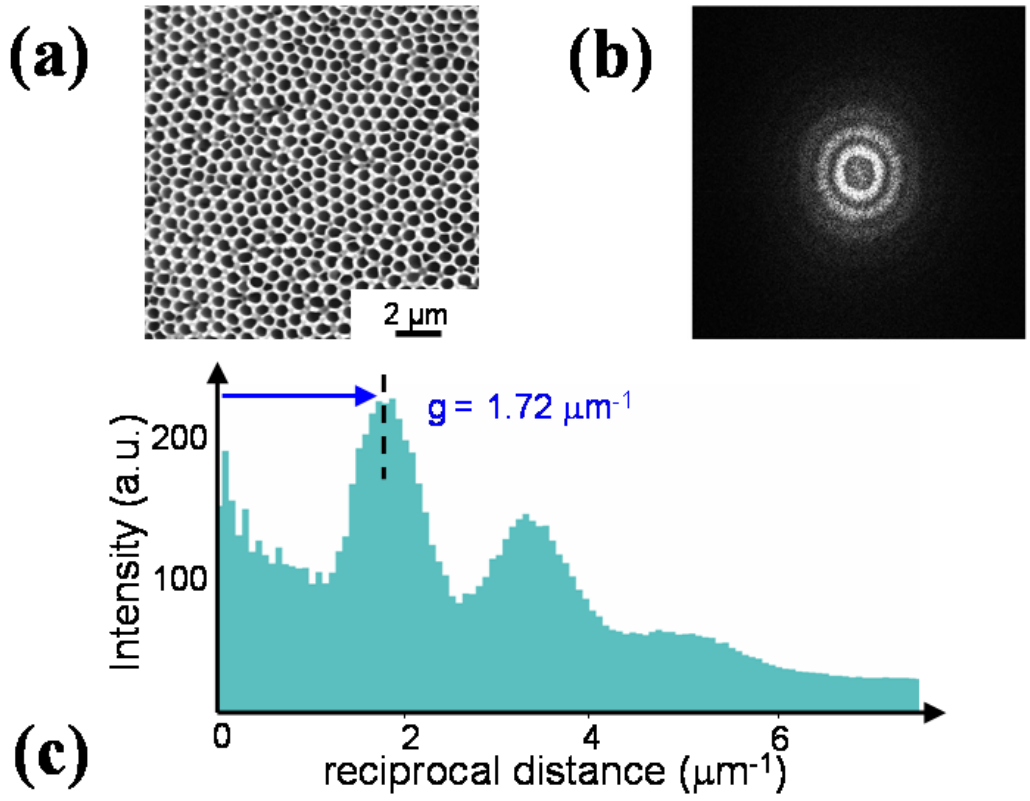

Figure 3-10: (a) SEM image of sample 2; (b) Corresponding 2D FFT image; (c) Rotational averaged radial intensity profile as a function of reciprocal distance from origin, based on the FFT result in (b).

3.3 Fabrication of ordered patterns using AAO as a template

The above results demonstrate AAO is a suitable material that provides a feasible way to fabricate ordered patterns at a low cost. However, it is still challenging to control some experimental parameters such as pore thickness, although pore period can be adjusted by tuning the applying voltage. In addition, the air-Al_2O_3 material system limits its applications, and it will be more beneficial for different functional devices if different materials can be introduced in this self-assembled structure. Here we utilize AAO as a template material, by which regular patterns made of various different materials can be fabricated.

Figure 3-11 lists the procedures of fabricating patterns using AAO as a template. First, the AAO structure is grown on aluminum foils (99.99%) using the aforementioned two step anodization method. Second, the Al substrate can be selectively removed in saturated $HgCl_2$ solution. Therefore, a thin AAO membrane is obtained, which is etched in phosphoric acid (5 wt%) to remove the barrier layer and adjust the pore diameter. Subsequently, the AAO membrane is used as a deposition mask, through which other materials can be evaporated on any substrates. Finally, the AAO membrane can be easily detached from the substrate, remaining a patterned material on the substrate, which replicates the ordered AAO structure.

The fabricated AAO membrane using our lab setup is shown in Figure 3-12. The sample with a diameter of about 1 cm is transferred onto a Si substrate. Since the membrane is attached to the substrate only by van der Waals force, it can be easily detached from the surface after deposition. In this example, the membrane is fabricated by Al anodization in citric acid under 280 V, and the period is about 700 nm. To make sure that the deposited materials can penetrate through the pores, the aspect ratio should be kept low. Here the thickness of the membrane is controlled to be around 1 μm to 2 μm.

To deposit materials we want through the AAO membrane, a suitable deposition technique should be selected. Evaporation in a high vacuum tube, either by thermal heating or electron beam (ebeam), is a good candidate since it is a ballistic process. It should be noted that the target materials should be placed right on top of the samples without tilting. Other deposition methods like sputtering and chemical vapor deposition (CVD) should not be used, since the atoms interact with the plasma gas, which inhibits the ballistic process. Figure 3-13 shows silver (Ag) and amorphous silicon (a-Si) patterns we fabricated

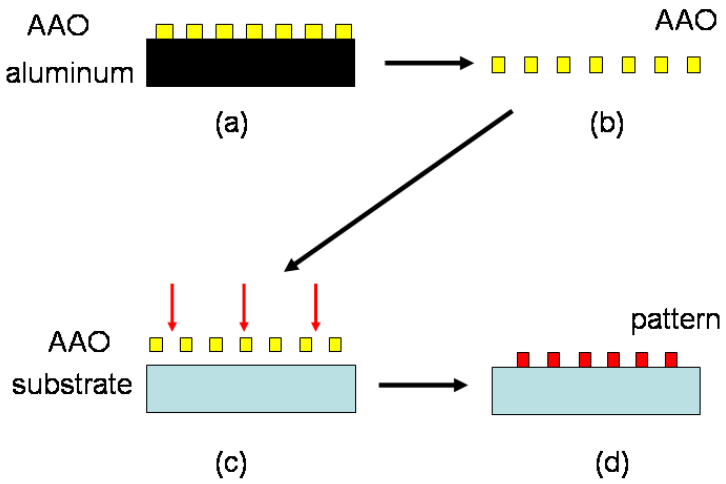

Figure 3-11: Process flow of transfer AAO pattern onto other substrates. (a) AAO grown on Al foils by two step anodization; (b) Selective Al removal and pore widening, obtaining a thin AAO membrane; (c) Evaporating other materials through the AAO membrane on other substrates; (d) Removing the AAO membrane, leaving a pattern on the substrate replicating the ordered AAO structure.

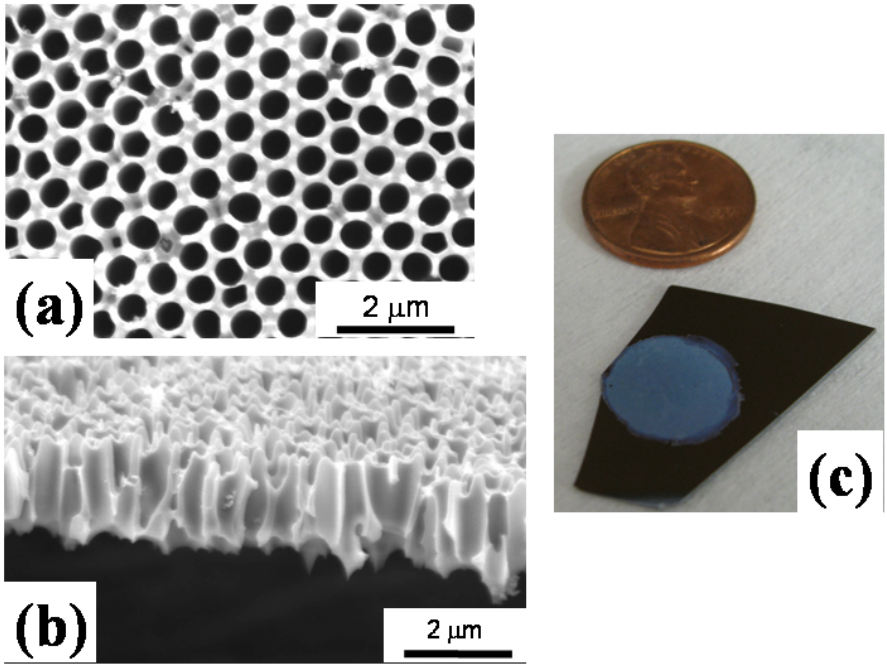

Figure 3-12: AAO membrane after Al removal and pore widening. (a) top-view SEM image; (b) side-view SEM image; (c) Photograph showing a circular AAO membrane (with a diameter of 1 cm) on a Si substrate, in comparison with a penny.

using ebeam evaporation. The SEM images clearly reveal that the deposited Ag and a-Si patterns directly replicate the nearly hexagonal AAO pore arrays.

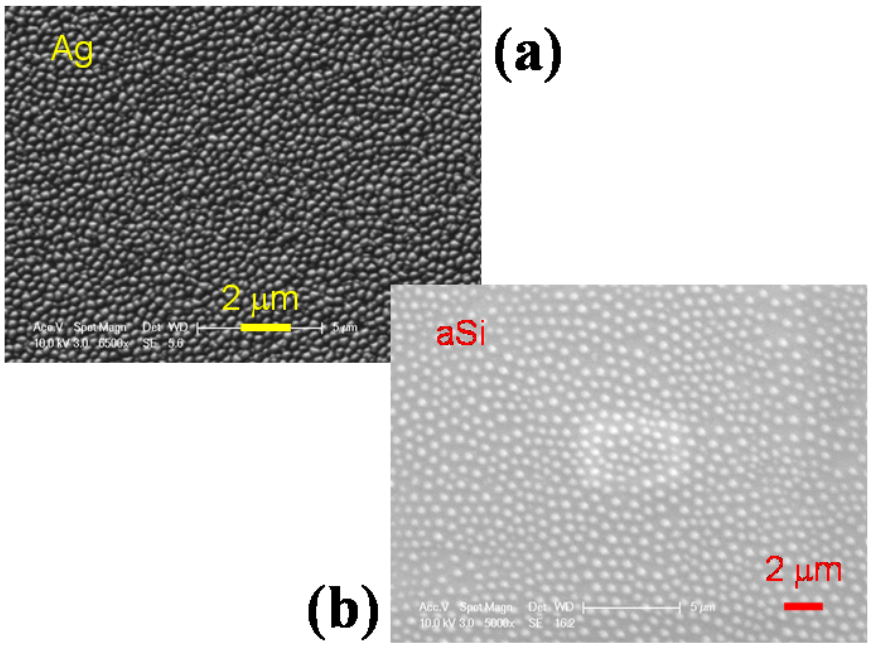

Figure 3-13: SEM images of the deposited pattern through AAO membranes. (a) Ag; (b) a-Si.

3.4 Simulation of the nearly hexagonal AAO pattern

The AAO fabrication and the pattern transfer process provide possible solutions to fabricating the PC light trapping structures at low cost. However, it is still challenging to fabricate a perfectly periodic pattern as we can make by lithographic technologies, even if we use the two-step anodization. Imperfections always exist. Therefore, it is imperative to understand how the irregularity will affect the light trapping performances, if we cannot eliminate it. To quantitatively predict the light trapping effect, numerical electromagnetic simulations based on the FDTD method are performed for 2 μm thick silicon. The simulation model is illustrated in Figure 3-14. Light is normally incident from air on a thin film active Si layer of 2 μm. The PC light trapping structure combining DBR and grating is in the backside of Si. The DBR consists of five pairs of aSi (65 nm) and SiO_2 (170 nm) layers, while the 150 nm thick grating is consisting of aSi cylinders embedded in the AAO matrix. To investigate the influences of the disorder, two types grating structures are simu-

lated and compared. Figure 3-14(b) shows the top view of the perfectly periodic structure with period $\Lambda = 380$ nm and pore diameter $D = 280$ nm. As a comparison to the perfect periodic structure, in Figure 3-14(c) a hexagonal pattern with distorted subunit cells is also simulated to further approach the real AAO structure.

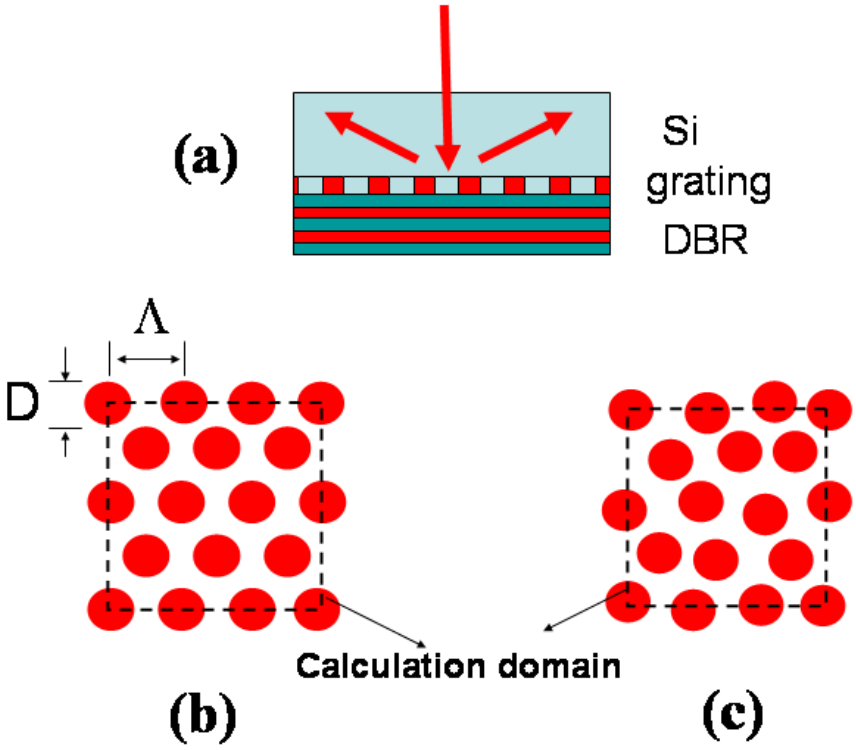

Figure 3-14: (a) Schematic cell structure with grating and DBR in the backside. Grating is composed of aSi rods embedded in Al_2O_3 matrix. Top view: (b) perfectly periodic hexagonal grating (PG) with period Λ and pore diameter D and (c) simulated AAO grating with disorder. FDTD calculation domains are also shown by dashed boxes. Periodic boundary condition is used for the super cell approach.

With the refractive indices of different materials given in [29], we calculate absorption spectra of the silicon layers with different backside structures, which are plotted in Figure 3-15. As expected, at wavelengths between 0.5 μm and 1.1 μm, stronger absorption peaks for silicon with DBR (green color) are caused by thin film Fabry-Perot interference. When the grating layer (either the periodic grating or the real AAO grating) is added, more and stronger resonance peaks are induced, and the absorption enhancement is even more significant (blue and red color) since the light can be diffracted into oblique angles to enhance the absorption length. Because of the difference in the pore configurations, these two types

of gratings show resonance peaks with different positions and magnitude in the curves.

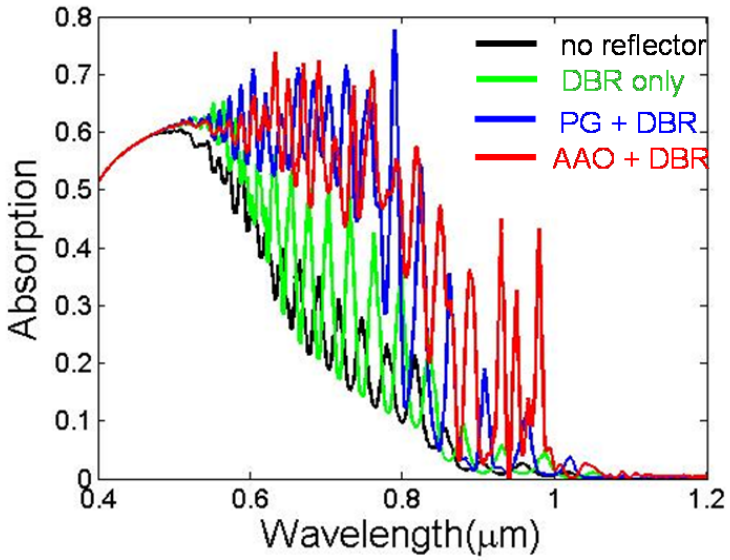

Figure 3-15: Simulated absorption spectra for the 2 μm thick silicon with different backside structures.

To quantitatively compare the performances of different simulated structures, we calculate short-circuit current densities (J_{sc}) based on the simulated absorption spectra in Figure 3-15 as a figure of merit based on the equation:

$$J_{sc} = e \int_0^{\lambda_g} s(\lambda) A(\lambda) d\lambda \tag{3.4}$$

where $A(\lambda)$ is the calculated absorption spectrum and $s(\lambda)$ is the standard AM1.5G solar spectrum [33]. The calculated J_{sc} are summarized compared in Table 3.3. Compared to the bare silicon without any reflector on the backside, the DBR gives rise to a 23% relative enhancement. The combination of periodic grating (PG) and DBR structure indicates a 51% enhancement, while the AAO grating we fabricated is capable of achieving an even higher increase (53%). These results demonstrate that the perturbed gratings fabricated through AAO structure can at least have a similar light trapping effect as the perfect periodic gratings fabricated by lithography.

Table 3.3: Calculate short-circuit current density J_{sc} for solar cells in Figure 5-10.

cell types	J_{sc}(mA/cm^2)	relative enhancement
no reflector	12.3	-
DBR only	15.1	23%
PG + DBR	18.3	51%
AAO + DBR	18.8	53%

3.5 Conclusion

In this chapter, we have reviewed the self-assembled AAO technology. We demonstrate that this porous structure can be well controlled by tuning the anodization process. The structural parameters such as pore period, diameter and thickness can be adjusted under different experimental conditions, like electrolytes, applying voltage and anodization time. Furthermore, we introduce the two step anodization method to obtain AAO structures with more organized hexagonal patterns. In addition, we use FFT analysis to calculate the pore period for the obtained ordered AAO. The ordered AAO pattern can also be transferred onto other materials by evaporation. Finally, we have done some preliminary study on the influences of the irregularity on the light trapping effect. We prove that the slightly perturbed AAO pattern has a light trapping effect comparable to (or even higher than) the perfectly periodic structures.

Chapter 4

Light trapping in c-Si wafer-based photoconductors by self-assembled PC structure

In previous chapters, we have proposed using the designed PC structure by self-assembly for effective light trapping in thin film Si solar cells. Before integrating this new technique with an actual photovoltaic device, we choose a simple Si wafer-based photoconductor to demonstrate the light trapping idea.[1]

4.1 Fundamentals of Si photoconductors

For a uniform semiconductor material like Si, its conductivity can be described as

$$\sigma = n_0 e\mu_n + p_0 e\mu_p \tag{4.1}$$

where n_0 and p_0 are concentrations of free electrons and holes in thermal equilibrium, and μ_n and μ_p are mobilities for electrons and holes, respectively. In other words, the conductivity σ is directly proportional to n_0 and p_0 when μ_n and μ_p are constant. Under light illumination, absorption and interband transition can generate excess electrons and holes, thus change the conductivity to

[1]This work has been published as a part in "Integration of Self-Assembled Porous Alumina and Distributed Bragg Reflector for Light Trapping in Si Photovoltaic Devices," IEEE Photonics Technology Letters, **22**, 1394 (2011) [41]. Copyright IEEE. Reproduced with permission.

$$\sigma = (n_0 + \delta n)e\mu_n + (p_0 + \delta p)e\mu_p \tag{4.2}$$

Therefore, the material becomes more electrically conductive. This phenomenon is called photoconductance, and the conductivity difference is called photoconductivity,

$$\delta\sigma = \delta n e\mu_n + \delta p e\mu_p \tag{4.3}$$

If we assume each electron and hole pair is generated by one absorbed photon, we can deduce that the photoconductivity is proportional to the incident light intensity and absorption efficiency of the device. Therefore, a photoconductor exhibits a similar dependence on photon absorption as a photovoltaic device. In addition, fabrication of photoconductors is much easier and more flexible than that for photovoltaic devices, since no doping or pn junctions are required. Photoconductors have been widely used in various applications for photon detection [42].

4.2 Device fabrication

The process flow for fabricating the Si photoconductor with PC light trapping structures is illustrated in Figure 4-1. The details for each step are discussed below.

4.2.1 Si photoconductor

Since thin-film Si devices cannot be easily fabricated with PC integration, here we use single crystalline Si wafers. For thick Si wafers, single pass absorption is very high for most wavelengths, so the light trapping effect is only observable in wavelengths very close to bandgap. The Si wafers are slightly p-doped and double-side polished, with a thickness of 300 μm. Al metal pads are evaporated on top of the Si wafers, forming ohmic contacts for the photoconductor.

4.2.2 AAO process

To fabricate the 2D AAO grating via self-assembly, a 150 nm thick aluminum (Al) film is deposited on the backside of the silicon wafer. Then the Al film is anodized in a 4 wt% phosphoric acid at a voltage of 150 V until the Al film is completely oxidized to aluminum

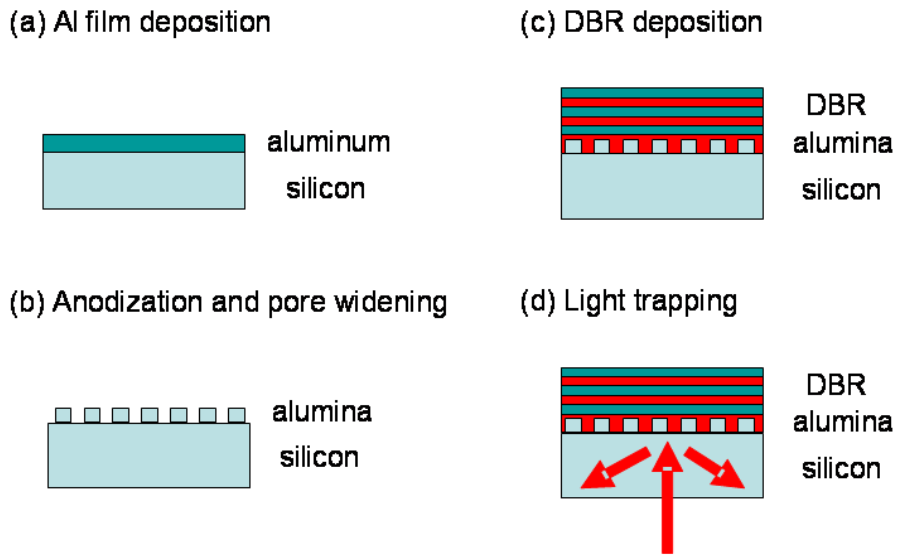

Figure 4-1: Process flow for fabricating the Si photoconductor with PC structure for light trapping.

oxide. During anodization, the temperature is maintained at 5 °C to prevent electrical breakdown. Afterwards, the samples are immersed in 5 wt% phosphoric acid for about 2 h at room temperature to widen the pore size and remove the barrier layer.

The inset of Figure 4-2 shows a scanning electron microscope(SEM) image of the porous alumina structure after the pore widening treatment. The regularity of the pore distribution is revealed by the 2D FFT technique mentioned in Chapter 3. To derive the characteristic length scale of AAO, the averaged radial intensity distribution is plotted as a function of distance from the center. From the scattering peak at the characteristic spatial frequency of $g_0 = 3.05\ \mu m^{-1}$, the average pore-to-pore distance of the near-hexagonal AAO can be determined to be $L = \frac{2}{\sqrt{3}g_0}$, which is about 380 nm. The average pore diameter of AAO is determined from the SEM image to be about 280 nm.

4.2.3 DBR deposition

Five pairs of alternating amorphous Si (65 nm) and SiO_2 (170 nm) layers are deposited by plasma enhanced chemical vapor deposition (PECVD) to fill the pores and form the DBR. We test the performance of the planar DBR and the measured reflectance is illustrated in

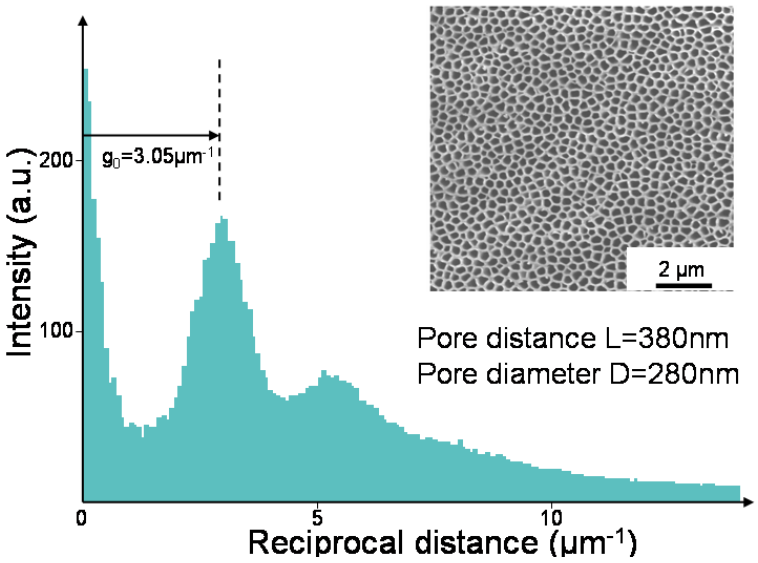

Figure 4-2: FFT intensity profile of SEM image as function of reciprocal distance from origin, from which interpore distance of AAO is derived. Inset shows SEM image of AAO after pore widening. Averaged pore distance Λ and pore diameter D are also shown.

Figure 4-3, in comparison with the calculated results. The measurement and calculation show a good agreement, with a photonic bandgap from 0.75 μm to 1.3 μm. Within this gap, the obtained reflectivity is close to 100%. For thick Si wafers, light trapping is effective near the Si bandgap (between 0.9 μm and 1.1 μm). Therefore, this DBR is suitable for the Si photoconductor we fabricate above.

4.3 Experimental results

Before we do the measurements, we estimate the magnitude of the generated photocurrents. The intrinsic Si wafers we use have a resistivity of about 10 $\Omega \cdot$ cm, and the distance between two metal contacts is around 0.1 cm. We can also assume the cross section area for current flow is about 0.01 cm^2. Therefore, the Si resistance in our measurement is

$$R = \rho \frac{L}{A} \approx 100\ \Omega \tag{4.4}$$

If we apply a bias of 1 V, the dark current (without illumination) is about $I_{dark} = V/R = 10$ mA. When we are measuring the photocurrent, we have to measure the current at monochromatic illumination. Therefore, we use a monochromator to split the spectrum of white light and generate a light beam with a single wavelength. For the monochromator

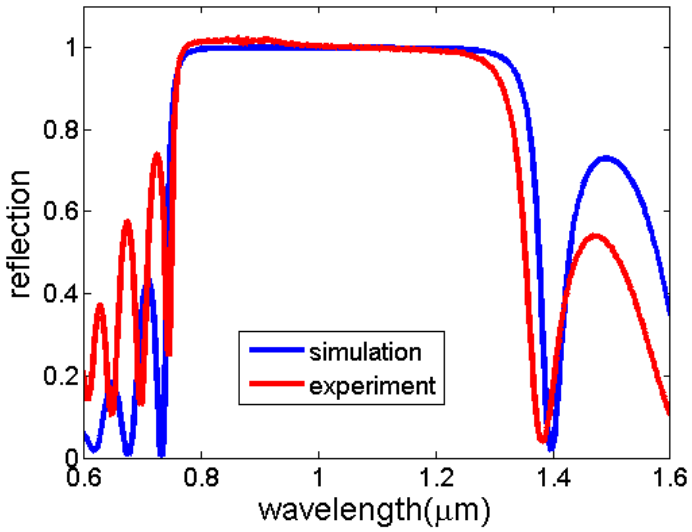

Figure 4-3: Comparison of the measured and calculated reflectivity spectra for DBR.

and light source we are using, the incident power P at each wavelength is about 1 μW. If we assume the wavelength is 1 μm, the absorption is 100% (usually this is very difficult to reach), the photocurrent at each wavelength is $I_{ph} = \frac{eP\lambda}{hc} \approx 1$ μA, which is much smaller than the dark current. Therefore, it is very difficult to capture such a small signal from a static current measurement. Here we implement a lock-in amplifier to capture this current difference using a dynamic measurement.

Figure 4-4 shows the schematic for the instruments we use for photo response measurement [43]. A white light source is generated by a halogen bulb, coupled to a monochromater (H20 IR Jobin Yvon). The monochromator can be remotely controlled to select a specific wavelength (with a spectral width of around 10 nm) from 0.4 μm to 1.1 μm. Subsequently, the monochromatic light is passing through a chopper controlled by a lock-in amplifier. The chopping frequency is fixed to be 40 Hz. The modulated light is focused on the photodetector, which is the Si photoconductor in our case. The captured response (photo current), which is also modulated at the chopper frequency, can be integrated within a fixed time constant and therefore amplified. The lock-in amplifier is a very useful tool that can extract a signal in an extremely noisy background.

The measured photoconductive response for samples with different backside structures are shown in Figure 4-5. Here an arbitrary unit is used. Since photons at short wavelengths (smaller than 1 μm) are completely absorbed by the thick active silicon layer within one

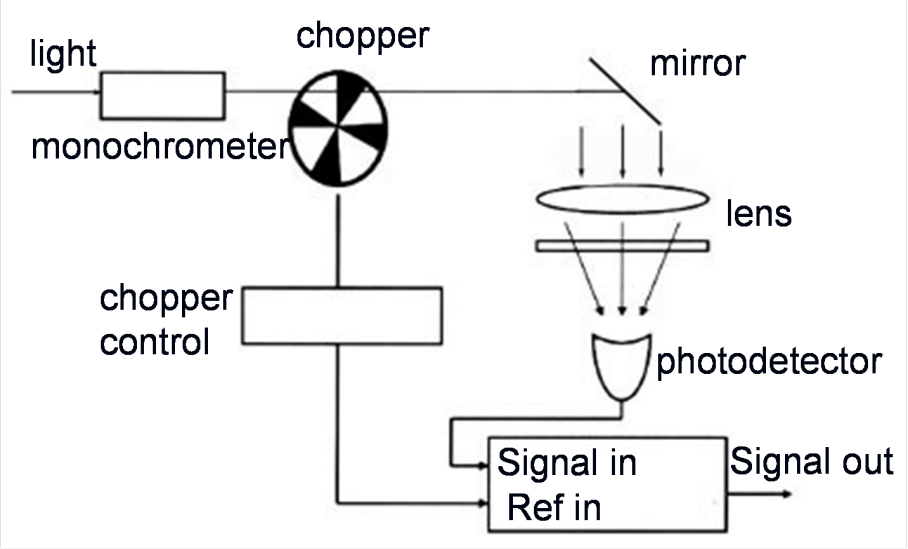

Figure 4-4: Schematic of the setup used for photo response measurement.

pass, the light trapping effect cannot be observed in this range and the photoresponses are very similar for all the different samples. Above 1 μm, an increase in the photoresponse can be clearly observed for a backside DBR structure, while the integration of an AAO and DBR can achieve even higher performance, in agreement with our predictions.

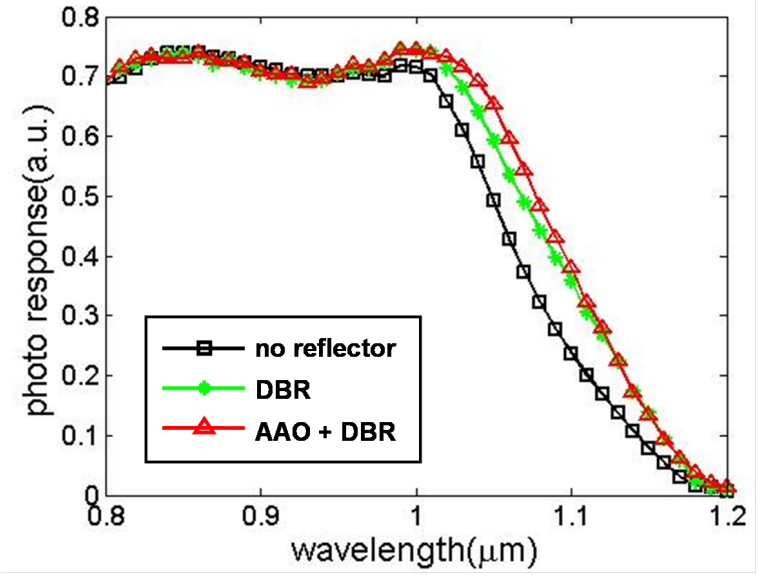

Figure 4-5: Measured photoconductive spectral response of the Si photoconductors with and without DBR and AAO+DBR on backside of the devices.

4.4 Conclusion

In this chapter, we perform photoconductance measurements on thick Si wafer-based photoconductors to demonstrate the light trapping effect of the self-assembled AAO grating and DBR. The experimental results show the enhancement of photo collection near the Si band edge, which confirms that the AAO and DBR structures can be applied for optical path length increase. Considering a thin-film Si cell with a thickness of several micrometers, the efficiency increase would be much more significant. Using the PC structures to improve the performances for thin-film Si solar cells will involve more works. For example, the structural parameters like grating period and thickness should be optimized to boost the cell efficiency as much as possible. In addition, fabrication compatibility issues should be taken into account, to implement the AAO structures without any damage to the active devices. The design and fabrication of PC structures for thin-film Si cells will be discussed in next chapter.

Chapter 5

Design and fabrication of light trapping structures for thin-film Si solar cells

In previous chapter, we have experimentally demonstrated the light trapping effects of our proposed PC structures on thick Si wafer-based photoconductors. A Si photovoltaic device, especially a thin-film Si device, is much more complicated than simple photoconductors and involves more complex fabrication technologies. In this chapter, we present the design and fabrication of PC structures for thin-film Si solar cells. We first begin with the fabrication and measurements of conventional thin-film amorphous Si (a-Si), microcrystalline Si (μc-Si) and micromorph Si solar cells. We then calculate and optimize the performances of PC on μc-Si cells. Finally, we experimentally implement the optimized light trapping structures into μc-Si cells and measure the cell performances, demonstrating the efficiency improvement and the light trapping effects of PC.[1]

5.1 Introduction of thin-film Si solar cells

Although the current PV market is dominated by thick Si wafer-based technology, thin-film Si cells have become an emerging field because of the lower cost and potential for

[1]Part of the work in this chapter has been published in "Design and Non-lithographic Fabrication of Light Trapping Structures for Thin Film Silicon Solar Cells," Advanced Materials, **23**, 843 (2011) [44]. Copyright Wiley-VCH Verlag GmbH & Co. KGaA. Reproduced with permission.

large scale production. Various types of thin-film Si solar cells have been invented and fabricated, including single crystalline Si (c-Si), polycrystalline Si (poly-Si), amorphous Si (a-Si), microcrystalline Si (μc-Si) and micromorph Si cells. Several methods are being applied for thin-film Si cell fabrication, such as plasma enhanced chemical vapor deposition (PECVD), hot wire chemical vapor deposition (HWCVD) and layer transfer process (LTP) [45, 46]. Here we mainly focus on PECVD technique, since it has been applied in industrial manufacturing and is available in conventional and standard cleanroom process.

5.1.1 Device structures and fabrication

Figure 5-1 shows the typical layouts for various types of thin-film Si solar cells fabricated by PECVD technique. A complete thin-film Si solar cell consists of several layers: a substrate, front contact, back contact, and a pn junction. Here we use a superstrate approach, in which transparent glass plates are used on top of the actual devices as substrates, and the incident light is from the top of glass. Substrate approaches can also be used for thin-film Si solar cells, where glass or stainless steel are used as bottom substrates [47]. Transparent conductive oxides (TCOs) are deposited by sputtering or CVD process on glass as front contacts. The conventionally used TCOs can be indium tin oxide (ITO), fluorine doped tin oxide (SnO_2:F) and aluminum doped zinc oxide (ZnO:Al). Then a vertical p-i-n junction made of a-Si or μc-Si is formed as the active homojunction device by PECVD process. Usually the highly dope p and n regions are very thin (about 10 nm) so that the recombination loss can be minimized. We can also make a double junction cell comprising both a-Si and μc-Si p-i-n junctions, which is called micromorph Si cell [3]. Three-junction (Tandem) a-Si/μc-Si/a-Ge cells have also been proposed [48]. Again, TCOs are deposited as back contacts. Finally, a highly reflective layer is placed in the bottom as backside mirror. This layer can be made of metals like silver or aluminum, or white paint with dielectric particles [49].

5.1.2 Device characterization techniques

To obtain the solar cell performances, several important device characteristics should be measured, including current-voltage (IV) relationships and external quantum efficiency (EQE) spectra. Figure 5-2 shows the draft of instrumental setup to do these measurements. To minimize the influences of contact resistances, we utilize a four-point probe station, in

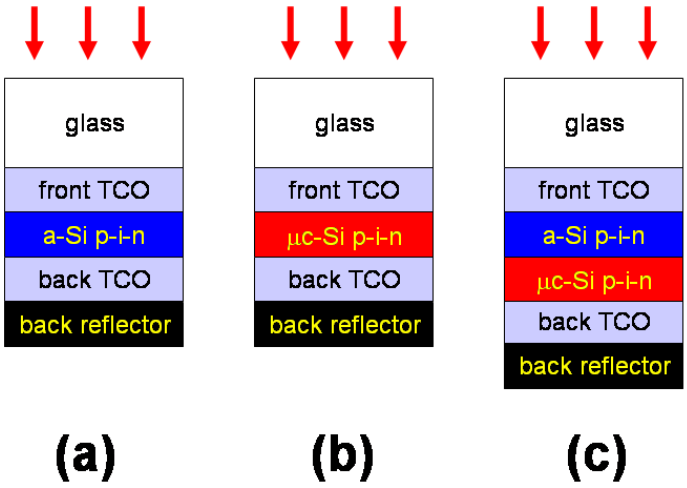

Figure 5-1: Structures for different types of thin-film Si solar cells fabricated by PECVD technique. (a) a-Si; (b) μc-Si; and (c) micromorph Si. Sunlight is incident from the top of glass plates.

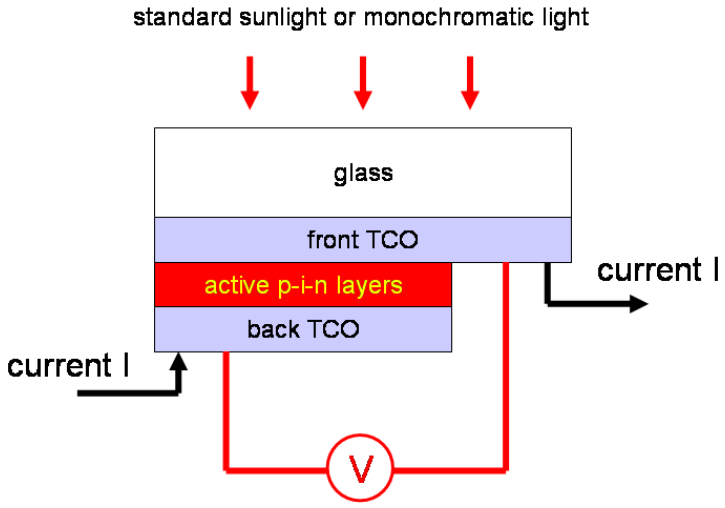

Figure 5-2: Instrumental setup for solar cell characterizations. The device is place on a four-point probe station. When the incident light is standard sunlight from a solar simulator, the setup is used to take current-voltage (IV) measurement. When the incident light is monochromatic light, the setup is used to measure photocurrent at zero bias and the external quantum efficiency (EQE) can be deduced.

which the current and voltage are measured from different channels. The incident light can be tuned to white light with standard Air Mass 1.5G spectrum [33] or monochromatic light with a single wavelength. If we want to do IV measurement and calculate the cell efficiency, we use a 1200 W Oriel solar simulator passing through a standard AM1.5G filter (Sciencetech Inc.). The incident light intensity is referenced by an NREL calibrated standard solar cell. A Keithley 2425 source meter is used to inject different current to the cell, while the corresponding voltage is measured independently from the other two channels. We define current density $J = I/A$, where A is the device area. From the measured JV curve under illumination, we can obtain several important figures of merit for solar cells including J_{sc}, V_{oc}, FF and efficiency.

External quantum efficiency (EQE) characterize the ratio of the number of collected charge carriers to the number of incident photons at a specific wavelength. If we want to measure the EQE spectra, monochromatic light is generated by passing the white light source to a H20 IR monochromator, scanning from 400 nm to 1200 nm. In this case, we only need to measure the generated photocurrent at each wavelength, so we fix the bias to 0 V and measure the current density $J(\lambda)$. If the incident spectrum from the monochromator is known to be $P(\lambda)$ (in watt per unit area), we can calculate the EQE:

$$\mathrm{EQE}(\lambda) = \frac{J(\lambda)}{P(\lambda)} \cdot \frac{hc}{e\lambda} \tag{5.1}$$

5.1.3 Device performances

Three types of thin-film Si solar cells are illustrated in Figure 5-1. The materials and layer thicknesses we use are: 4 mm glass, 1 μm ZnO:Al as front contact and 0.4 μm ZnO:Al as back contact. For the a-Si cell, the p-i-n active layers are 10 nm p-type a-Si, 350 nm intrinsic a-Si and 25 nm n-type a-Si. For the μc-Si cell, the p-i-n active layers are 15 nm p-type μc-Si, 1500 nm intrinsic μc-Si and 18 nm n-type μc-Si. The micromorph cell has both p-i-n a-Si and p-i-n μc-Si junctions, and the corresponding thickness of each layer is identical to the single junction cells. In commercial products, the front and back TCO layers are intentionally textured to enhance optical scattering and cell efficiency. Here untextured devices are used, since we want to demonstrate the light trapping effects of our proposed PC structures and exclude other effects. Performances for different types of textures will be compared and discussed later.

Figure 5-3 plots the measured current voltage relationship for the μc-Si, a-Si and micromorph Si cells. The calculated short circuit current density (J_{sc}), open circuit voltage (V_{oc}), fill factor (FF) and efficiency are summarized in Table 5.1. The a-Si cell shows higher performances compared to the μc-Si cell (efficiency 5.24% versus 1.98%), because the a-Si solar cell technology has been developed for a long time and the process is more optimized, while the μc-Si cell technology is an emerging one and more efforts are needed to optimize its performance. The a-Si cell also has a higher V_{oc} since the bandgap for a-Si is larger (about 1.7 eV) than crystalline Si (1.1 eV). This is also reflected from the measured quantum efficiency spectra, where the a-Si cell shows a lower cutoff wavelength than the μc-Si cell.

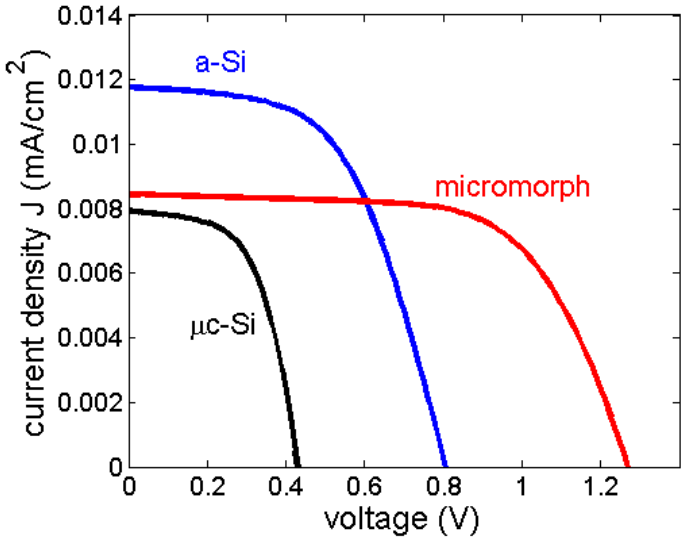

Figure 5-3: IV characteristics measured under AM1.5G spectrum for μc-Si, a-Si and micromorph Si cells.

Table 5.1: Measured characteristics for μc-Si, a-Si and micromorph Si cells.

	J_{sc}(mA/cm^2)	V_{oc}(V)	FF	efficiency η (%)
μc-Si	7.95	0.43	0.58	1.98
a-Si	11.8	0.81	0.55	5.24
micromorph	8.46	1.27	0.65	6.93

IV and EQE measurements are also performed for the micromorph cell. As shown in Figure 5-3 and Table 5.1, the micromorph cell shows the highest efficiency since it takes the advantages of both the a-Si and μc-Si junctions. Due to the serial connection, the V_{oc} for the micromorph cell is the sum of that for the individual a-Si and μc-Si cells, while the

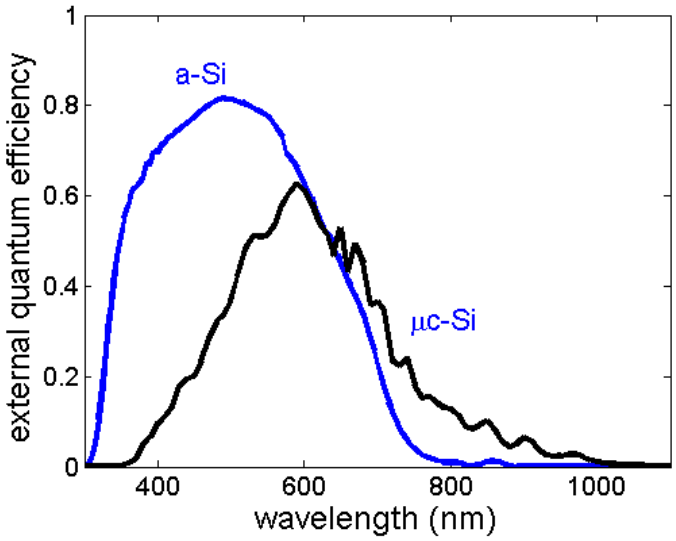

Figure 5-4: EQE spectra using monochromatic light from 300 nm to 1100 nm for the μc-Si and a-Si cells, respectively.

J_{sc} is limited by the junction that has a lower value. The EQE spectra is illustrated in Figure 5-5, with the photon response measured separately for the individual a-Si and μc-Si junctions. Due to the current match issue, the experimental setup for measuring the EQE of tandem cells is more complicated than that for a single junction device. The current of one junction should be saturated first with a probe light, while the response of the other junction can be measured using monochromatic light. For example, an intense green light beam ($\lambda = 400$ nm) is used to saturate the top a-Si cell in order to measure the EQE for the bottom μc-Si cell. Similarly, when measuring the EQE for the top a-Si cell, the bottom μc-Si cell is saturated by an intense infrared light beam ($\lambda = 750$ nm). The overall EQE can be obtained by combining the spectra for the individual cells.

5.2 Design and optimization of PC structures for thin-film μc-Si solar cells

Based on the device performances we measure in previous section, we can start to design the PC structures for efficiency improvement. The a-Si cell has a cutoff wavelength of about 700 nm, above which no EQE can be observed. Also, the band structure for a-Si is like that of a direct bandgap semiconductor, which means the absorption is relatively high above the bandgap compared to crystalline Si. In addition, the PC structures we propose also

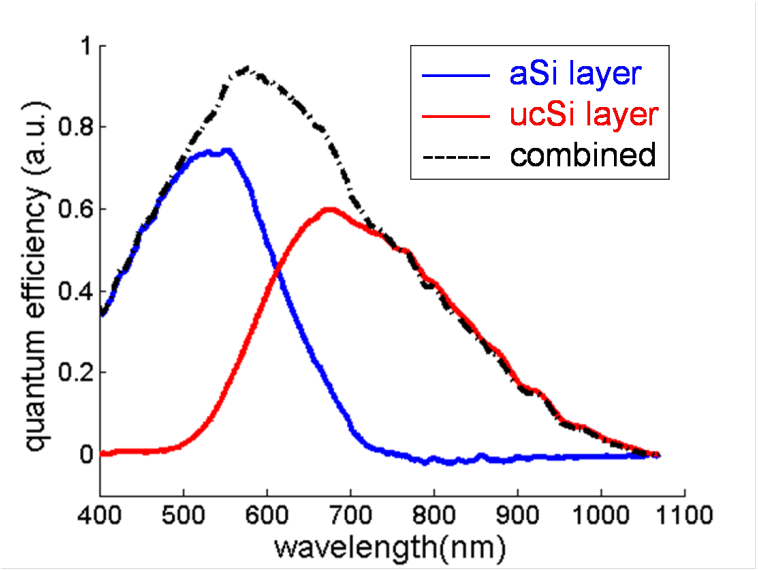

Figure 5-5: EQE spectra using scanning monochromatic light as well as a saturation probe light, separately measured for the μc-Si junction and a-Si junction in the micromorph cell.

contain a-Si in both the grating and DBR layers. The PC is highly absorptive below 700 nm, introducing significant parasitic loss. Therefore, a-Si cell is not a suitable device for our proof of concept, unless we find an alternative material for a-Si in our PC. The micromorph Si solar cell is a tandem junction cell, including two p-i-n junctions serially connected. Therefore, current match issues should be considered. If the a-Si top cell limits the overall current, light trapping effects are very difficult to detect even when the photocurrent in the μc-Si bottom cell is greatly improved. As a result, the μc-Si cell is the best candidate for our design and experimental demonstrations, because it has similar optical constants as single crystalline Si, and light trapping issue occurs mainly in the near-IR regime. In addition, it has a single junction so no current match issues are involved. Therefore, here we implement our PC structures into the μc-Si cells for design and demonstration.

In our model, we use the FDTD method [31] to simulate the optical absorption in the μc-Si cells.[2] As shown in Figure 5-6, the active device is similar to what we present in Figure 5-1. The thicknesses for front and back ZnO layers are mentioned in previous section. Here we neglect the thin p-type and n-type μc-Si layers, only assume a 1500 nm thick μc-Si layer interposed between the two ZnO layers. The light trapping configuration includes a self-assembled 2D hexagonal pattern as a grating layer, as well as a DBR. Optical

[2]We use a commercially available software from `http://www.rsoftdesign.com/products.php?sub=Component+Design&itm=FullWAVE`.

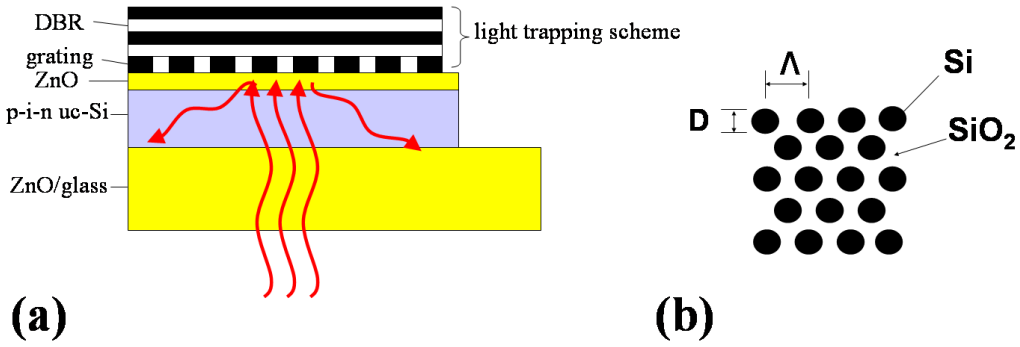

Figure 5-6: (a) The device layout and the schematic light trapping effect induced by integrating our designed PC structure comprising a self-assembled 2D grating and a DBR on the backside. (b) Top view of the grating layer, which has a hexagonal Si pattern embedded in SiO_2 matrix with period Λ and rod diameter D.

constants (refractive index n, extinction coefficient κ) for all the materials except ZnO:Al are obtained from the Ref. [29]. Here we assume μc-Si has similar optical constants as crystalline Si. The optical constants of ZnO:Al is measured by ellipsometry and shown in Figure 5-7. With all the structural parameters and material properties, we can numerically simulate the absorption in the active μc-Si layer $A(\lambda)$ for different solar cell structures. To compare the performances for different devices, we use the short-circuit current density as the figure of merit:

$$J_{sc} = e \int A(\lambda) S(\lambda) d\lambda \tag{5.2}$$

Here $S(\lambda)$ is the AM1.5G spectrum, and we assume each absorbed photon can generate one electron-hole pair, meaning the internal quantum efficiency is 100%. Therefore, J_{sc} is critically dependent on the light trapping of cells, and we will use it as the figure of merit to compare different light trapping structures. In our design, other device properties like V_{oc} and FF are not sensitive to the back structure, so the cell efficiency is almost directly proportional to J_{sc}. The structural parameters should be carefully designed to increase the photon absorption in the red and near-IR range in order to achieve highest performance.

5.2.1 DBR optimization

We use 5 pairs of a-Si and SiO_2 as the DBR layer, which can be deposited through the PECVD method at 150 °C. The target range for the photonic bandgap is slightly different

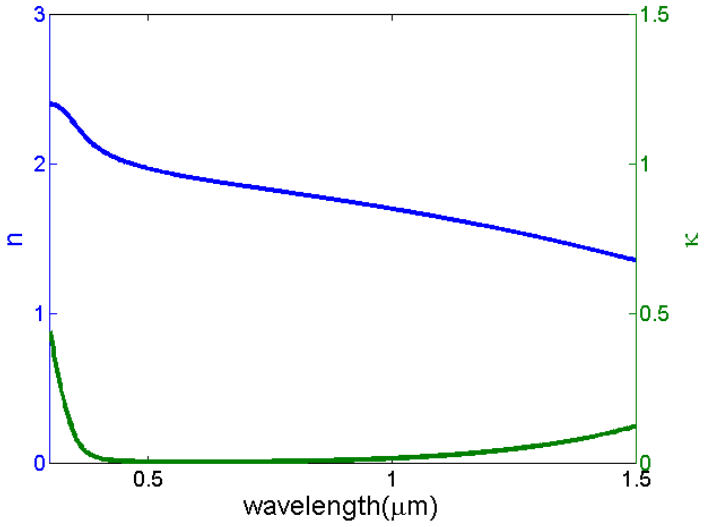

Figure 5-7: Measured refractive index n and extinction coefficient κ for ZnO as a function of wavelength.

from what we present in previous chapter, since we aim at slightly shorter wavelengths. We choose 40 nm a-Si and 130 nm SiO_2 for each layer, and we test the reflectivity on a planar glass substrate. For comparison, a planar 200 nm aluminum film deposited by PECVD is also measured. The reflectivity of the DBR is measured using a Cary-500i UV/vis/near-IR spectrophotometer. The reflectivity results are measured and compared, illustrated in Figure 5-8. The simulation results are done through scattering matrix method [35]. The spectrum shows that we can obtain more than 99% reflectivity from 600 nm to 1100 nm, much better than a conventional Al metal reflector with a reflectivity of about 90%.

5.2.2 Effect of backside ZnO layer thickness

In previous chapter, we implemented the self-assembled AAO and DBR structures within c-Si photoconductors and demonstrate the light trapping effects. As shown in Figure 4-2, the fabricated AAO structure has an average period of 380 nm. However, those structures are not fully optimized. In addition, the thin-film μc-Si cell we study here has a different configuration. Especially, the low index ZnO contact layer between the grating and active Si device may greatly influence the scattering effect. We investigate the calculated J_{sc} for the device structure shown in Figure 5-6 with different back ZnO thicknesses. We still assume the grating has a period of 380 nm and a thickness of 100 nm. The results are listed in Table 5.2. If there is no ZnO layer between the grating and Si, the J_{sc} can be improved by

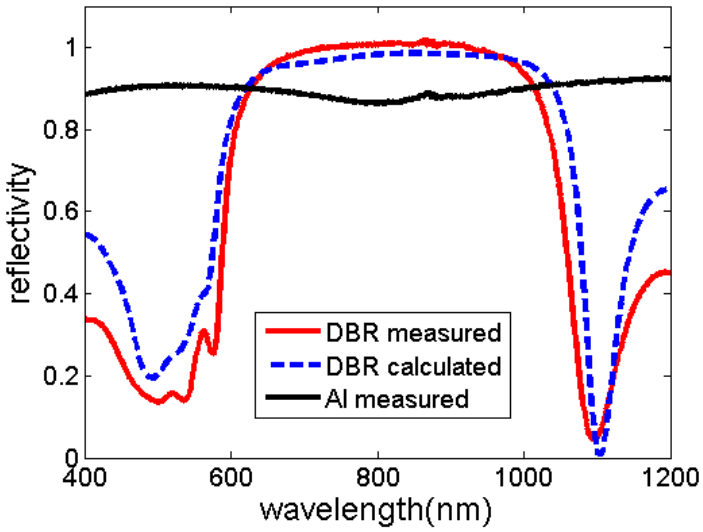

Figure 5-8: Comparison of the measured and calculated reflectivity spectra for DBR and the 200 nm Al film.

50% using the aforementioned grating and DBR, consistent with the results we obtain in Table 3.3. However, the absorption enhancement decreases as we increase the ZnO thickness. The device with grating, DBR and 400 nm thick ZnO shows a performance (19%) similar to the cell with DBR only (18%). This means the scattering effect introduced by the grating is greatly reduced when creasing the ZnO thickness. Therefore, the grating parameters should be redesigned and optimized to accommodate the fabricated device configuration.

Table 5.2: Calculated relative J_{sc} increase for μc-Si cells with fixed grating and DBR structures and different backside ZnO thicknesses.

cell type	relative J_{sc} increase
reference (without grating or DBR, 400 nm thick ZnO)	-
with DBR only, 400 nm thick ZnO	18%
with grating and DBR, no ZnO	50%
with grating and DBR, 50 nm thick ZnO	37%
with grating and DBR, 100 nm thick ZnO	29%
with grating and DBR, 400 nm thick ZnO	19%

5.2.3 Grating optimization

The structure of the grating layer is composed of a hexagonal a-Si array embedded in a SiO_2 matrix. As shown in Figure 5-6, the grating parameters are period (Λ), the Si rod diameter (D), and the grating thickness (t). Here we assume that the area ratio of a-Si and

SiO_2 is 1:1, which means that D is set to about 0.74Λ. The influence of Λ and t on the light trapping effect is plotted in Figure 5-9. If there is no grating layer ($t = 0$), only the DBR has an effect and absorption peaks induced by Fabry-Perot interferences are enhanced (Figure 5-10). The relative improvement of cell efficiency is about 19% as compared to the reference device structure without DBR and grating. When the grating period Λ is too small ($\Lambda < 400$ nm), absorption increase caused by the grating is not very significant. This differs from some previous numerical predictions and experiments, which indicate that strong enhancement occurs for a grating period Λ around 300 nm [21, 41]. The reason is due to the low-index ZnO contact layer between the active Si layer and the grating, which changes the diffraction condition and requires a larger grating period for effective scattering (the first order diffraction occurs when $\Lambda > \lambda/n$, n is the index for the layer close to the grating). The region for optimum response ranges from 600 nm to 700 nm for Λ, and corresponds to about 100 nm for t, where strong light diffraction appears and causes an optimal relative J_{sc} improvement of up to 34%.

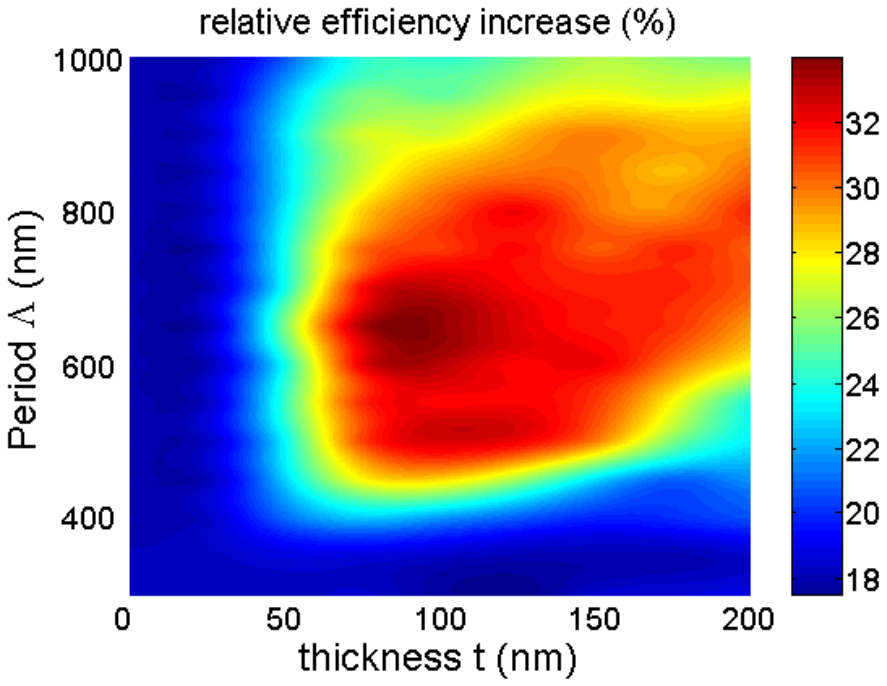

Figure 5-9: Schematic plot of the relative J_{sc} increase as a function of the grating period Λ and thickness t. The performance is compared to the reference cell structure without grating and DBR.

Figure 5-10 compares the simulated absorption spectra for reference cell, cell with DBR only, and cell with optimized grating (with $\Lambda = 700$ nm and $t = 120$ nm) and DBR. It can

be seen that all the devices exhibit identical response at short wavelengths ($\lambda < 500$ nm), since photons at this spectral range can be fully absorbed at a single pass and the absorption is only limited by the reflection at the front surface. At longer wavelengths ($\lambda > 500$ nm), we clearly observe the effects of grating and DBR. The enhanced absorption peaks for the device with DBR only are due to the Fabry-Perot interference effect. When the optimized grating layer is added, more interferences are introduced by various scattering mechanisms, further improving the overall absorption efficiency.

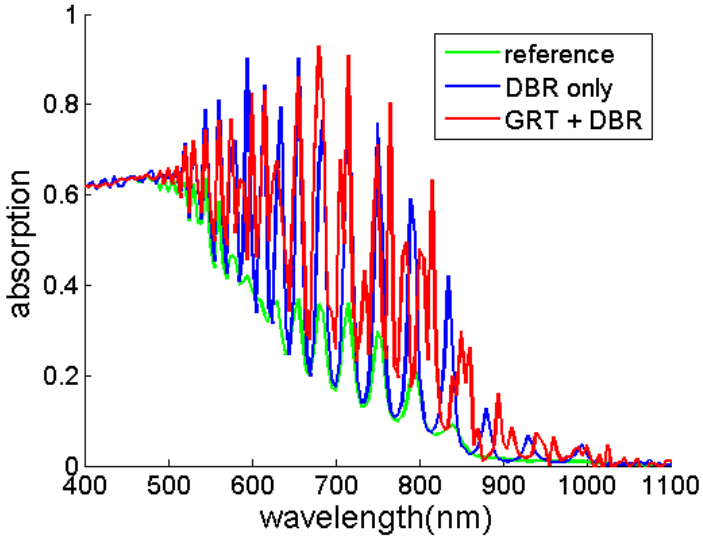

Figure 5-10: Simulated absorption spectra for cell structure with different configurations on the backside.

5.2.4 Rod diameter optimization

For simplicity, we simulate the effect of rod diameter with optimized Λ and t ($\Lambda = 700$ nm and $t = 120$ nm). We plot the J_{sc} enhancement as a function of the Si:SiO_2 area ratio in Figure 5-11. The maximum value is obtained when the fraction of SiO_2 is chosen to be 50%. When the SiO_2 fraction is approaching 0 or 1, the grating will lose its effect, and the enhancement of around 18% is totally from the DBR. This is also consistent with results in Ref. [35].

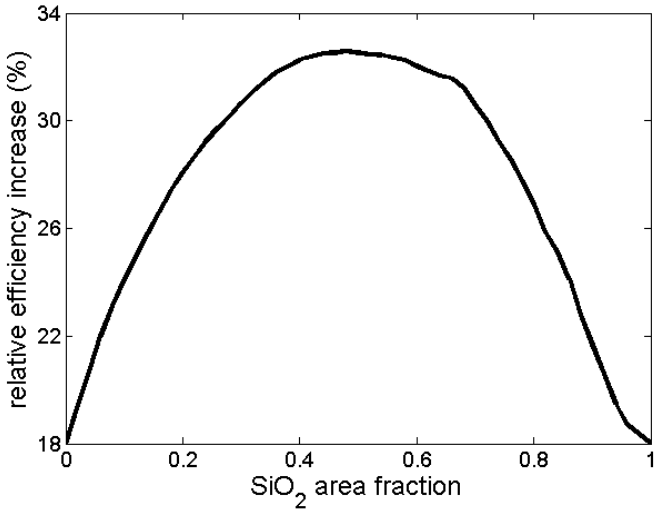

Figure 5-11: Relative J_{sc} improvement as a function of the Si:SiO_2 area ratio.

5.3 Fabrication and experimental results for thin-film μc-Si solar cells

5.3.1 PC structure fabrication

We use the self-assembled AAO technique to non-lithographically fabricate the submicron grating layer. The technique has been reported to pattern Al surfaces as substrates for solar cells [50], and in Chapter 4 we have demonstrated directly fabricating the AAO layer on crystalline Si wafers [41]. However, these methods are not compatible with our thin-film μc-Si cells, since the ZnO layers are severely damaged during the anodization process. Therefore, we choose an alternative method, which is using the AAO membrane as a template. The process flow is illustrated in Figure 5-12. The details for this method have been discussed in Chapter 3.

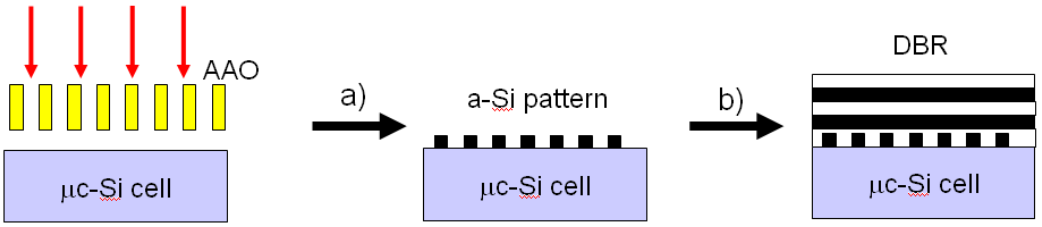

Figure 5-12: Illustration of the procedure for fabricating the light trapping structure. (a) forming the a-Si pattern by evaporative deposition through AAO membrane; (b) making DBR by PECVD.

By using two step anodization method at a constant DC voltage of 280 V in a citric acid solution, an AAO membrane structure is fabricated, with a period of about 700 nm, a thickness of about 2 μm and a porosity of nearly 50%. The SEM image of the AAO membrane is shown in Figure 5-13. We can more accurately calculate the period to be $\Lambda = 672$ nm through the 2D FFT image (Figure 5-14).

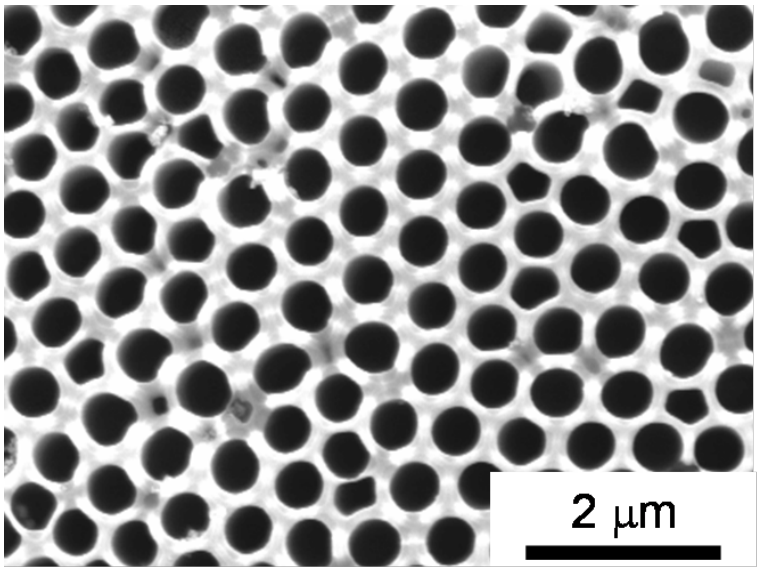

Figure 5-13: SEM image of the as-prepared AAO membrane used for deposition mask.

Through the AAO mask, 120 nm thick a-Si is deposited on the backside of the reference μc-Si cells using electron beam evaporation. During the deposition, the height of the a-Si pattern is simply dependent on the deposition time. The AFM image in Figure 5-15 reveals that the deposited a-Si pattern directly replicates the hexagonal AAO pore arrays. Before the subsequent DBR deposition, the a-Si pattern was covered by a thin SiO_2 layer, therefore working as a grating layer similar to that in our simulation model, with $\Lambda = 700$ nm and $t = 120$ nm.

It should be noted that the fabricated a-Si grating pattern exhibits a cone-shape structure with some irregularity. Simulation results in Table 5.3 compares the performance of different grating shapes, including the real grating pattern imported from the scanned AFM image (with a 3 μm by 3 μm range) in Figure 5-15 and the perfectly periodic cylindrical array (with $\Lambda = 700$ nm and $t = 120$ nm). The fabricated grating pattern shows a very similar performance (relative increase 29%) compared with the optimized, perfectly periodic hexagonal structure (32%). Despite of non-perfect periodicity, the effectiveness of the

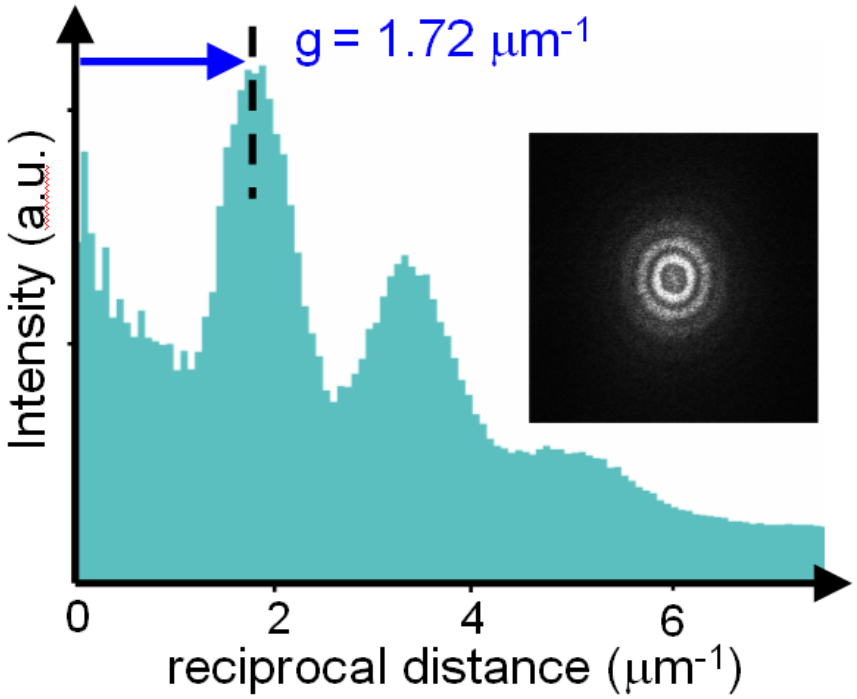

Figure 5-14: Rotational averaged radial intensity profile as a function of reciprocal distance from origin, based on the 2D FFT image of the SEM in Figure 5-13(shown in the inset).

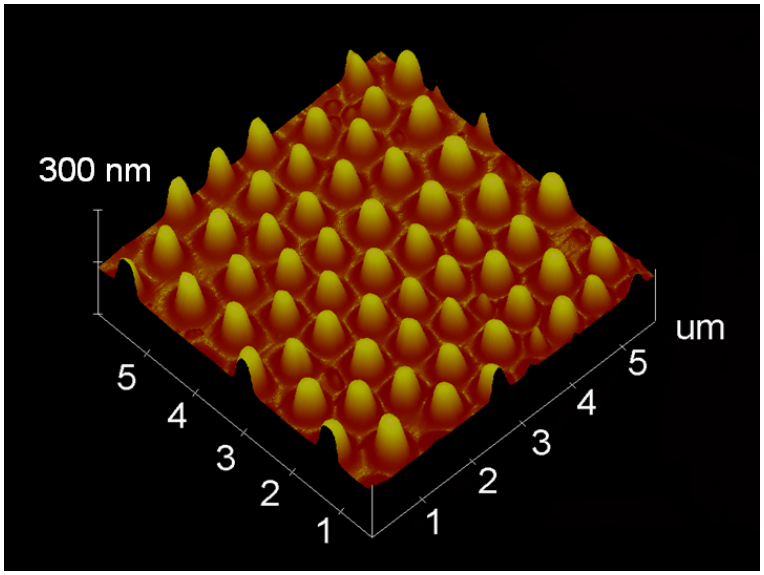

Figure 5-15: AFM image of the deposited a-Si pattern.

fabricated grating deposited through the AAO membrane, is achieved by implementing optimized design parameters and a medium range order that is longer than the wavelength in the optical media (λ/n).

Table 5.3: The perdicted efficiency improvement for different grating shapes, where the "perfect grating" is the periodic hexagonal array show in Figure 5-6 (with $\Lambda = 700$ nm and $t = 120$ nm), and the "fabricated grating" refers to the a-Si pattern imported from the AFM image in Figure 5-15.

	calculated $\Delta\eta/\eta_{ref}$ for perfect grating	calculated $\Delta\eta/\eta_{ref}$ for fabricated grating
PC	32%	29%

For comparison, we also fabricate other types of light trapping structures. We implement a similar technique to fabricate a-Si patterns with an average period of 380 nm using the AAO shown in Figure 3-9. In addition, planar DBR (by PECVD) or aluminum reflector (200 nm, by Ebeam evaporation) are also deposited on the backside of unpatterned μc-Si cells.

5.3.2 Device performance

The photovoltaic performances of μc-Si solar cells with different back structures are measured under AM1.5G spectrum. Figure 5-16 shows the current density-voltage (JV) curves, and the characteristic parameters derived from JV curves are summarized in Table 5.4. The relatively low absolute efficiency is due to imperfections in the μc-Si materials, which induce a high recombination rate. Nevertheless, it can be seen that the J_{sc} is considerably higher if grating and DBR are used as light trapping structures. This result is expected since the light trapping schemes increase the density of photogenerated carriers due to higher optical absorption. Furthermore, the V_{oc} and fill factor (FF) are not affected by the backside structure, in contrast to other light trapping configurations such as textured silicon interface, which causes degradation in V_{oc} and FF. The reason for this behavior is that our self-assembled 2D grating and DBR significantly enhances light trapping without increasing surface recombination or adversely affecting carrier transport as textured Si interfaces do.

In Table 5.5 we summarize the measured efficiency and relative efficiency increase for cells with different light trapping structures. Compared to the reference cell without any backside structure, planar aluminum reflector improves the cell efficiency by 7%, while the DBR can achieve an increase of 13%. This is consistent with the reflectivity difference

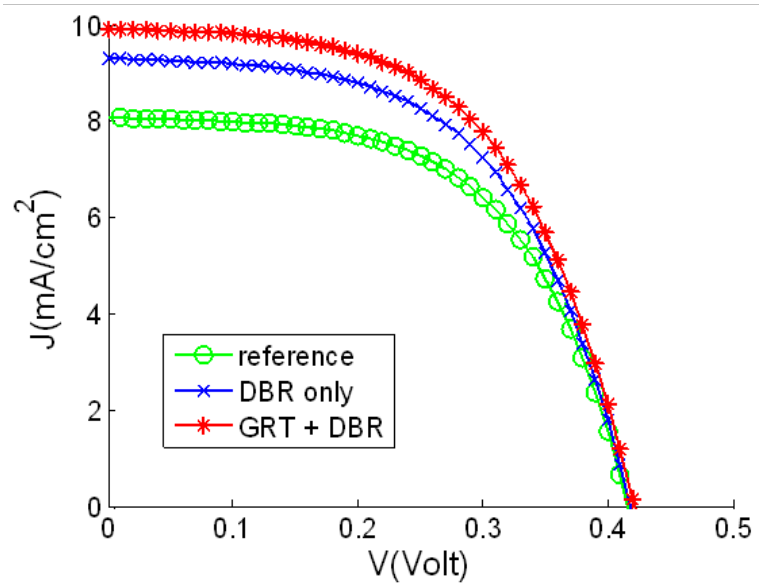

Figure 5-16: JV curves measured under AM1.5G spectrum for μc-Si devices with various back structures.

Table 5.4: Measured characteristics for μc-Si cells with different backside structures.

cell type	J_{sc}(mA/cm^2)	V_{oc}(V)	FF	efficiency η (%)
reference	8.09	0.416	0.57	1.93
DBR only	9.32	0.418	0.56	2.18
GRT + DBR	9.94	0.422	0.56	2.34

between Al and DBR shown in Figure 5-8. The PC structure containing a period-380 nm grating and DBR exhibits a very similar efficiency increase compared to the planar DBR, while the solar cell with optimal grating and DBR shows the highest performance with a relative improvement of 21%. These results show an agreement with the grating optimization graph Figure 5-9. The differences between simulated and measured data mainly come from the non-idealities such as electron-hole recombination as well as inherent interfacial roughness of the TCO layers.

Table 5.5: The measured efficiency and relative improvement compared to the reference cell.

cell type	efficiency	relative increase $\Delta\eta/\eta_{ref}$
reference	1.93%	-
planar Al reflector	2.07%	7%
DBR only	2.18%	13%
GRT (period 380 nm) + DBR	2.19%	13%
optimal GRT + DBR	2.34%	21%

To further confirm the results, external quantum efficiency (EQE) measurements are also taken. Using a monochromator, the photon responses are collected in the spectral range from 400 nm to 1100 nm, as illustrated in Figure 5-17. For short wavelengths (below 500 nm), the EQE curves remain identical for all solar cells, since μc-Si has an absorption length that is shorter than the device thickness (1500 nm). In agreement with our simulation, significant EQE enhancement can be seen from 600 nm to 900 nm. For the device with only DBR, a series of distinct peaks arise due to stronger interferences in the thin film layers. When the grating layer is added, light diffraction occurs and part of the reflected light propagates at oblique angles with much longer optical path length than the film thickness. Therefore, the spectrum becomes smoother and even higher EQE is achieved, especially from 700 nm to 800 nm. Overall, the EQE spectrum experimentally confirms our theoretical predictions. The measured spectra are smoother than the calculated spectra in Figure 5-10 and no distinct sharp peaks can be observed. This is mainly due to the resolution of the monochromator (around 10 nm) and the non-ideality and aperiodicity of the a-Si pattern.

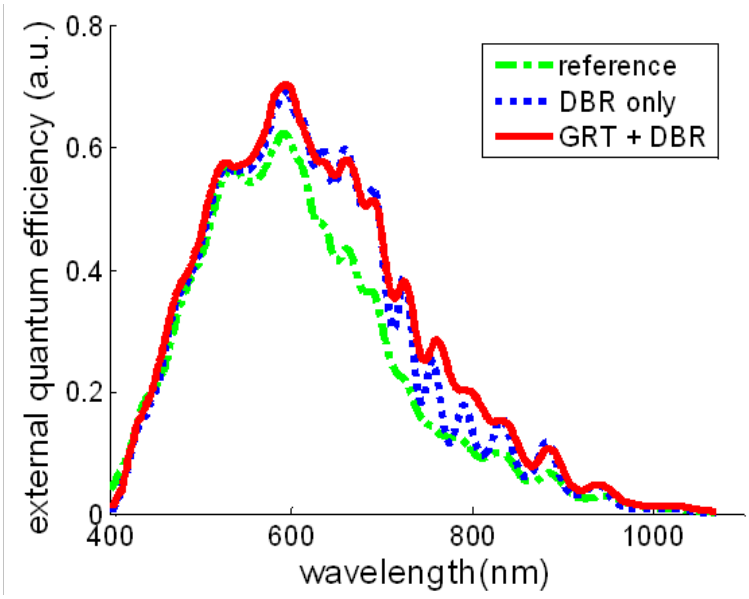

Figure 5-17: EQE spectra using monochromatic light from 400 nm to 1100 nm for μc-Si devices with various back structures. It can be observed that the cell with both grating and DBR shows the highest quantum efficiency in the red and near-IR range, thus obtaining the highest efficiency.

5.4 Summary

In this chapter, we first review the structures, fabrications and performances for different types of thin-film Si solar cells, including a-Si, μc-Si and micromorph Si cells. The PC structure for light trapping in thin-film μc-Si solar cells is optimally designed with numerical simulations and experimentally implemented through a non-lithographic, self-assembled technique that can potentially be scaled up to large area. Although there is plenty of room to improve the active material quality in the future investigation, the 1.5 μm prototype μc-Si devices integrating our proposed backside PC structure yield a 21% improvement in efficiency. This is further verified by quantum efficiency measurements, which clearly indicate stronger light absorption in the red and near-IR spectral ranges. Through appropriate design, this technique could also be implemented in other high-efficiency a-Si, micromorph Si and even single crystalline Si solar cells for efficiency enhancement. These results provide a low-cost and deterministic approach for achieving efficiency enhancement by light trapping in thin-film silicon solar cells.

Chapter 6

Fundamental performance limits for thin-film Si photovoltaics

In previous chapters, we have demonstrated that the efficiency of thin film μc-Si solar cells can be greatly improved by using our proposed self-assembled template approaches. We can make more efforts to further boost the cell performances, for example, by optimizing the deposition conditions, improving the TCO layers and passivating the surfaces and interfaces. Current thin-film Si single junction solar cells with the best performances, however, still show inferior performance compared to Si wafer based techniques and thus become less competitive [18]. In this chapter, we explore the fundamental efficiency limits for a single junction thin film Si solar cell (for example, with an active layer thickness of 1.5 μm). First, we discuss the fundamental Lambertian limits for light trapping in thin film Si, and develop an optimization based method to optimize periodic textures for thin film Si cells.[1] We then predict the optimal efficiency for a thin film Si cell based on Shockley-Queisser theory. We conclude that it is still possible to design a thin film Si solar cell approaching 20% efficiency.

[1]This work has been published in "Optimization-based design of surface textures for thin-film Si solar cells," Optics Express, **19**, A841-A850 (2011) [51]. Copyright Optical Society of America. Reproduced with permission.

6.1 Optimization-based design of surface textures for light trapping

For thin film Si photovoltaics, one of the major challenges is to absorb light at near-IR wavelengths where the absorption length is much larger than the active layer thickness. Besides our works, various light trapping schemes have been proposed and experimentally demonstrated as promising solutions for efficiency enhancement. Figure 6-1 shows some examples of light trapping design. Front and/or back surface textures (whether periodic or aperiodic) can improve efficiency by scattering normally incident light into the plane of the film, but are limited by the fact that the same texture also scatters in-plane light back out of the film. In order to understand these limits, different authors have considered textured-surface absorption under models with restricted assumptions for which an explicit limit can be derived (detailed derivation can be found in Appendix A). The most well-known models are pioneered by Yablonovitch [23], in which the efficiency enhancement is at most $4n^2$ in 3D strutures for a film with index n. The result is known as the Lambertian limit, Yablonovitch's limit, $4n^2$ limit, ergodic limit and/or statistical limit. It is a thermodynamic limit based on the conclusion that the number of photonic density of states is increased by a factor of n^2 when light propagates from air to a dielectric material. For 2D structures, the enhancement factor $4n^2$ is reduced to πn. However, the Lambertian limits (πn and $4n^2$) are based on the assumption that the incoming light is isotropically distributed. We know that the incident sunlight is not isotropically distributed through out the daytime, and usually it peaks in the middle of the day (for normal incidence). It has been shown that restricting the incident angles to lie within a cone with the half-angle θ results in a theoretical enhancement limit of $4n^2/\sin^2\theta$ (for 3D) or $\pi n/\sin\theta$ (for 2D) [52], which can be used for a concentration system. However, here we consider only infinite thin-film geometries without light-concentrating systems, so these results may no longer apply. Although Lambertian limits are still valid for isotropic incidence, we still do not know how to obtain an angular/enhancement tradeoff, how to design a surface texture to achieve the best performance, and what is the maximum enhancement for normal incidence.

More recently, a more generalized Lambertian model has been developed and extended to finite film thickness and finite spectral range for periodic structures at normal incidence by Yu and others [9]. In their theory, the authors modeled the film by a set of guided-

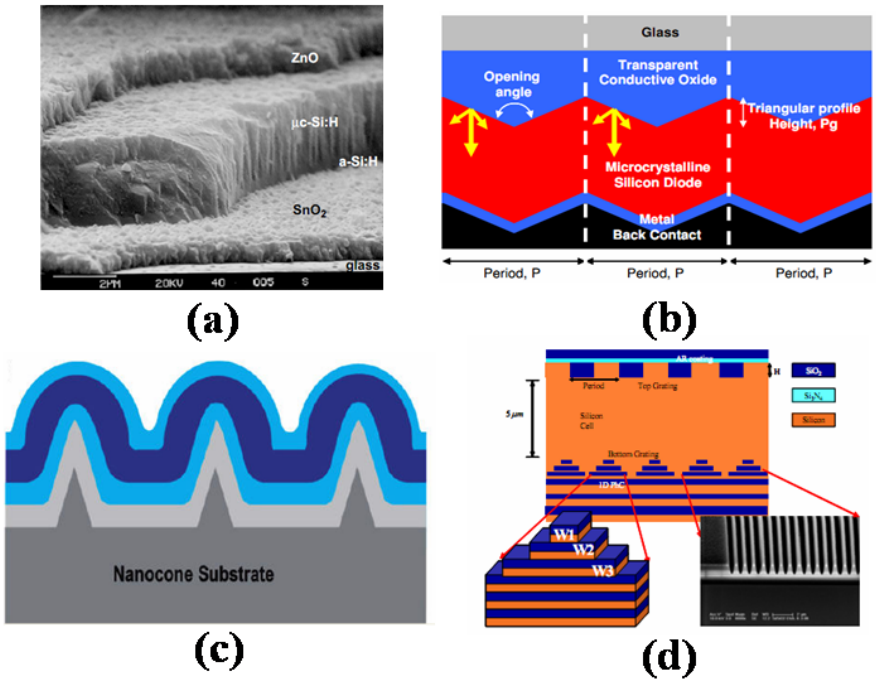

Figure 6-1: Examples of light trapping design for thin film Si solar cells. (a) Traditional textures based on rough TCO surface [3]; (b) Triangular periodic grating structure [6]; (c) "Nano-dome" solar cells based on pre-patterned substrates [7]; (d) Multi-layered grating structures [8].

wave resonances, assuming isotropic scattering by requiring equal scattering into all allowed resonances and weak scattering by modeling the resonances as exponentially decaying leaky modes. However, the performances of these models may not be fundamental limitations, and it is possible that larger efficiency enhancement can be achieved by violating the weak and isotropic scattering assumptions of the models. We perform full electromagnetic wave simulations to investigate the influence of different light trapping structures in thin film silicon cell. Furthermore, an optimization algorithm is implemented in our numerical model to explore the light trapping limit for periodic structures.

6.1.1 Computational Method

The 2D device structure used in our numerical model is illustrated in Figure 6-2. From top to bottom, it consists of air (semi-infinite), 1.5 μm crystalline silicon (Si), 0.5 μm silicon dioxide (SiO_2) and a perfect reflector on the backside. For the sake of simplicity, electrical components like metal grids or transparent conductive oxides (TCOs) are not included in the optical model. Meanwhile, the silicon is considered to be intrinsic and the effects of p

and n regions are neglected. The front surface of silicon and the interface between SiO_2 and reflector are kept flat, and only the interface between Si and SiO_2 are textured. It should be noted that the volumes of Si and SiO_2 are kept constant when different type of textures are evaluated. That means, if the texture is characterized by a function $H(x)$, we enforce that the average H_{avg} is held constant at 0.5 μm.

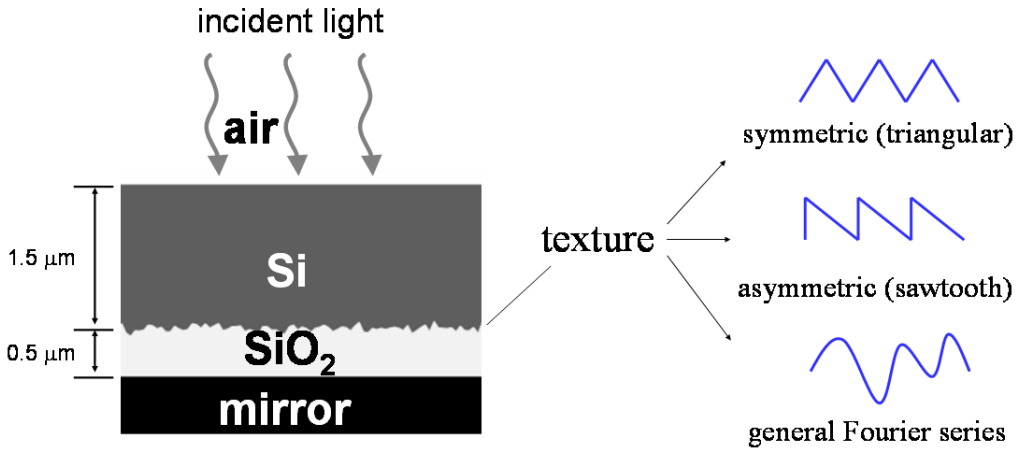

Figure 6-2: (left) Schematic device structure for a thin film Si solar cell with a textured Si / SiO_2 interface. The averaged thicknesses for Si and SiO_2 layers are 1.5 μm and 0.5 μm, respectively. (right) Different types of texture we investigate are symmetric triangular grating, asymmetric sawtooth grating and general periodic structures with Fourier series.

To simulate this structure, we employ the FDTD method [31] implemented via the open source code MEEP [32]. The simulation cell size is Λ in the x direction, with a periodic boundary condition for normal incident light and a grid resolution of 10 nm. The material refractive indices are 3.6 for Si and 1.4 for SiO_2. The Si layer is assumed to be weakly absorptive, with a constant absorption coefficient ($\alpha = 12.56\ \mathrm{cm}^{-1}$). We use a constant absorption coefficient because it can be easily implemented in MEEP as a constant conductivity. This is different from the real material dispersion [29], but the underlying physics should not be affected as long as we are exploring the light trapping in the weak absorption regime. The unit cell is illuminated under normal incidence by TE polarized light (with the electric field perpendicular to the plane) in the spectral range from 900 nm to 1100 nm. The absorption spectrum $A(\lambda)$ is calculated by Fourier-transforming the response to a short pulse to obtain $A = 1 -$ reflection, with a wavelength resolution of 1 nm. The performance of the texture is characterized by the dimensionless enhancement factor F,

which is the averaged absorption divided by the single-pass absorption αd:

$$F = \frac{\frac{1}{\lambda_2 - \lambda_1} \int_{\lambda_1}^{\lambda_2} A(\lambda) d\lambda}{\alpha d} \tag{6.1}$$

Different light-trapping structures are simulated and compared in terms of their performance F.

6.1.2 Simulation Results

Light trapping by Asahi glass

The first type of structure we investigate is from commercially available Asahi U-type glass [53], which is a glass plate coated by fluorine doped tin oxide (SnO_2:F). It is widely used as a superstrate for amorphous and microcrystalline silicon solar cells. The intentionally textured SnO_2:F works as a conductive layer as well as a scattering layer for light trapping. An atomic force microscope (AFM) image of the Asahi glass is shown in Figure 6-3. The root-mean-square (RMS) roughness is measured to be about 30 nm. To construct a 2D model for comparison, 1D textures were extracted from the measured AFM image and imported into the model mentioned in Figure 6-2. To obtain more accurate results, 20 different 1D textures (with a length of 4 μm) were arbitrarily selected and simulated, and we computed enhancement factors F from $0.90\pi n$ to $1.28\pi n$ (average $(1.04 \pm 0.10)\pi n$), which are very close to the prediction of a conventional 2D Lambertian surface ($F = \pi n$).

Light trapping by symmetric triangular gratings

Diffractive gratings have been proposed as promising candidates to improve solar cell efficiency by us and others. Here we implement a symmetric triangular grating into our model (Figure 6-4(a)), and investigate its influences on light trapping. Absorption-enhancement factors F are calculated based on the simulated absorption spectra (from 900 nm to 1100 nm), and plotted as a function of the grating period Λ and thickness t. As shown in Figure 6-4(b), the optimal regions are around $\Lambda = 900$ nm, although there also are other parameters shown to have high absorption. Figure 6-4(c) shows the absorption spectrum of the optimal structure indicated in Figure 6-4(b) ($\Lambda = 920$ nm and $t = 520$ nm). The calculated maximum F is $1.26\pi n$. The simulation results are compared with the generalized Lambertian model [9] in Figure 6-4(d). The blue curve plots the best F at each period Λ, compared

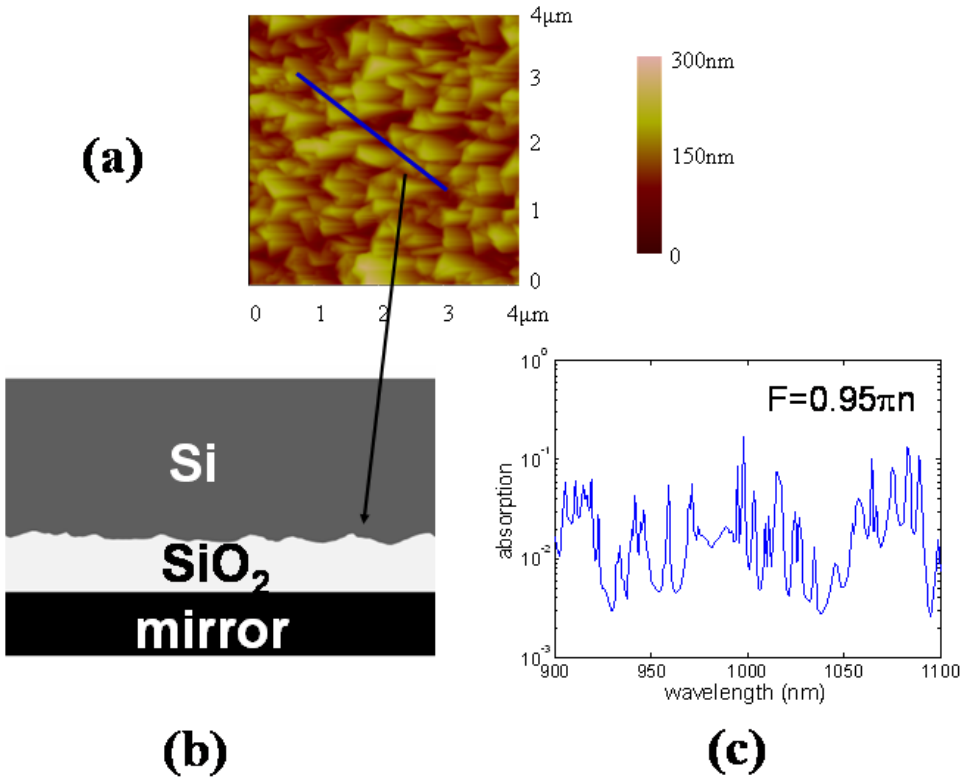

Figure 6-3: (a) AFM image of an Asahi U-type glass substrate; (b) An example of simulated device structures with 1D texture extracted from the AFM image; (c) The simulated absorption spectrum, with a calculated $F = 0.95\pi n$.

with the generalized model for symmetric grating structures (in green):

$$F(\Lambda) = \frac{1}{\lambda_2 - \lambda_1} \int_{\lambda_1}^{\lambda_2} \left(\frac{\frac{\Lambda}{\lambda}}{\lfloor \frac{\Lambda}{\lambda} \rfloor + 1} \right) d\lambda \cdot \pi n \tag{6.2}$$

where $\lfloor x \rfloor$ rounds to the nearest integers less than or equal to x. It can be observed that the two curves follow a similar trend, both peaking at around $\Lambda = 900$ nm. However, the simulated results F deviate from the generalized Lambertian model, showing higher values for most periods ($1.26\pi n$ compared to $0.9\pi n$ at $\Lambda = 900$ nm).

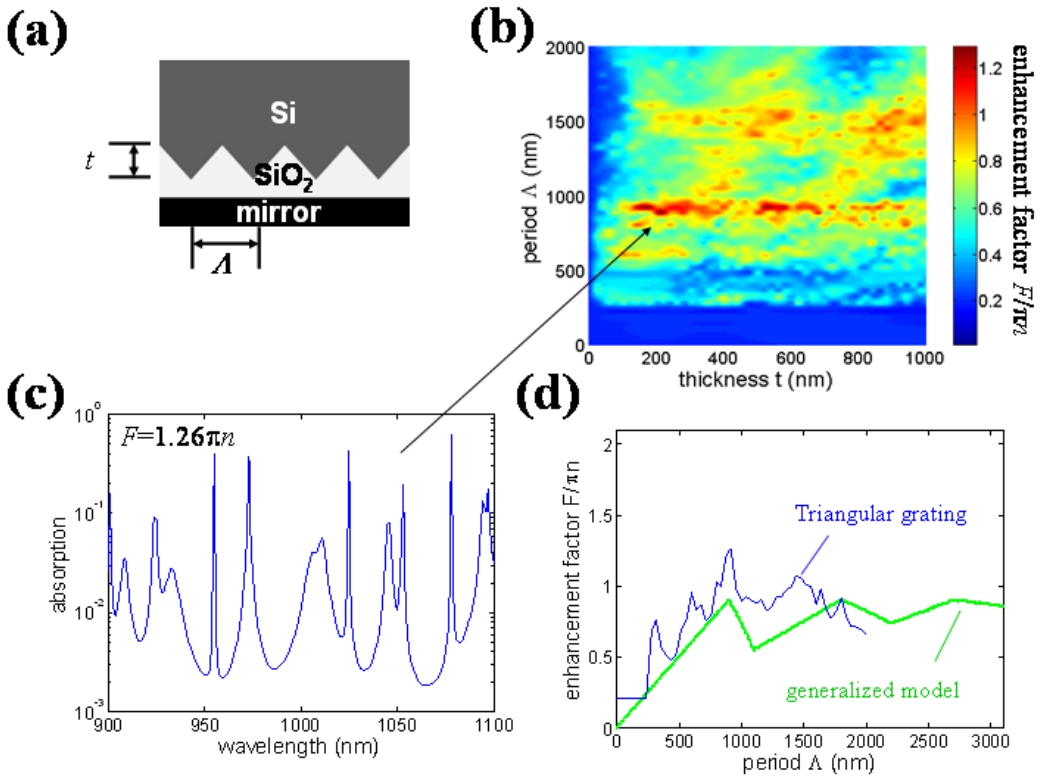

Figure 6-4: (a) Schematic device structure with symmetric triangular grating; (b) Plot of the absorption enhancement factor (F) as a function of the grating period Λ and thickness t. The arrow indicates the optimal parameters; (c) Absorption spectrum of the optimal structure ($\Lambda = 920$ nm and $t = 520$ nm), obtaining $F = 1.26\pi n$; (d) Comparison of the best results at each Λ and the generalized model for symmetric gratings.

Light trapping by asymmetric sawtooth gratings

We now investigate the performance of an asymmetric sawtooth grating Figure 6-5(a), following the inspiration that asymmetry should enhance performance for normal incidence

[9, 54]. Similar to the previous section, the enhancement factor F is plotted as a function of Λ and t in Figure 6-5(b). Optimal regions are still around $\Lambda = 900$ nm; however, F is significantly higher than that obtained for symmetric grating, with a maximum value of $2.04\pi n$. The optimal structure has $\Lambda = 920$ nm and $t = 240$ nm. As illustrated in Figure 6-5(c), the absorption spectrum for the optimized sawtooth grating has many more resonance peaks than the optimized symmetric grating (Figure 6-4(c)), which causes a larger enhancement. This is because in structures with mirror symmetry (Figure 6-4(a)), normally incident plane wave can only couple to even modes while resonances with odd modes remain unexcited [9,54]. We can also compare the results with the generalized model for asymmetric grating structures:

$$F(\Lambda) = \frac{1}{\lambda_2 - \lambda_1} \int_{\lambda_1}^{\lambda_2} \left(\frac{\frac{\Lambda}{\lambda}}{\lfloor \frac{\Lambda}{\lambda} \rfloor + \frac{1}{2}} \right) d\lambda \cdot \pi n \tag{6.3}$$

Again, the two curves have a similar trend, and the peak result for sawtooth gratings exceeds the value $1.8\pi n$ predicted by Yu's model for asymmetric gratings.

Light trapping by grating with optimized Fourier series

We have simulated and optimized two types of gratings (symmetric and asymmetric), comparing with the analytical models. However, there are various shapes of gratings, and probably the simple triangular and sawtooth gratings do not have the highest performances. To further explore the light trapping limit of a periodic structure, an arbitrarily shaped texture should be studied. In principle, any arbitrarily shaped periodic texture, described by the function $H(x)$ (in nanometers), can be expanded in terms of its Fourier series:

$$H(x) = 500 + \sum_{n=1}^{\infty} \left(A_n \sin\left(\frac{2\pi n}{\Lambda} x\right) + B_n \cos\left(\frac{2\pi n}{\Lambda} x\right) \right) \tag{6.4}$$

where 500 nm is the averaged thickness of SiO_2 layer (the volume of SiO_2 is fixed), and Λ is the period of the simulation cell. To ensure that the texture does not cross the SiO_2/mirror interface, we use a constraint $|H(x) - 500| < 500$. Because the absorption can be numerically calculated for any given device texture $H(x)$, the enhancement factor F is directly related to the Fourier coefficients (A_1, B_1, A_2, B_2, ...) and period Λ:

$$F = F(A_1, B_1, A_2, B_2, \ldots, \Lambda) \tag{6.5}$$

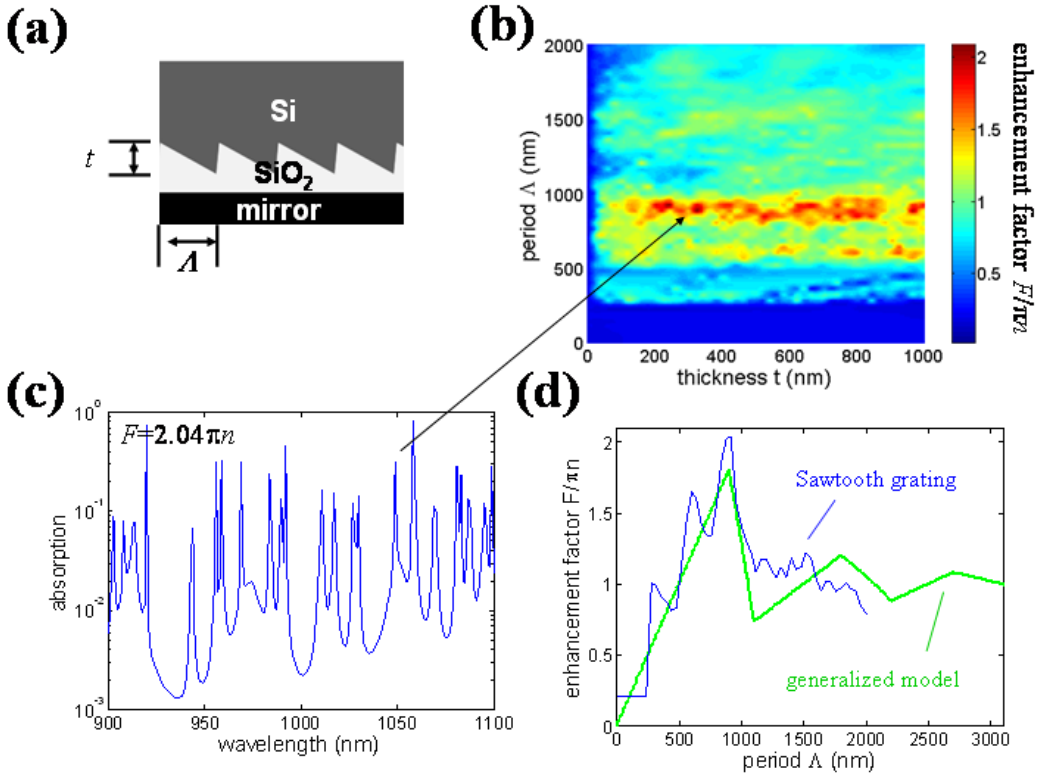

Figure 6-5: (a) Schematic device structure with asymmetric sawtooth grating; (b) Plot of the absorption enhancement factor (F) as a function of the grating period Λ and thickness t. The arrow indicates the optimal parameters; (c) Absorption spectrum of the optimal structure ($\Lambda = 920$ nm and $t = 240$ nm), obtaining $F = 2.04\pi n$; (d) Comparison of the best results at each Λ and the generalized model for asymmetric gratings.

Therefore, we can optimize the device performance F by tuning the parameters (A_1, B_1, A_2, B_2, ... and Λ). As a practical matter, the number of parameters is limited by the simulation capability. We choose the first 5 orders as degrees of freedom, i.e. from (A_1, B_1) to (A_5, B_5), and set higher-order Fourier coefficients to zero. One of those parameters is redundant for periodic boundary condition, because it corresponds to a phase shift. Therefore, we can set $B_5 = 0$ without loss of generality. Based on previous optimization results for triangular and sawtooth gratings as well as the predictions of Yu's model [9], we expect that the optimal structure has a period of around 900 nm, so we choose the initial Λ to be 900 nm, but Λ is permitted to be varied in the optimization. The FDTD method is combined with a nonlinear optimization toolbox NLopt.[2] The algorithm we use is based on constrained optimization by linear approximation (COBYLA) [55]. Generally, this problem may have many local optima, and it is infeasible to guarantee that the global optimum has been obtained, so these local optima only represent a lower bound on the attainable performance. We also explored the use of a genetic global-optimization algorithm [56], but its convergence rate was so slow that over feasible run times it obtained inferior results than repeated local optimization. We run the optimization several times with different initial parameter values to explore different local optima. The optimization results are illustrated in Figure 6-6 and Table 6.1. In 3 runs, we achieve optimized enhancement factors F of $2.07\pi n$, $2.10\pi n$ and $2.28\pi n$, respectively. These local optima are noticeably larger than the prediction of the Yu's model [9]. In addition, the optimizations keep Λ close to its initial value of 900 nm.

Table 6.1: Optimized structural parameters and the corresponding enhancement factors F. The units for A_n, B_n (n from 1 to 5) and Λ are nm.

	A_1	B_1	A_2	B_2	A_3	B_3	A_4	B_4	A_5	B_5	Λ	$F/\pi n$
run 1	124	-8.63	56.2	108	-12.8	-33.2	-24.2	-4.91	-18.1	0	866	2.07
run 2	81.7	160	1.25	183	-3.91	167	-10.9	-14.6	-1.65	0	898	2.10
run 3	170	157	15.9	53.7	18.7	20.2	17.3	19.2	18.3	0	899	2.28

The above method explores light trapping performances for asymmetric structures, since it includes both sine and cosine coefficients. By using only cosine coefficients, we can also optimize symmetric structures. Here we intentionally set all the sine coefficients (A_1 to A_5) to zeros. The optimization results are illustrated in Figure 6-7 and Table 6.2. We obtain

[2]The Nlopt package can be downloaded from `http://ab-initio.mit.edu/nlopt`.

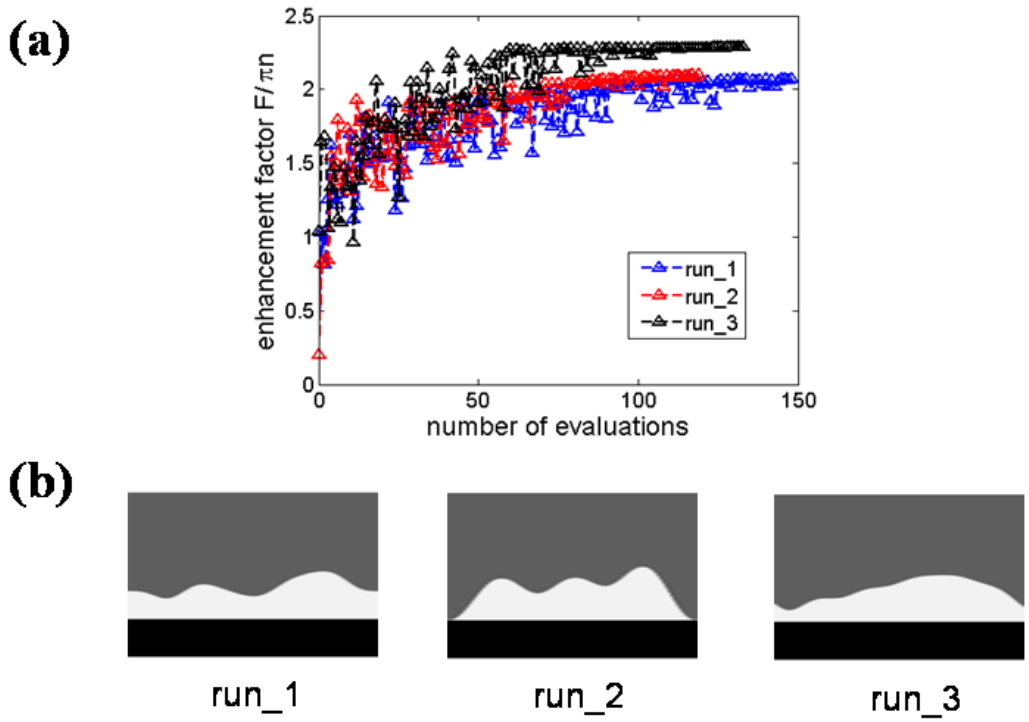

Figure 6-6: (a) Convergence trends for enhancement factor F optimization using NLopt-COBYLA, starting with different sets of initial parameters; (b) Optimized device structures for 3 different runs. All the optimized structures have periods Λ around 900 nm.

optimized F of $1.56\pi n$ and $1.45\pi n$, respectively. The performances of optimized symmetric structures are much lower than those achieved for asymmetric structures, but still larger than the prediction of the Yu's model [9] and are also larger than the performance of the optimized triangular grating.

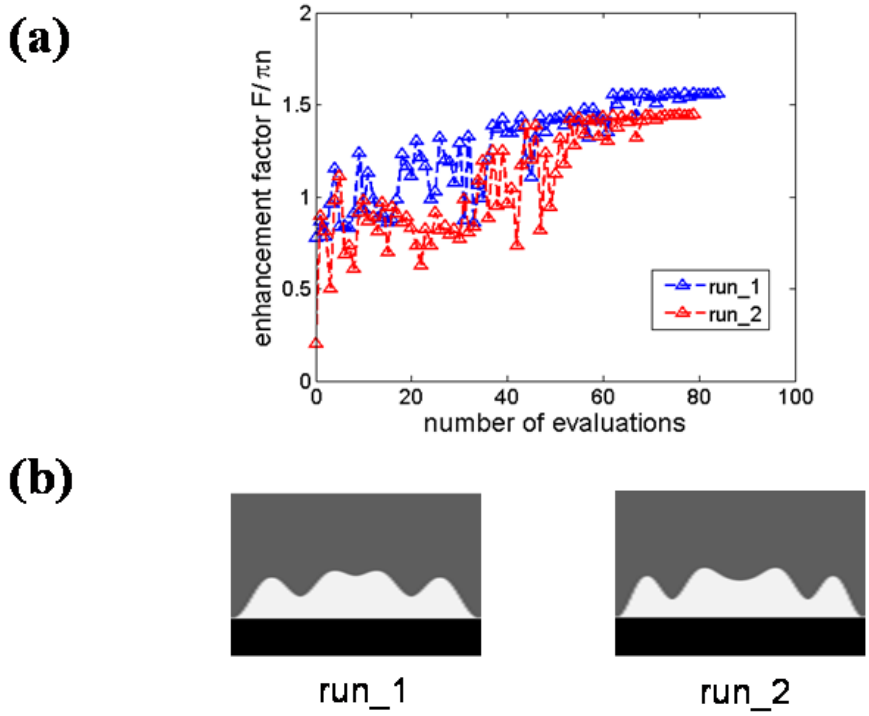

Figure 6-7: (a) Convergence trends for enhancement factor F optimization for symmetric structures, starting with different sets of initial parameters; (b) Optimized device structures for 2 different runs, and both the optimized structures have periods Λ around 900 nm.

Table 6.2: Optimized structural parameters and the corresponding enhancement factors F for symmetric structures. The units for B_n (n from 1 to 5) and Λ are nm.

	B_1	B_2	B_3	B_4	B_5	Λ	$F/\pi n$
run 1	203	16.6	154	143	-22.4	899	1.56
run 2	181	23.6	5.65	191	95.9	899	1.45

In our model, textured Si/SiO_2 interface is the critical component introducing strong anisotropic scattering, while the magnitude of the surface roughness is determined by the thickness of the silicon oxide layer. Therefore, to further explore the light trapping limit,

we introduce the oxide thickness t_{ox} as an additional parameter for optimization:

$$F = F(A_1, B_1, A_2, B_2, \ldots, \Lambda, t_{ox}) \tag{6.6}$$

The optimization results are illustrated in Figure 6-8 and Table 6.3. With this additional parameter, for asymmetric structures we achieve optimized enhancements F of $2.28\pi n$, $2.70\pi n$ and $2.38\pi n$, which are even higher than the obtained results when t_{ox} was fixed at500 nm in the previous simulations. The best found F is $2.70\pi n$, which is 50% larger than the prediction of the Yu's model ($F = 1.8\pi n$). Of course, it is possible that other local optima exist with even better performances.

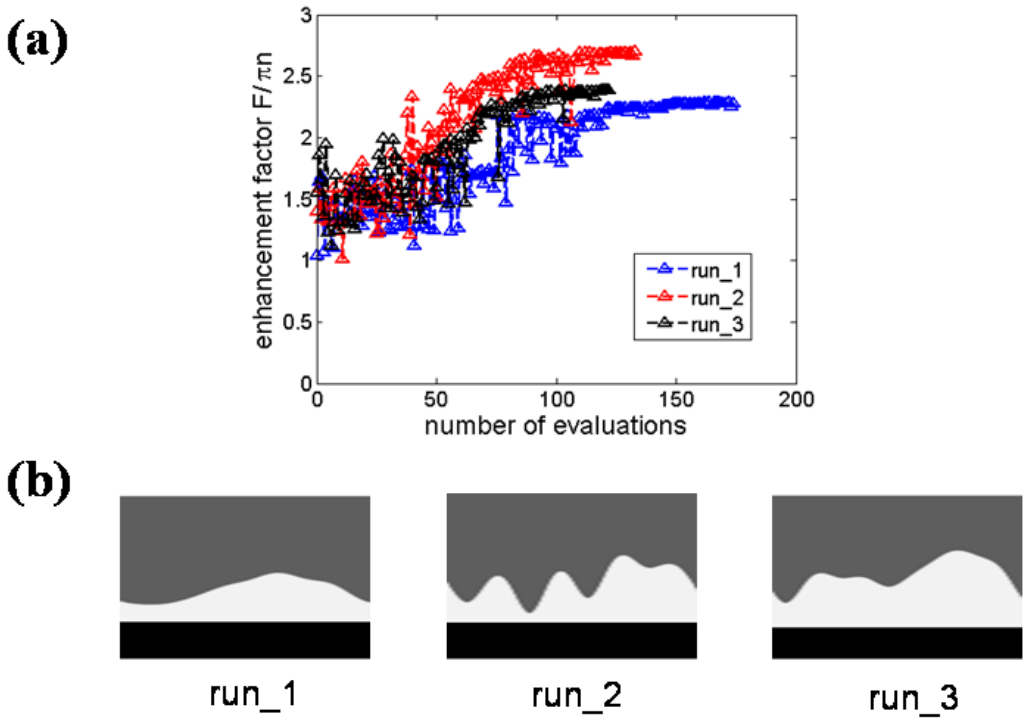

Figure 6-8: (a) Convergence trends for enhancement factor F optimization using NLopt-COBYLA, starting with different sets of initial parameters. t_{ox} is also included as a variable; (b) Optimized device structures for 3 different runs, and all the optimized structures have periods Λ around 900 nm.

Table 6.3: Optimized structural parameters and the corresponding enhancement factors F. t_{ox} is also included as a variable. The units for A_n, B_n (n from 1 to 5) and Λ are nm.

	A_1	B_1	A_2	B_2	A_3	B_3	A_4	B_4	A_5	B_5	Λ	$F/\pi n$
run 1	184	161	8.63	16.4	6.89	2.88	-0.96	18.1	-7.74	0	897	2.28
run 2	256	-44.1	36.1	82.2	-22.1	93.1	218	-44.4	-43.7	0	882	2.70
run 3	250	53.2	49.3	249	48.3	48.4	51.0	49.4	49.9	0	900	2.38

Comparison and discussion

Our simulation results are summarized compared with the generalized Lambertian models by Yu et al. [9], as shown in Figure 6-9. In the generalized models (in green), the maximum F occurs when $\Lambda = 900$ nm, in which $F = 1.8\pi n$ for asymmetric structures. For symmetric structures, $F = 0.90\pi n$ for the first maximum, but approaches πn as Λ goes to infinity. Textures from commercial Asahi glass (the dotted line in black) show performance close to πn.

The best results of our simulated triangular and sawtooth gratings are also shown (in blue). As illustrated, both triangular grating and sawtooth grating follow a trend similar to the analytical models, peaking at around $\Lambda = 900$ nm. However, these simulated results F deviate from the Lambertian models, showing higher values for most periods.

In addition, we illustrate the results for gratings with optimized Fourier series (in black and red dots). Due to the computational expense of this optimization, we only plot local optima for several runs with different initial values at $\Lambda \approx 900$ nm. Nevertheless, all of them exceed the optimal sawtooth gratings as well as the Lambertian models. The best Fourier structures are also illustrated in the insets, with $F = 2.70\pi n$ for asymmetric structures and $F = 1.56\pi n$ for symmetric structures. These results clearly demonstrate that violating the isotropic coupling assumption in Yu's model [9] can lead to higher performances.

Angular response of the optimized structure

As explained in Appendix A, this super-Lambertian enhancement for normal incident light must necessarily come at the expense of enhancement at other angles. To demonstrate this, in Figure 6-10 we plot the enhancement factor versus incident angle, as computed by a rigorous coupled wave analysis (RCWA) method [35]. As expected, the enhancement factor F decreases significantly for non-normal incidence [9]. F is larger than πn for incident angles from about -25 degree to 25 degree. The average enhancement factor over all angles:

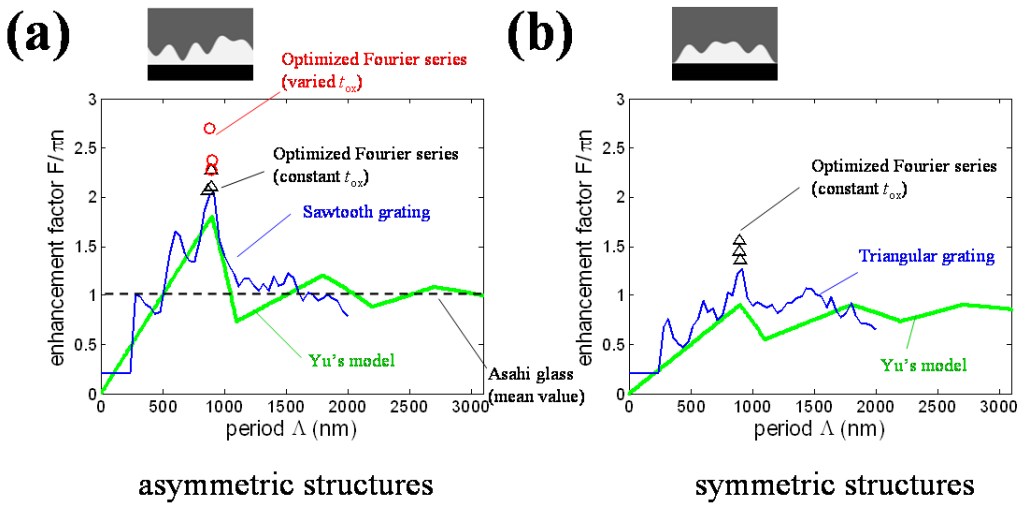

Figure 6-9: Summary of the calculated maximum enhancement factors F in our simulations and comparison with Yu's model in [9] and commercial Asahi glass. The insets indicate the structures with the best performance achieved in our optimizations. (a) Asymmetric structures; (b) Symmetric structures.

$$\overline{F}_{2D} = \frac{\int_{-\frac{\pi}{2}}^{\frac{\pi}{2}} d\theta F(\theta) \cos\theta \sin\theta}{\int_{-\frac{\pi}{2}}^{\frac{\pi}{2}} d\theta \cos\theta \sin\theta} \tag{6.7}$$

is calculated to be $0.9\pi n$, which still obeys the classical Lambertian limit for isotropic light [23]. It should be noted that low-cost thin-film Si solar cells are usually implemented within a non-concentrated configuration like a roof-top system, so strictly restricting the angle range is not practical. Nevertheless, our design provides a methodology for achieving high efficiency solar cells with restricted angles. In addition, our design is still instructive for practical applications since the incoming power of sunlight is not isotropic and usually peaks in the middle of the day. Therefore, it is still meaningful to design a cell with a better performance for normal incidence.

6.1.3 Discussion

Lambertian models provide a simple and instructive intellectual framework for describing the effects of surface texturing on thin-film absorption. Even outside their range of validity (isotropic weak scattering), they can still be surprisingly descriptive: in our case, we find that the Lambertian prediction by Yu's model [9] gives a rough guideline as to the optimal texture period, and is within 50% of the actual performance. In order to design an optimal

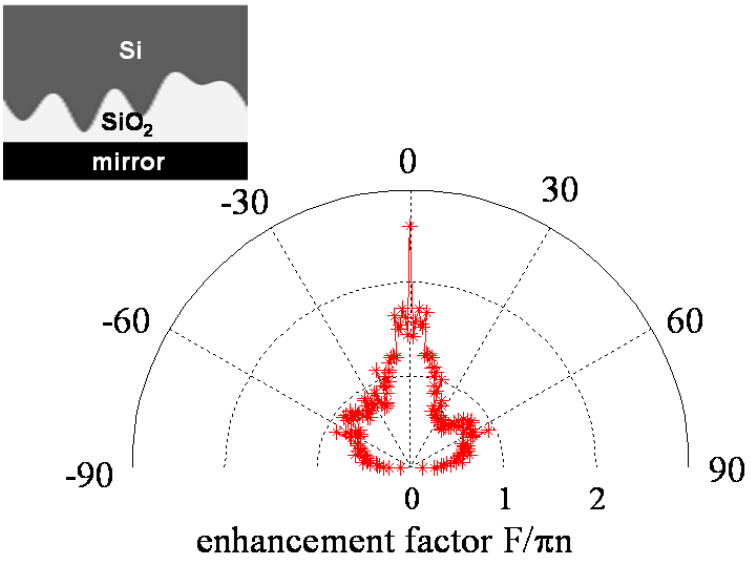

Figure 6-10: Angular dependence of the optimized asymmetric structures obtained in Figure 6-9.

texture structure at normal incidence or in restricted angles, including strong anisotropic scattering, one must eventually depart from the confinements of analytical models, however beautiful, and resort to brute-force computation and parameter optimization. The results in this section provide a glimpse of what is possible from such a computational approach, in which significant improvements are obtained even by a small number of local optimizations (despite the nonlinear and nonconvex nature of this optimization problem). Such local optima represent only lower bounds on the attainable performance, and by expending additional effort one could certainly envision pushing those bounds upwards, although locating the true global optimum with confidence seems daunting. It may also be possible to analytically prove more general upper bounds on performance for gratings with a given period and specific incident angle. As a practical matter, a more important goal is to adapt these techniques to 3D. In order to improve the efficiency of the calculation and make 3D optimization feasible, a number of techniques could be employed. First, one could use more sophisticated computational techniques than FDTD, such as boundary-element methods that only require the interfaces to be discretized [57]. Second, one could use adjoint methods to compute the gradient of F with respect to the optimization parameters [58], and thereby employ much more efficient gradient-based optimization methods (such methods have been used in topology optimization of photonic structures with hundreds or thousands of degrees of freedom [59]). As a heuristic method, it might be interesting to investigate

using the optimized Fourier coefficients from the 2D simulations in this paper to form a two-dimensional texture with similar frequency components in 3D.

6.2 Efficiency limit based on the Shockley-Queisser theory

Until now, most parts of this thesis are focused on the light trapping issues, that is, designing a solar cell structure so that it can absorb as much light as possible. More absorbed light means higher generated photon currents, thus larger short-circuit current density (J_{sc}). Ultimately, we do not only want to know the J_{sc}, but also the power conversion efficiency of the solar cell. In this section, we make some predictions about the fundamental efficiency limit of a single junction thin film Si solar cell, based on the Shockley-Queisser theory.

6.2.1 Shockley-Queisser limit

The maximum theoretical efficiency of a p-n junction solar cell was first predicted by Shockley and Queisser [24]. Based on their theory, the current generated by a solar cell is balanced by the absorbed photon current and radiative recombination [60]:

$$\begin{aligned} J &= J_{photon} - J_{recombine} \\ &= e\int_0^{\lambda_g} s(\lambda)A(\lambda)d\lambda - \frac{2\pi e(n^2+1)E_g^2 kT}{h^3c^2}\exp\left(\frac{-E_g}{kT}\right)\left(\exp\left(\frac{eV}{kT}\right)-1\right) \end{aligned} \tag{6.8}$$

where e is the unit charge for an electron, λ_g is the cutoff wavelength for absorption (corresponds to the material bandgap E_g), $s(\lambda)$ is the standard AM1.5G solar spectrum [33], $A(\lambda)$ is the absorption spectrum of the solar cell (depending on the material absorption coefficient and device light trapping design), h is the Planck's constant, c is speed of light in vacuum, n is refractive index, E_g is the bandgap of the semiconductor, k is the Boltzmann constant and T is the environment temperature. Here we assume $n = 3.6$ as a constant.[3] At room temperature ($T = 300$ K), Equation 6.8 predicts the current-voltage (JV) relationship. Therefore, the ideal efficiency of the solar cell is the maximum output power divided by the incident solar energy.

$$\eta = \frac{J_{max}V_{max}}{\int_0^\infty s(\lambda)d\lambda} \tag{6.9}$$

[3]For semiconductors, n may vary from 2.0 (diamond) to 4.0 (HgTe), but this does not affect the final results too much.

For ideal case, we assume an infinitely thick device that can absorb all the photons with energy above the bandgap, then $A(\lambda) = 100\%$. Therefore, efficiency η is a function of bandgap E_g, which is plotted in Figure 6-11. Under AM1.5G spectrum, the maximum efficiency for a single junction solar cell is about 31% with a bandgap of 1.4 eV. If bandgap gets small, the overall efficiency will decrease since the energy each photon can generate is limited by the bandgap (or open-circuit voltage V_{oc}), although the material can absorb more photons thus have higher current J. If bandgap gets larger, the overall efficiency will also decrease since less photons can be absorbed (less J_{sc}). Several important semiconductors (Si, Ge, GaAs and aSi) are indicated in the figure. It is observed that both Si and GaAs are ideal materials to make a solar cell with an optimal efficiency above 30%.

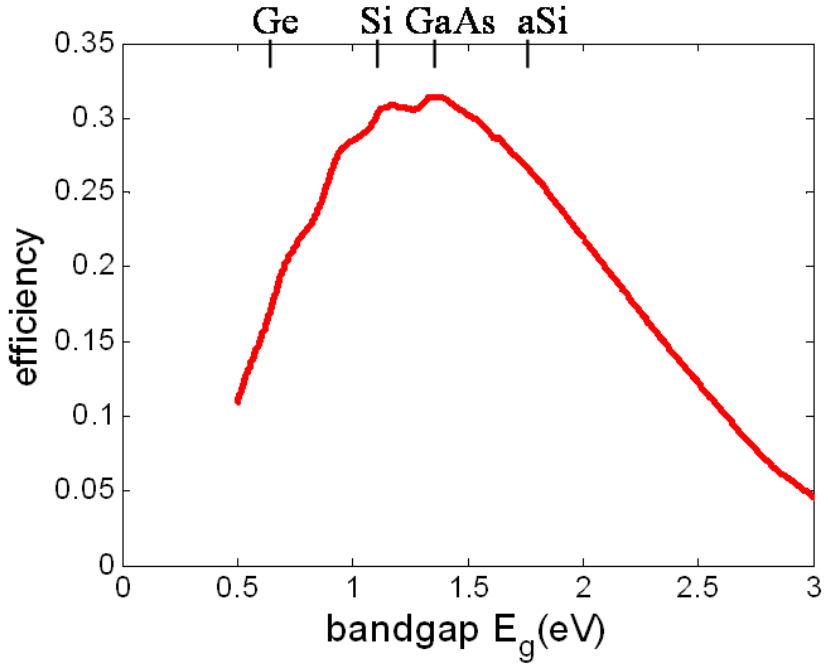

Figure 6-11: Shockley-Queisser efficiency limit for semiconductors with different bandgaps under AM1.5G spectrum.

6.2.2 Efficiency limit considering nonradiative recombination

In Equation 6.8, only radiative recombination is assumed. For a real device, nonradiative recombinations also occur. We can introduce a factor called external radiation efficiency η_{ext}, which is the ratio of radiative recombination to the total recombination, then Equation 6.8 can be modified as [61]:

$$
\begin{aligned}
J &= J_{photon} - J_{recombine} \\
&= e\int_0^{\lambda_g} s(\lambda)A(\lambda)d\lambda - \frac{1}{\eta_{ext}} \cdot \frac{2\pi e(n^2+1)E_g^2 kT}{h^3c^2} \exp\left(\frac{-E_g}{kT}\right)\left(\exp\left(\frac{eV}{kT}\right)-1\right)
\end{aligned} \tag{6.10}
$$

Therefore, the introduced factor $\frac{1}{\eta_{ext}} > 1$ (in red) plays an important role, which further increases the recombination current and decreases the V_{oc}. The value of η_{ext} depends on the type of semiconductors and device structure design.[4] Direct bandgap semiconductors like GaAs can have very high η_{ext} (approaching 100%) [62], while indirect bandgap semiconductors like Si and Ge typically have low η_{ext} (around 1% even for the best devices) [63]. Here we assume $\eta_{ext} = 1\%$ and replot Figure 6-11 in Figure 6-12. The introduction of η_{ext} significantly changes the efficiency limits. Especially for low bandgap semiconductors ($E_g < 1.5$ eV), there is a 5% absolute efficiency drop when η_{ext} decreases from 100% to 1%. This means that the performances of low bandgap semiconductors are more sensitive to the material and device qualities. In this modified model, we can get the maximum efficiency for Si is about 25%, which was almost achieved by Martin Green's group at UNSW in 1999 [10]. Due to the limitation of η_{ext}, the record for crystalline Si cells is very difficult to beat. For GaAs cells, there is still a chance to reach the Shockley-Queisser limit above 30% because η_{ext} can approach 100%, and the-state-of-the-art efficiency is 28.2% [18].

6.2.3 Efficiency limit for thin-film Si solar cells

When real thin-film solar cells are considered, the light absorption $A(\lambda)$ in Equation 6.8 and Equation 6.10 will also be a limiting factor for cell efficiency. For thin-film Si, this issue is severe because of its nature of indirect bandgap. As we discussed previously, absorption in the weak absorption regime is determined by the fundamental light trapping limits. If isotropical incident light is considered, Lambertian limits are applicable. However, the $4n^2$ absorption enhancement factor (in 3D devices) is only valid for very weak absorption ($\alpha d \approx 0$). For intermediate and high absorption regime ($\alpha d > 0$), the Lambertian limit can be approximated to [64]

[4] Essentially, it is similar to the quantum efficiency of light emitting diodes, which is the combination of internal quantum efficiency η_{int} and extraction efficiency $\eta_{extract}$. See Chapter 7 for detailed discussion.

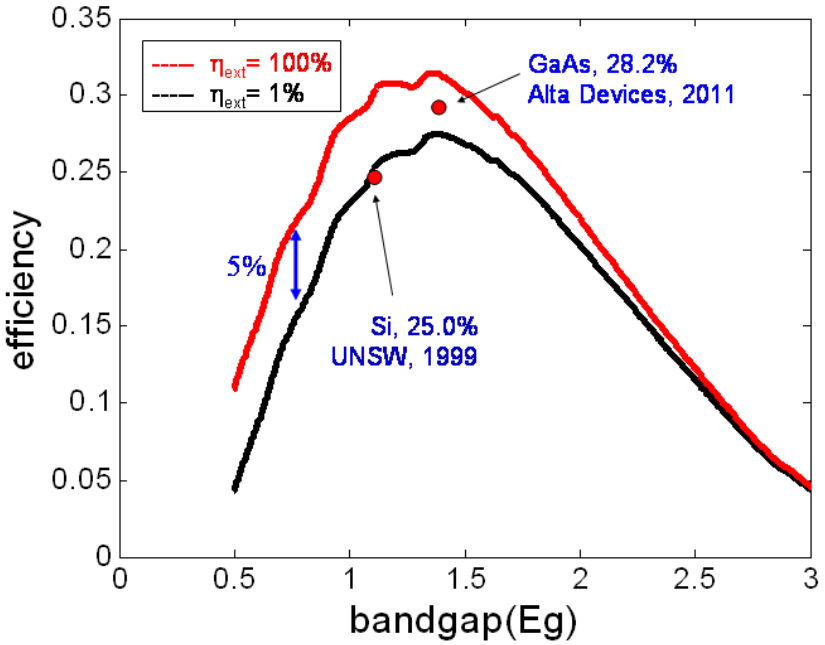

Figure 6-12: Efficiency limit for semiconductors with different bandgaps under AM1.5G spectrum. The red curve is the same as in Figure 6-11, with $\eta_{ext} = 100\%$, while the black curve plots the case when $\eta_{ext} = 1\%$. The world record efficiencies to date for Si and GaAs are indicated.

$$A = \frac{1 - e^{-4\alpha d}}{1 - (1 - \frac{1}{n^2})e^{-4\alpha d}} \tag{6.11}$$

while the single pass absorption (without considering the interference effect) is

$$A = 1 - e^{-\alpha d} \tag{6.12}$$

Based on Equation 6.11 and Equation 6.12, Figure 6-13 compares the absorption spectra for different types of crystalline Si cells. These absorption spectra $A(\lambda)$ can be input into Equation 6.10 (assuming $\eta_{ext} = 1\%$) to calculate current-voltage relationships, which are plotted in Figure 6-14. The cell performances, including short-circuit current J_{sc}, open-circuit voltage V_{oc} and cell efficiency, are extracted from the JV curves and listed in Table 6.4. We can see that cell performances, especially J_{sc}, critically depend on cell thickness and light trapping design. On the other hand, V_{oc} are not so much different for different types of cells, since V_{oc} are mostly determined by recombinations.

The above discussions are based on the assumption that the Lambertian light trapping

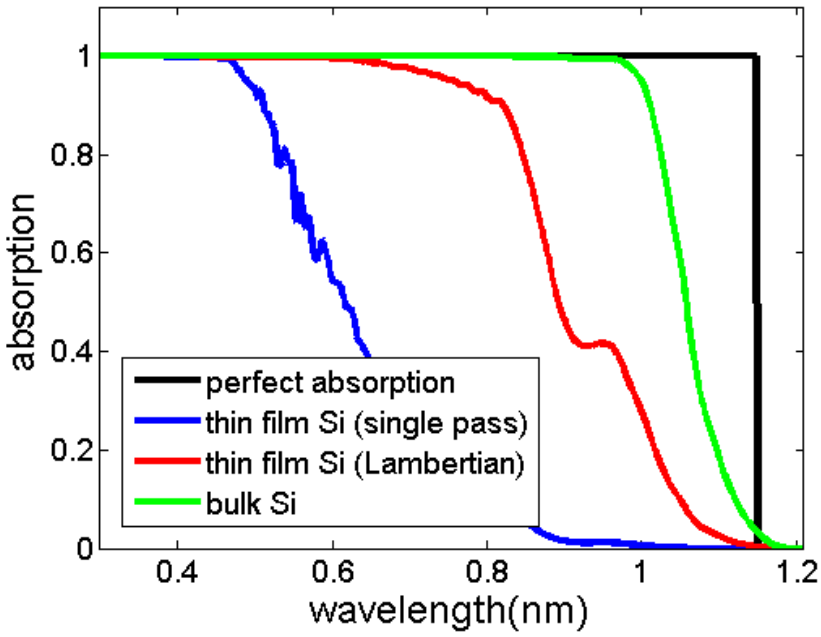

Figure 6-13: Comparison of the ideal absorption spectra for different crystalline Si solar cells: perfect absorption (100% above the bandgap), planar 1.5 μm thin-film Si (single pass), 1.5 μm thin-film Si with Lambertian light trapping and bulk Si with a thickness of 600 μm.

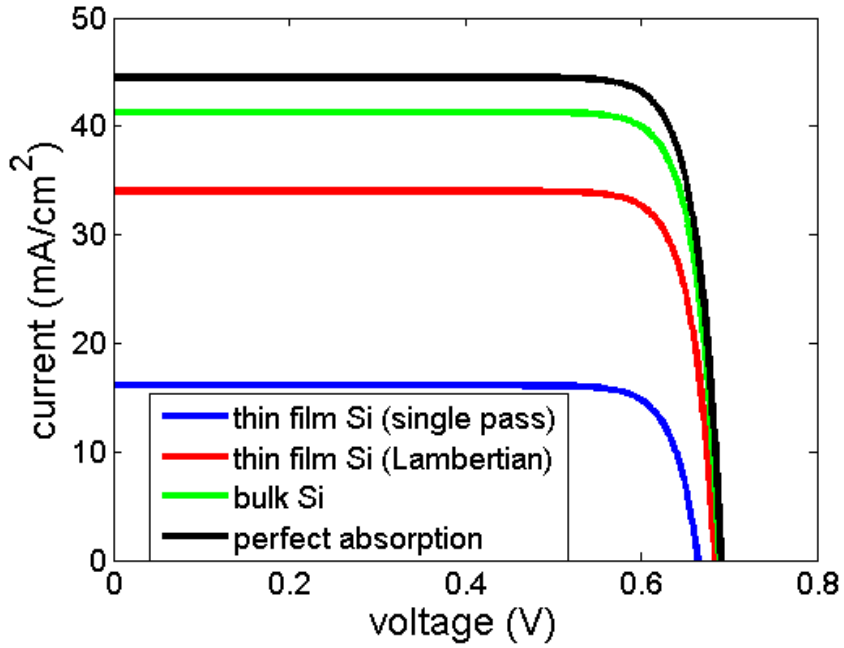

Figure 6-14: Comparison of the ideal current-voltage curves for different crystalline Si solar cells: perfect absorption (100% above the bandgap), planar 1.5 μm thin-film Si (single pass), 1.5 μm thin film Si with Lambertian light trapping and bulk Si with a thickness of 600 μm.

Table 6.4: Calculate cell performances for solar cells in Figure 6-13.

cell types	J_{sc}(mA/cm^2)	$V_{oc}(V)$	Efficiency
thin-film Si (single pass)	16.1	0.664	8.98%
thin-film Si (Lambertian)	34.0	0.684	19.6%
bulk Si (single pass)	41.3	0.689	24.0%
perfect absorption	44.5	0.691	26.0%

provides the upper limit ($4n^2$) for light absorption in thin-film Si cells. As we previously demonstrated for a 2D model, the classical limits can be exceeded in restricted spectral and angular ranges. Therefore, efficiency can be further improved for thin-film Si cells with advanced light trapping design, and more than 20% can be obtained for 1.5 μm thin-film Si cells.

6.3 Conclusions and Outlook

In this chapter, we discuss the possibilities for achieving crystalline Si solar cells with high efficiency. Two important factors should be considered:

1. Ideal light trapping design to approach Lambertian limit, enhancing light absorption and photon current J_{sc};

2. Ideal material and device qualities to approach Shockley-Queisser limit (Equation 6.10), achieving high voltage V_{oc}.

For bulk crystalline Si cells, we predict that the cell efficiency limit under AM1.5G spectrum should be around 26% (Table 6.4). Practically, the best Si cell to date has an efficiency of 24.7% [10], which almost approaches this limit. The device structure of this cell is shown in Figure 6-15. It has ideal light trapping designs, including double layer antireflection coating, inverted pyramids front texture and rear metal reflector. In addition, high quality float zone (FZ) wafers and carefully designed n-type and p-type regions enable good carrier collections and surface passivations.

For thin-film Si cells, approaching the theoretical limit is a much more daunting task. Although in Table 6.4 we predict that a 1.5 μm thick Si cell with Lambertian light trapping can reach an efficiency of almost 20%, the best thin-film Si cells (either polycrystalline or amorphous) only obtain efficiency around 10% [18]. The reasons leading to the gap between the ideality and reality are manifold:

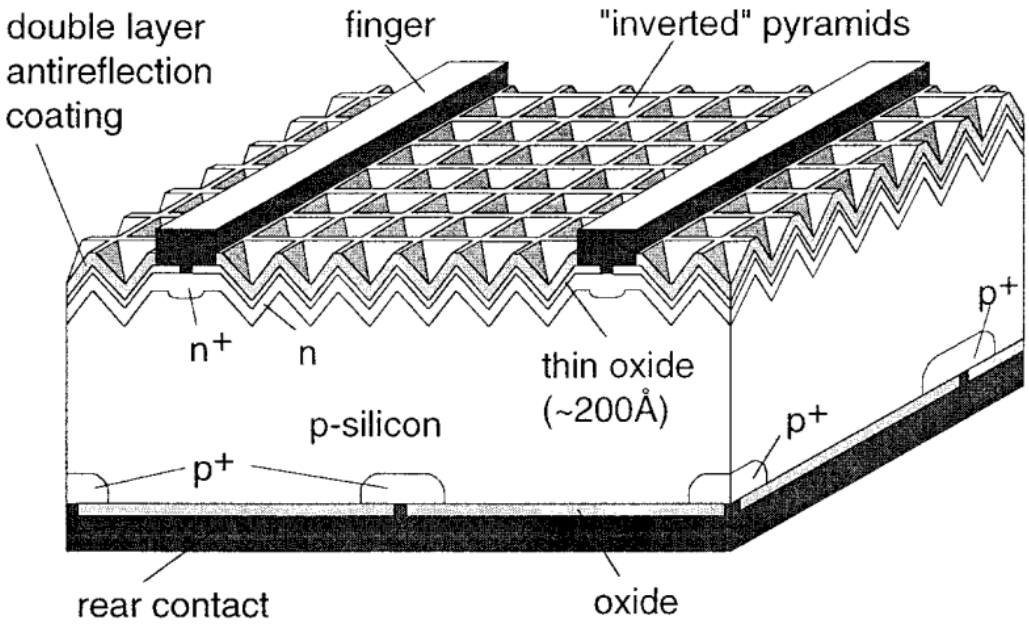

Figure 6-15: PERL (Passivated Emitter, Rear Locally-diffused) solar cell structure with world-record efficiency [10].

1. For thick Si, deeply etched textures (with a depth of tens of micrometers) can be used to obtain ideal Lambertian light trapping. However, for thin film Si the light trapping schemes should be carefully designed to exhibit expected performances since the textures are strongly limited by the cell thickness;

2. Since the textures have dimensions comparable to the cell thickness, they can significantly affect carrier collections and device performances;

3. Most of the thin film Si cells are fabricated through physical deposition like evaporation or chemical vapor deposition (CVD). Therefore, polycrystalline or amorphous Si films are formed, which have poorer material qualities compared to single crystalline Si wafers. This will induce severe recombinations and affect the carrier collections;

4. The techniques used in Figure 6-15, such as surface passivation and local diffusion, are very difficult to be implemented in thin film Si devices, since the whole pn junction has a limited thickness.

Therefore, in order to obtain a thin film Si cell with an efficiency up to 20%, the above challenges should be addressed. In addition, there is a tradeoff between cell performances

and fabrication cost if large-scale manufacturing is considered in the future. Here we propose several feasible techniques for a high efficiency single junction thin film Si solar cell:

1. In order to obtain thin-film Si with high quality, we can begin with single crystalline Si wafers, then use layer transfer techniques to peel off thin film Si cells from the wafers [65]. The Si wafers can be reused and the entire process can be repeated;

2. To enable efficient carrier collection, core-shell configurations and/or nano/micro wire structures can be used to replace the conventional vertical pn junction [66];

3. The numerical simulation and optimization methodology we have used in this chapter can be adapted to design the optimal periodic or nonperiodic light trapping schemes to achieve ideal absorption [51];

4. The self-assembled techniques mentioned in the previous chapters can be utilized to fabricate the designed light trapping textures at a low cost [44].

Chapter 7

High-index-contrast self-assembled texture for light extraction enhancement in LEDs

Light management issues not only challenge photovoltaic device design, but also various optoelectronic applications, including biotechnology [67], photodetection [68] and information technology [69]. In this appendix, we further adapt the self-assembled AAO technology we have developed to improve the light extraction efficiency in light-emitting diodes (LEDs).[1]

7.1 Introduction

Light-emitting diodes (LEDs) have become an emerging and promising candidate for light sources. Unlike conventional incandescent or fluorescent light sources, LEDs directly transfer electricity into light. Therefore, it has many advantages such as high energy conversion efficiency, long lifetime and small footprint [71]. Typical LED devices are made of inorganic (III-V) or organic semiconductor junctions. The internal quantum efficiency η_i of the light emission process, which is the portion of electron-hole pairs converted into photons, can be increased by improving material quality, and the state-of-the-art η_i has reached 90% for III-V semiconductors, already approaching the theoretical limit [62]. As a consequence, cur-

[1]This work has been published in "Design and fabrication of high-index-contrast self-assembled texture for light extraction enhancement in LEDs," Optics Express, **19**, A701-A709 (2011) [70]. Copyright Optical Society of America. Reproduced with permission.

rently the major LED efficiency limiting factor becomes poor light extraction, i.e. photons trapped inside the device due to total internal reflection at semiconductor and air interface. For a planar LED, the light extraction efficiency η_e can be estimated to be $\frac{1}{4n^2}$ [72]. For most semiconductors, their refractive indices n are high ($n > 2$). Therefore, η_e is a severe limitation for overall device performance.

To resolve the issue of limited extraction efficiency η_e in semiconductor LEDs, many photonic designs have been proposed. For example, organic materials are used as encapsulants to cover the top surface and reduce the total internal reflection [73]. Another example is to roughen/texture the device surface and induce stronger scattering effect [74]. However, these methods have limitations. Organic encapsulants suffer from degradation under photon radiation (especially for blue and green light), which largely limits their use for long lifetime and high brightness LEDs. Texturing semiconductor surface (by plasma etching, for example) generates defects that work as recombination centers that exacerbate non-radiative recombination and decrease the internal quantum efficiency η_i [75]. Furthermore, random scattering surfaces generated using a conventional texturing process lack the ability to purposively optimize and control the structural parameters of the textured surface.

Photonic crystal (PhC) has a structure with one, two, or three dimensional (1D, 2D and 3D) periodic patterns consisting of two materials with different refractive indices. In such periodic structures, light propagation can be controlled in various ways [76]. To increase LED extraction efficiency, a two-dimensional photonic crystal structure can be embedded in the device [77] or integrated on top surface [78]. Due to the periodicity, the guided waves can leak to free space as Bloch modes. Therefore, light can escape from the high index semiconductors even if the incident angle is larger than the critical angle. However, to fabricate these photonic crystals with submicron feature size, high-cost methods like interference lithography or electron beam lithography have to be employed, which prohibits LED cost reduction and high-volume production. Therefore, a low-cost and controllable method is highly desirable for fabrication of light extraction photonic crystal structures in LED devices.

Here we proposed a self-assembled two-dimensional photonic structure to increase the light extraction efficiency in LEDs. The proposed structure has several advantages:

1. A potentially low-cost, self-assembled method is introduced for fabrication, and the structural parameters can be controlled by experimental conditions;

2. Unlike plasma or wet chemical etching, the method is non-specific and can be implemented on top of any semiconductors;

3. Instead of etching through the active device, the structure is directly deposited on the surface, so it is non-damaging and does not cause any degradation of internal quantum efficiency η_i;

4. According to the targeted emission wavelength, various materials can be deposited to make the structure for achieving optimal light extraction;

5. As we will discuss below, a high-index-contrast texture is used, which provides much more efficient light extraction than low-index-contrast structures like SiO_2 / air or Al_2O_3 / air gratings.

7.2 Device design and optimization

The LED device with designed light extraction configuration is plotted in Figure 7-1. The light extraction texture is made by a hexagonal pattern as a grating layer. Due to the diffraction effect of the grating, light propagating at oblique angles (outside the emission cone) can be partly coupled out from the high index III-V semiconductor layer. Therefore, the light extraction efficiency will be significantly improved. Since the light out-coupling critically depends on the light extraction structure, the grating should be carefully designed to maximize the efficiency at the device emission wavelength.

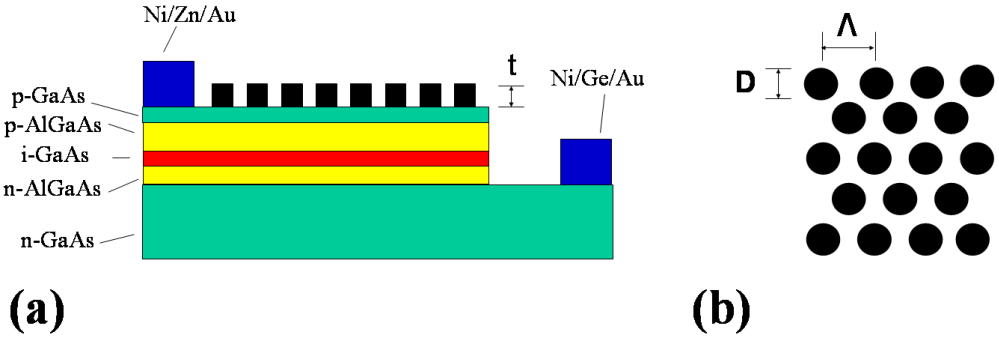

Figure 7-1: (a) Schematic layout of a test LED device with photonic crystal structures integrated on top surface for light extraction. The active device is a double heterojunction based on a GaAs substrate. (b) Top view of the photonic crystal layer, which has a hexagonal lattice, with period Λ, thickness t and rod diameter D

7.2.1 Optimization of grating parameters

A three-dimensional model based on rigorous coupled wave analysis (RCWA) was utilized to optimize the performance of the grating design.[2] The basic theory can be found in the reference [79]. The simulated device structure used in this model is described in the previous section, excluding the metallic contact pads. The optical properties (refractive index n and extinction coefficient κ) for all the materials are quoted from Ref. [29]. The simulation is performed at the central emission wavelength, which is 870 nm corresponding to the bandgap of GaAs ($E_g = 1.43$ eV). A monochromic dipole is placed in the middle of the intrinsic GaAs layer and the emitting field intensity on top of the grating layer is integrated over all angles to calculate the extraction efficiency. Unlike nitride based semiconductor, GaAs has a zinc blende structure, which leads to an isotropic spontaneous emission. Therefore, the overall extraction efficiency is averaged over different dipole orientations and dipole positions with respect to the grating unit cell.

We show that the structure and optical parameters of the gratings (refractive index n, grating period Λ, cylinder diameter D and thickness t in Figure 7-1) can significantly impact the light extraction efficiency. Here we assume the grating filling area ratio is 1:1, i.e., $D = 0.74\Lambda$, and study the impact of varying Λ and t. To quantify the effect of grating index contrast, we simulated two types of gratings, amorphous silicon (a-Si) in air matrix and silicon dioxide (SiO_2) in air matrix. Figure 7-2 plots the relative LED efficiency enhancement as functions of Λ and t for both types of gratings. Figure 7-2(a) reveals that when we choose appropriate values (Λ and t) for the a-Si / air grating, strong light extraction effect appears and the LED performance is enhanced. According to the simulation, the optimized design corresponds to $\Lambda = 500$ nm and $t = 200$ nm, where an enhancement factor of up to 70% can be achieved. Although the SiO_2 / air grating has a similar optimized region ($\Lambda = 600$ nm and $t = 250$ nm), the optimal enhancement factor is much lower (about 18%). This suggests that the a-Si / air grating is very effective in enhancing light extraction, because of the high index contrast (4.0 versus 1.0) of this system as well as the transparency of a-Si in the near-infrared wavelength range. In comparison, the optimal enhancement is far less significant in the SiO_2 / air grating design (Figure 7-2(b)) due to the much lower index contrast (1.4 versus 1.0).

[2]The software can be downloaded from `http://camfr.sourceforge.net/`.

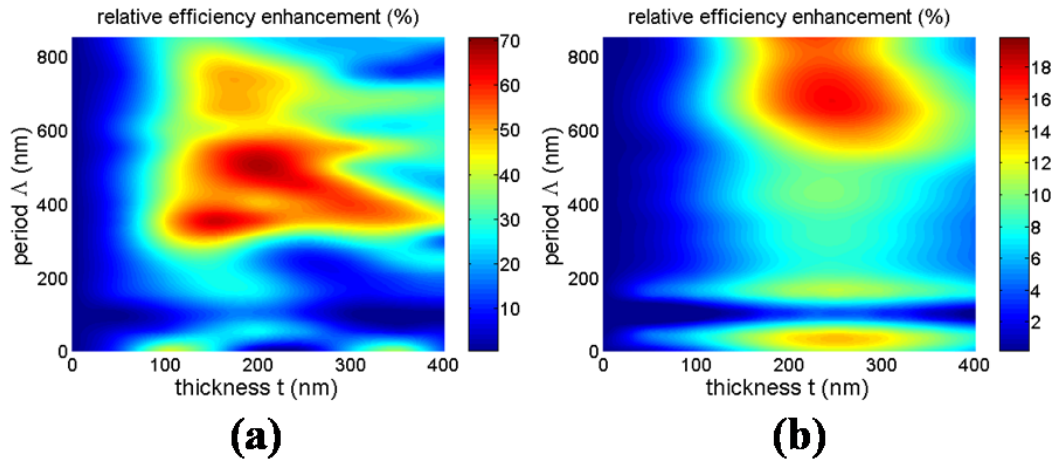

Figure 7-2: Plot of the relative efficiency increase after introducing the grating layer for light extraction, as a function of grating period Λ and thickness t. The performance is compared with the planar device without the grating. Grating structure: (a) a-Si hexagonal pattern in air matrix; (b) SiO_2 hexagonal pattern in air matrix.

7.2.2 Calculation of far field emission profiles

To further understand the effects of high-index-contrast grating, we analyzed the far field emission pattern for the LED structure with the optimal grating parameters (a-Si / air grating with $\Lambda = 500$ nm and $t = 200$ nm). Figure 7-3 compares the contour plots for the LEDs with and without grating in the reciprocal space. In Figure 7-3(a) and Figure 7-3(b), k_x and k_y are parallel to the device plane, and each point (k_x, k_y) corresponds to a specific emission angle θ in the far field,

$$\sin\theta = \frac{\sqrt{k_x^2 + k_y^2}}{2\pi/\lambda_0} = \frac{\sqrt{k_x^2 + k_y^2}}{k_0} \tag{7.1}$$

The averaged angular dependences are plotted in Figure 7-3(c). As expected, the planar device reveals a Lambertian emission pattern with a maximum in the normal direction, since GaAs has an isotropic spontaneous emission. For the LED with grating, the non-Lambertian behavior is caused by the outcoupling of the guided modes due to diffraction, which also explains the improvement of extraction efficiency. Because the results are averaged among dipoles emitting at different directions and combining both TE and TM modes, no significantly sharp peaks can be observed as mentioned in some references [78, 80].

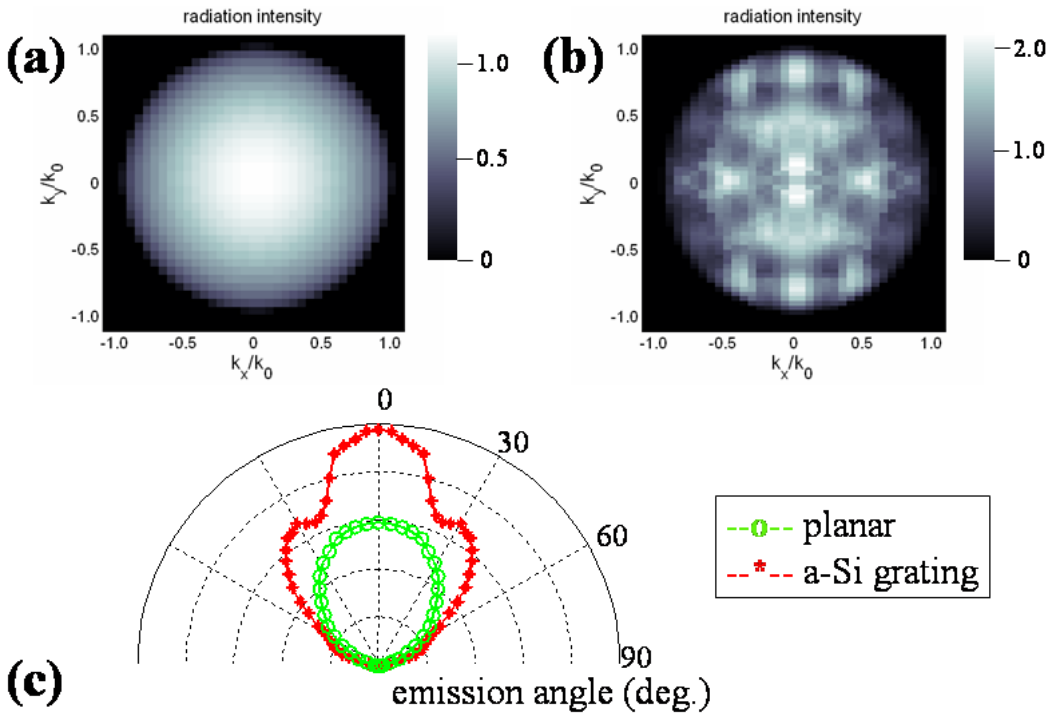

Figure 7-3: Simulated far-field emission pattern at a wavelength of 870 nm. (a) Planar LED without grating on top, which shows a Lambertian pattern. (b) LED with a periodic a-Si / air grating of optimized parameters ($\Lambda = 500$ nm and $t = 200$ nm), which shows a non-Lambertian pattern. (c) Averaged angular dependence of light emission for devices without (green) and with (red) a-Si grating. The normalized intensity has an arbitrary unit.

7.3 Experimental results

7.3.1 Device structure and fabrication

For demonstration, we use conventional GaAs based LEDs. The process flow of making such devices is illustrated in Figure 7-4:

1. A double heterojunction is grown on an n-type GaAs substrate by Metal-Organic Chemical Vapor Deposition (MOCVD). The detailed structure (from bottom to top) is 1 μm n-$Al_{0.3}Ga_{0.7}As$ (Si doping, $n = 4 \times 10^{18}$ cm^{-3}), 0.12 μm intrinsic GaAs and 1 μm p-$Al_{0.3}Ga_{0.7}As$ (Zn doping, $p = 4 \times 10^{18}$ cm^{-3}). Subsequently, a thin p-GaAs layer (0.2 μm, Zn doping, $p = 1 \times 10^{19}$ cm^{-3}) is grown on top of the p-i-n junction as a protecting layer to prevent the $Al_{0.3}Ga_{0.7}As$ layer from oxidation and enable a better ohmic contact.

2. A mesa structure is defined by wet etching in a mixed solution of 30% H_2O_2 / 85% H_3PO_4 / H_2O (volume ratio = 1:3:25). At room temperature, the etch rate is about 200 nm/min. Final etch depth is around 4 μm. The size of the mesa is defined by the size of the photomask, which varies from 50 μm to 5000 μm.

3. Ideal ohmic contacts on the n-GaAs and p-GaAs are formed by evaporating 20 nm Ni / 30 nm Ge / 200 nm Au and 20 nm Ni / 30 nm Zn / 200 nm Au, followed by rapid thermal annealing (at 400 °C for 40 s). The above procedures create the reference LED device without light extraction structures.

4. To improve the light extraction efficiency, grating structures are fabricated on top of the LEDs. The process for making gratings are mentioned in the following sections.

The current-voltage (IV) characteristic of a fabricated LED device (without grating) is shown in Figure 7-5. The p-i-n junction shows a typical diode response, with a turn-on voltage at around 1.5 V, which is close to the bandgap of GaAs ($E_g = 1.43$ eV). When the applied voltage is greater than the turn-on voltage, light emission can be clearly observed through a near-infrared microscope, as illustrated in the insets.

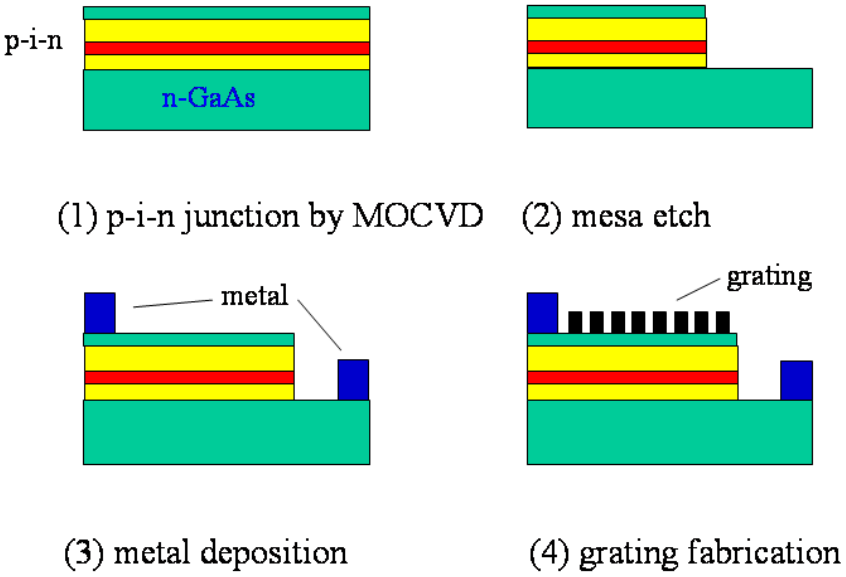

Figure 7-4: Process flow for fabricating the GaAs based LEDs.

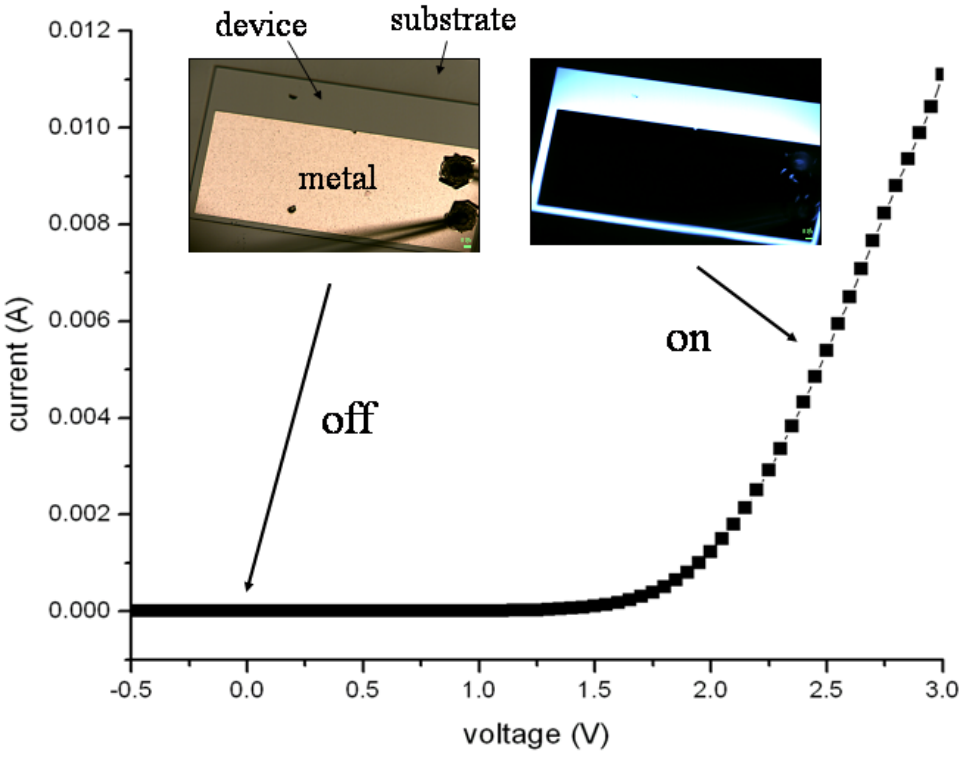

Figure 7-5: Performances of the fabricated GaAs based LEDs.

7.3.2 Self-assembled light extraction structures

The above simulation results predict and optimize the performance of devices with a perfectly periodic texture. To fabricate the optimized sub-micron light extraction structure on top of the LED devices, one needs to resort to lithographic techniques. If the light extraction structure only has short range order, the device performances will deviate from the simulations because of the average effect due to imperfection. However, the influences of different index contrast can still be observable in those short-range-order structures.

To demonstrate the effect of refractive index contrast on extraction efficiency, we use low-cost, self-assembled anodic aluminum oxide (AAO) templates as an alternative to high resolution lithography, similar to the way we fabricate light trapping structures for solar cells. As we demonstrated in the above simulations, the low index contrast between air and alumina (1.0 versus 1.7) will significantly limit the extraction enhancement. Also, the electrolyte used in the anodization process can severely degrade the active device by introducing surface defects. To overcome these challenges of directly using AAO for light extraction, we used AAO as a template. Details of the process can be referenced in Chapter 3 as well as Ref. [44]. By a two-step anodization at a constant DC voltage of 200 V in a 1.0 mol/L citric acid solution, self-organized AAO with a uniform pore distribution can be fabricated and used as a deposition mask. Figure 7-6(a) shows a SEM image of a fabricated AAO membrane with a period of about 500 nm and thickness of nearly 1 μm. Through this thin porous membrane, various materials including semiconductors and metals can be deposited via simple thermal or electron beam evaporation. As we designed in the previous section, 200 nm a-Si and SiO_2 are deposited on top of the GaAs LEDs respectively, forming the optimal designed light extraction structure. Shown in the AFM images (Figure 7-6(b) and Figure 7-6(c)), the deposited a-Si and SiO_2 pattern have very similar morphology, directly replicating the near hexagonal AAO pore arrays.

7.3.3 Device characterization

The electroluminescence (EL) performances of LEDs with different light extraction structures were measured using an optical multimeter (Ando AQ2140). A multimode fiber (100 μm diameter, NA = 0.28) was placed above the devices to collect the emitted photons from the surface. The light intensity-current (LI) characteristics are shown in Figure 7-7(a).

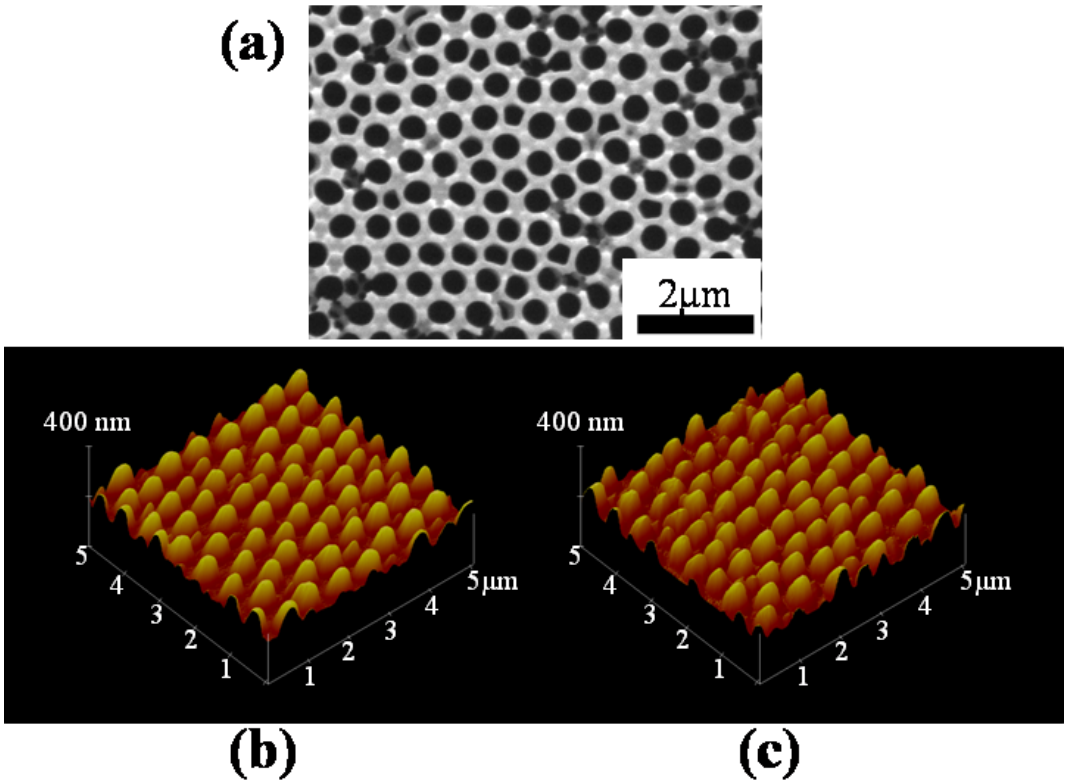

Figure 7-6: (a) SEM image of the anodized porous alumina membrane utilized as a deposition mask; (b) AFM image of the deposited a-Si pattern; (c) AFM image of the deposited SiO_2 pattern.

The slight non-linear behavior is due to some feedback mechanisms, causing a small portion of stimulated emission [81]. It can be clearly seen that the emission intensity is significantly higher if the designed grating is used as a light extraction structure. Compared to the planar device without any light extraction structure, the device with a-Si grating shows a relative efficiency improvement of 27%, while the SiO_2 grating only achieves 7.3% relative increase. These results are further confirmed by the emission spectra measured under a current of 20 mA by an optical spectrum analyzer (Ando AQ6315A). As illustrated in Figure 7-7(b), all the spectra peak at 870 nm, with a full width at half-maximum (FWHM) of 26 nm. The LI curves and emission spectra clearly reveal that the grating with higher index contrast entails higher performance for light extraction, which agrees well with our numerical predictions. Other approaches show a 130% increase in GaN devices by surface roughening [82] and 39% increase in AlGaInP directly using the low-index AAO [83]. The differences in materials systems (GaAs vs. GaN or AlGaInP) and device configurations (bulk vs. thin film) lead to lower efficiency improvements in our case. However, our approach can be implemented in those different systems and will yield better performances which scale with index-contrast and structural parameters according to our model.

Figure 7-7(c) shows the angular dependence of emission for the devices with and without a-Si grating. In the measurement, the devices are mounted on a goniometer which can rotate 90 degrees. Unexpectedly, both the devices show a Lambertian emission pattern, which does not fully agree with the simulation predictions shown in Figure 7-3(c). This is mainly due to the imperfection of the fabricated grating. As seen in the SEM image of AAO membrane (Figure 7-6(a)), the pore distribution only exhibits short-range order. In addition, the AFM images of the deposited a-Si and SiO_2 indicate we obtained a cone-shaped array. Therefore, the self-assembled approach causes a deviation from the ideal hexagonal array of cylinders, thus inducing random scattering and forming the near-Lambertian emission pattern [84].

Although the above results are obtained from GaAs based near-IR LEDs, the proposed design can also be applied for light extraction in LEDs emitting at other spectral ranges. For visible LEDs based on nitride or organic semiconductors, the simulation and fabrication methods we utilized here are still applicable, while the structural parameters should be altered to accommodate the target wavelength. The AAO template has controllable feature sizes, which can be manipulated by varying experimental conditions like applied voltage and anodization time Chapter 3. It should be noted that a-Si becomes strongly absorptive at

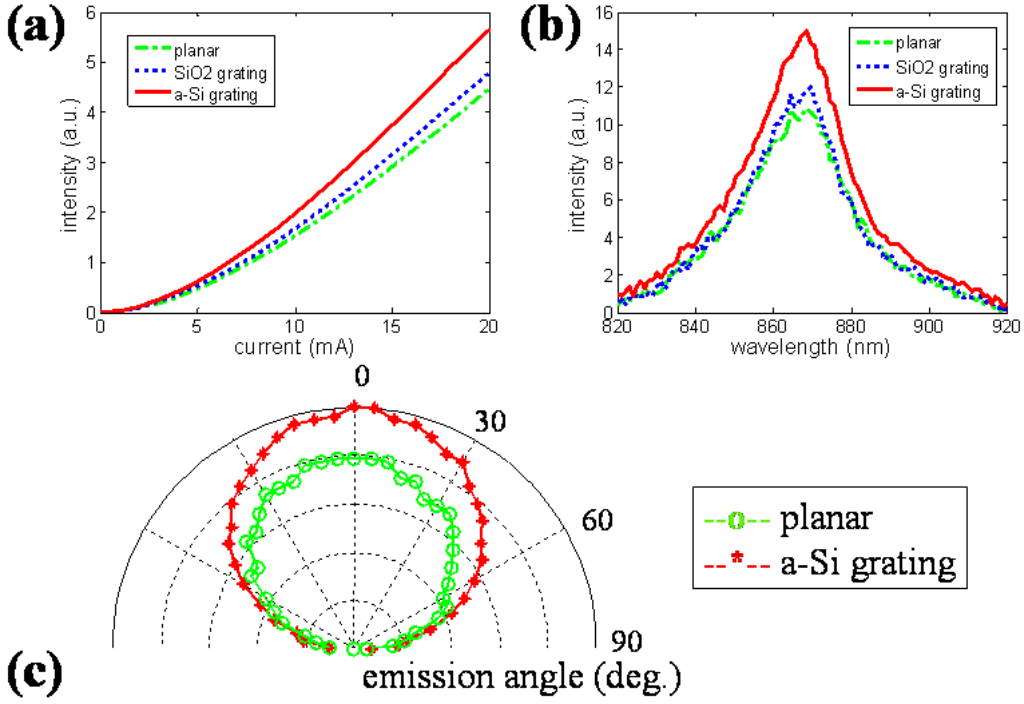

Figure 7-7: Performances for LED devices with various top structures: the planar LED without grating (green), the LED with SiO_2 grating (blue) and the LED with a-Si grating (red). (a) Light intensity-current (L-I) curves; (b) Emission spectra measured at current of 20 mA. It can be observed that the LED with a-Si grating shows the highest emission intensity, thus obtaining the highest efficiency. (c) Angular resolved measurement of light emission for the planar LED and the one with a-Si grating. The normalized intensity has an arbitrary unit.

visible wavelengths ($\lambda < 700$ nm). Therefore, other materials should be exploited to make the self assembled pattern. Possible candidates can be SiC and ZnS, both of which have high refractive indices as well as low absorption coefficients in the visible range [29].

7.4 Conclusion

The self-assembled light extraction structure is integrated for LED efficiency enhancement. Based on numerical simulations, we systematically investigate the impact of grating parameters and materials selection on the light extraction. We show that high-index gratings are far more effective in light extraction improvement compared to their low-index counterpart. The optimized structures are integrated on GaAs based LEDs by using self-assembled AAO membranes as a template, which acts as an effective and low-cost alternative to lithographic fabrications. The LED device with the optimized high-index-contrast a-Si grating yield a 27% improvement in emission intensity. The effects of different index contrasts are verified by comparing the performances of gratings made from a-Si and SiO_2. Unlike the simulation results, the device with fabricated a-Si grating showed a Lambertian emission pattern, which is due to the non-ideality of the periodicity. By proper structure design and materials selection, these approaches could also provide a guideline for efficiency enhancement in nitride and organic based LEDs.

Chapter 8

Summary and future work

8.1 Summary

Thin-film Si solar cells are promising candidates to supply world increasing energy demand with renewable and clean energy sources. In Chapter 1, we stress the importance of solar energy, introduce the photovoltaic effect, and discuss the motivations of using thin-film Si solar cells for solar energy utilization. We identify light trapping as one of the key challenges for achieving highly efficient thin-film Si solar cells. Several existing light trapping schemes are presented and compared.

Chapter 2 discusses a previously reported PC based light trapping structure combining a DBR and a grating layer, which can induce light scattering and reflection and significantly improve the thin-film Si absorption. Using photonic band theories and numerical analysis, we elucidate the light trapping mechanism of the PC structure by discovering that total internal reflection occurs at the bottom surface of the DBR. The combined photonic structure with grating and DBR reveals an unusual way of achieving light scattering and reflection, unlike the conventional reflectors based on metals or photonic crystals with a complete bandgap. Based on this discovery, the effects of DBR bilayers on cells with and without gratings are investigated and compared. We present the design rules and determine the suitable materials constitutes the PC structures are a-Si and SiO_2.

In Chapter 3, we develop a self-assembled method by using AAO for low-cost grating fabrication. We demonstrate that the AAO structures can be well controlled and adjusted in the electrochemical process. By using two step anodization, highly organized pore distribution can be obtained. The period of AAO structures can be accurately determined

through FFT analysis. The self-organized AAO material can also be used as a template to fabricate ordered patterns made of other materials like a-Si and Ag. Numerical simulations confirm that the slightly disturbed self-assembled pattern can provide a similar or even higher performance compared to a perfectly periodic pattern.

In Chapter 4 and Chapter 5, we apply the light trapping concepts of the PC structures on thick Si wafer based photoconductors and thin-film μc-Si solar cells. The gratings are fabricated either by directly anodizing Al films or using AAO membranes as templates for pattern transfer. The optimal grating structural parameters are determined by numerical simulations, and more than 30% relative efficiency improvement is predicted for optimal PC structures in 1.5 μm thick μc-Si solar cells. EQE measurements clearly reveal that the photon absorption is greatly improved in the near-IR spectral range for cells with optimal PC structures, with an efficiency enhancement up to 20%.

Chapter 6 explores the fundamental performance limits for thin-film Si solar cells. We consider a variety of texture designs, such as simple periodic gratings and commercial random textures. Furthermore, we develop a deterministic method to optimize arbitrary irregular periodic textures with combined multiple periods by multi-parameter optimization. For normal incidence, our optimized surface texture in two dimensions (2D) exhibits a considerably larger absorption enhancement than the classical Lambertian result and exceeding by almost 50% a recent generalization of Lambertian model for periodic structures in finite spectral range. We further modify the conventional Shockley-Queisser limit to predict the ultimate efficiency for thin-film Si solar cells. Considering non-radiative recombination and advanced light trapping, we concludes that a 1.5 μm Si cell with more than 20% efficiency is achievable under one sun illumination.

In Chapter 7, we further adapt the design and fabrication methodologies on another important energy device—the light-emitting diode (LED). We implement our designed photonic structure on a GaAs double heterojunction LED. We numerically explore the effects of the structural parameters on the device performances, followed by fabrication through the self-assembled AAO as a template. Device simulation and experimental results indicate that an optimized high-index-contrast (a-Si / air) grating obtains a much larger efficiency increase than using a low-index SiO_2 grating, providing an effective and low-cost method for improving LED efficiency.

8.2 Future work

The ultimate goal in the photovoltaic area is to provide a solar cell technology that can meet the terawatts scale energy demand and approach the ideal efficiency we predict in Chapter 6. Thin-film Si solar cells are promising candidates, but there are some aspects we can further explore in the future:

1. Different thin-film Si technologies can be evaluated and compared. a-Si and μc-Si solar cells benefit from low-cost fabrications but suffer from relatively low efficiency due to light trapping and high defect level. Double junction a-Si/μc-Si cells and even three junction a-Si/μc-Si/a-Ge cells [48] can more efficiently harness solar energy and provide higher ultimate efficiencies. Another interesting direction is to utilize special techniques like layer transfer approaches [65] to fabricate thin-film single crystalline Si cells which have the ideal device quality and can potentially approach the theoretical efficiency limit.

2. The self-assembled AAO technology should be optimized and extended to wafer size cell fabrication. Other nano-texturing approaches can also be explored, such as nanosphere lithography [7], soft imprint [85] and nano molding [86]. Efficiency-cost models should be developed to evaluate different techniques.

3. The optimization methods we establish in Chapter 6 can be adapted for real 3D device simulation and optimization. Although the Lambertian $4n^2$ limit is difficult to exceed for isotropic incidence, we can design structures that can trade off between efficiency enhancement and angular sensitivity. The optimized multiscale photonic structures can be fabricated by soft imprint techniques. Also, the interference lithography [87] will be another optional method, which can be used to fabricate gratings with multiple periods by combining interference beams with different wavelengths.

4. Novel light trapping schemes, including plasmonic structures [88], spheres with whispering gallery modes [89] and micro/nano wires [66], can be explored numerically and experimentally, which can possibly exceed the conventional Lambertian limit.

Appendix A

Light trapping limit

In this appendix, we summarize the theoretical derivations of light trapping limit for Lambertian textures. In addition, the results can be modified when the incident angles are restricted. Original analysis can be found in the literatures [9, 52, 90, 91].

A.1 Geometrical optics derivation

In this section, we investigate the light trapping performance for randomly textured (Lambertian) surfaces. Consider a dielectric layer illustrated in Figure A-1. Here we assume the device is two-dimensional (2D) so that the structure is uniform in y direction in Figure A-1, and the light is incident in the xz plane.

We can zoom into a small area element dA. I_{inc} is the incident power on this area dA, with an incident angle ϕ. If the transmission coefficient is $T_{inc}(\phi)$, the radiation power into the device is $T_{inc}(\phi)I_{inc}$. Inside the device, the internal intensity of area dA is defined as I_{int}. If internal radiation is isotropic due to the surface scattering, such a surface is called Lambertian surface. Let B_{int} be the internal intensity per unit angle $d\theta$. Then we can get

$$\begin{aligned} I_{int} &= \int B_{int} \cos\theta d\theta \\ &= 2\int_{-\frac{\pi}{2}}^{\frac{\pi}{2}} B_{int} \cos\theta d\theta \\ &= 4B_{int} \end{aligned} \tag{A.1}$$

Due to the total internal reflection, only a small fraction of the internal radiation can escape

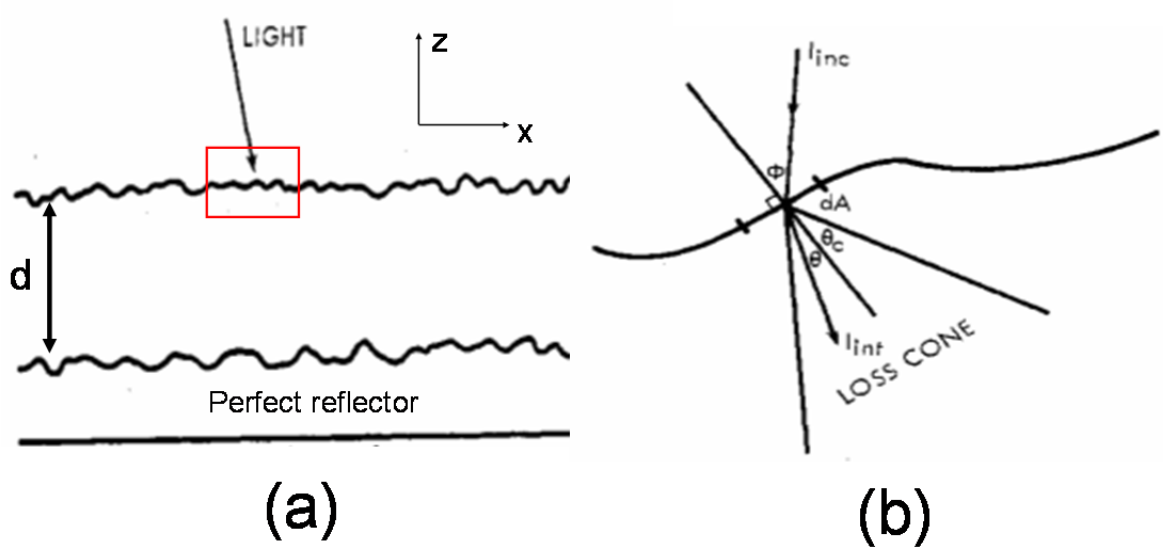

Figure A-1: (a) A schematic of device structure. The light is incident from air ($n = 1.0$) on a dielectric slab (index n) with Lambertian surfaces on both sides. A perfect reflector is in the backside so that light can only escape from the top surface; (b) The balance formed between the incoming and outgoing radiation.

from the top surface. The escaping intensity is

$$\begin{aligned} I_{esc} &= \int_{-\theta_c}^{\theta_c} B_{int} T_{esc}(\theta) \cos\theta d\theta \\ &= 2 \times \frac{I_{int}}{4} \overline{T_{esc}} \sin\theta_c \\ &= \frac{1}{2n} I_{int} \overline{T_{esc}} \end{aligned} \tag{A.2}$$

Here we use $\sin\theta_c = \frac{1}{n}$, where θ_c is the critical angle for total internal reflection. Since all the materials are lossless, the energy conservation requires that the escaping intensity I_{esc} should be balanced by the incoming intensity $T_{inc}(\phi) I_{inc}$. Therefore,

$$\frac{1}{2n} I_{int} \overline{T_{esc}} = T_{inc}(\phi) I_{inc} \tag{A.3}$$

$$I_{int} = 2n \frac{T_{inc}(\phi)}{\overline{T_{esc}}} I_{inc} \approx 2n I_{inc} \tag{A.4}$$

Because the front surface is randomly textured, the incident angle ϕ is equally distributed at all the values. Therefore, the incident intensity is also isotropic and we can get $T_{inc}(\phi) \approx \overline{T_{esc}}$ above.

If the material is weakly absorptive, then loss is involved in the device. However, Equation A.3 still holds since only a small fraction of light is trapped inside and get absorbed. Therefore, the conclusion in Equation A.4 is still valid, and the bulk absorption can be expressed by

$$\begin{aligned} &\iint B_{int}(1-e^{-\alpha d})dAd\theta \\ =&\int_{-\pi}^{\pi}\int \frac{I_{int}}{4}\alpha d dAd\theta \\ =&\frac{\pi}{2}\alpha V I_{int} \end{aligned} \tag{A.5}$$

where α is the absorption coefficient, d is the thickness ($\alpha d \sim 0$) and V is the volume of the dielectric material.

If we compare the result Equation A.5 with the absorption of a single pass

$$\begin{aligned} &\int I_{inc}(1-e^{-\alpha d})dA \\ =&\int I_{inc}\alpha d dA \\ =&\alpha V I_{inc} \end{aligned} \tag{A.6}$$

we can obtain the enhancement factor for a Lambertian texture

$$F = \frac{\frac{\pi}{2}\alpha V I_{int}}{\alpha V I_{inc}} = \pi n \tag{A.7}$$

The above calculations could be applied for a three-dimensional (3D) structure, where we just need to replace the plane angle $d\theta$ with solid angle $d\Omega$. In this case, Yablonovitch and Cody [90] proved that the enhancement factor is

$$F = 4n^2 \tag{A.8}$$

A.2 Wave optics derivation

Fundamentally, light lines are described as electromagnetic waves, whose behaviors can be fully understood by Maxwell equations. The light trapping limit can also be investigated through the electromagnetic theory [9]. The absorption of a dielectric slab mentioned in Figure A-1 can be considered as a combination of multiple resonances. When the light is incident on the device, it is either to be absorbed because of the intrinsic material loss with

a decay rate

$$\gamma_i = \frac{c}{n}\alpha \tag{A.9}$$

or coupled out through the leaky modes (with modes number N and decay rate γ_e for each mode). Based on the Lambertian assumption, the outgoing radiation is isotropic so γ_e is invariant for all the modes. If we assume periodic boundary condition and the longitudinal size is L, we can get

$$N_{2D} = \frac{2k_0}{2\pi/L} = \frac{2L}{\lambda} \tag{A.10}$$

for a 2D structure, and

$$N_{3D} = \frac{\pi k_0^2}{(2\pi/L)^2} = \frac{\pi L^2}{\lambda^2} \tag{A.11}$$

for a 3D structure.

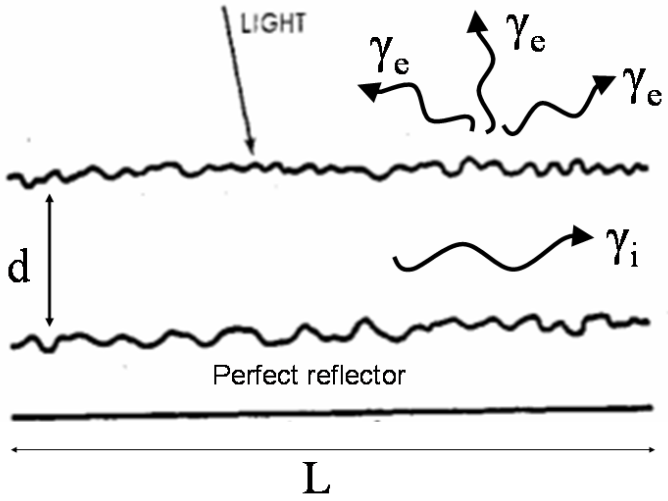

Figure A-2: A schematic of device structure, which is identical to Figure A-1(a).

According to the temporal coupled mode theory [92], the absorption spectrum of an individual resonance can be represented by a Lorenztian function

$$A(\omega) = \frac{\gamma_i \gamma_e}{(\omega - \omega_0)^2 + (\gamma_i + N\gamma_e)^2/4} \tag{A.12}$$

where ω_0 is the resonant frequency. The averaged absorption in a frequency range $\Delta\omega$ is

$$\frac{\int_{-\infty}^{+\infty} A(\omega)d\omega}{\Delta\omega} = \frac{2\pi}{\Delta\omega}\frac{\gamma_i}{N + \gamma_i/\gamma_e} \approx \frac{2\pi\gamma_i}{N\Delta\omega} \tag{A.13}$$

since the intrinsic absorption is weak ($\gamma_i \ll \gamma_e$). If there are M resonances in the frequency range $\Delta\omega$, the overall averaged absorption is

$$\frac{2\pi\gamma_i}{N\Delta\omega}M \tag{A.14}$$

M is determined by the optical density of states (DOS). For 2D structure,

$$\begin{aligned} M_{2D} &= \mathrm{DOS}_{2\mathrm{D}}\Delta\omega \\ &= \frac{\partial}{\partial\omega}\left(\frac{\pi k_0^2}{(\frac{2\pi}{L})(\frac{2\pi}{d})}\right)\Delta\omega \\ &= \frac{2\pi n^2\omega}{c^2}\left(\frac{L}{2\pi}\right)\left(\frac{d}{2\pi}\right)\Delta\omega \end{aligned} \tag{A.15}$$

and for 3D structure,

$$\begin{aligned} M_{3D} &= \mathrm{DOS}_{3\mathrm{D}}\Delta\omega \\ &= \frac{\partial}{\partial\omega}\left(\frac{\frac{4}{3}\pi k_0^3}{(\frac{2\pi}{L})(\frac{2\pi}{L})(\frac{2\pi}{d})}\right)\Delta\omega \\ &= \frac{4\pi n^3\omega^2}{c^3}\left(\frac{L}{2\pi}\right)\left(\frac{L}{2\pi}\right)\left(\frac{d}{2\pi}\right)\Delta\omega \end{aligned} \tag{A.16}$$

Combining Equation A.9, Equation A.10, Equation A.11, Equation A.15 and Equation A.16 with Equation A.14, we can get the overall averaged absorption is,

$$A_{2D} = \pi n\alpha d \tag{A.17}$$

or

$$A_{3D} = 4n^2\alpha d \tag{A.18}$$

Therefore, compared to the single pass absorption αd, the enhancement factor is πn and $4n^2$ for 2D and 3D structures, respectively. These are exactly the same results as we obtain in section A.1 using geometrical optics.

A.3 Results with restricted angles

The above derivations (section A.1 and section A.2) are based on the assumption that the incident light is isotropic. In other words, Equation A.7 and Equation A.8 can be more strictly written as

$$\overline{F}_{2D} = \frac{\int_{-\frac{\pi}{2}}^{\frac{\pi}{2}} d\theta F(\theta)\cos\theta\sin\theta}{\int_{-\frac{\pi}{2}}^{\frac{\pi}{2}} d\theta\cos\theta\sin\theta} = \pi n \tag{A.19}$$

$$\overline{F}_{3D} = \frac{\int_0^{2\pi} d\varphi \int_0^{\frac{\pi}{2}} d\theta F(\theta)\cos\theta\sin\theta}{\int_0^{2\pi} d\varphi \int_0^{\frac{\pi}{2}} d\theta\cos\theta\sin\theta} = 4n^2 \tag{A.20}$$

with incident angle θ and azimuthal angle φ.

If the incident angles are restricted in a range $[-\theta, \theta]$, then we can set $F = 0$ outside this acceptance cone to maximize F in the acceptance cone.

$$\frac{\int_{-\theta}^{\theta} d\theta F(\theta)\cos\theta\sin\theta}{\int_{-\frac{\pi}{2}}^{\frac{\pi}{2}} d\theta\cos\theta\sin\theta} = \pi n \tag{A.21}$$

$$\frac{\int_0^{2\pi} d\varphi \int_0^{\theta} d\theta F(\theta)\cos\theta\sin\theta}{\int_0^{2\pi} d\varphi \int_0^{\frac{\pi}{2}} d\theta\cos\theta\sin\theta} = 4n^2 \tag{A.22}$$

We can get

$$F_{2D} = \frac{\pi n}{\sin\theta} \tag{A.23}$$

$$F_{3D} = \frac{4n^2}{\sin^2\theta} \tag{A.24}$$

which are consistent with the results in Ref. [52].

Appendix B

Acronyms and Abbreviations

1D, 2D, 3D One-Dimensional, Two-Dimensional, Three-Dimensional

AAO Anodic Aluminum Oxide

AFM Atomic Force Miscroscope

ARC Anti-Reflective Coating

CMOS Complementary Metal-Oxide-Semiconductor

DBR Distributed Bragg Reflector

EQE External Quantum Efficiency

FDTD Finite-Difference Time Domain

FFT Fast Fourier Transform

GRT Grating

IQE Internal Quantum Efficiency

IR Infrared

LED Light Emitting Diode

PAM Porous Alumina Membrane

PECVD Plasma-Enhanced Chemical Vapor Deposition

RCWA Rigorous Coupled-Wave Analysis

RMS Root-Mean-Square

SOI Silicon-On-Insulator

SEM Scanning Electron Microscope

TCO Transparent Conductive Oxide

TE Transverse Electric

TEM Transmission Electron Microscope

TFSC Thin-Film Solar Cell

TM Transverse Magnetic

TPC Textured Photonic Crystal

Bibliography

[1] R. Perez and M. Perez, The IEA SHC Solar Update **50**, 2 (2009).

[2] R. Castellano, Vacuum Technology and Coating **2011**.

[3] H. Keppner, J. Meier, P. Torres, D. Fischer, and A. Shah, Applied Physics A: Materials Science & Processing **69**, 169 (1999).

[4] P. Bermel, C. Luo, L. Zeng, L. C. Kimerling, and J. D. Joannopoulos, Opt. Express **15**, 16986 (2007).

[5] A. Eftekhari, *Nanostructured Materials in Electrochemistry* (WILEY-VCH, 2008).

[6] R. Dewan, M. Marinkovic, R. Noriega, S. Phadke, A. Salleo, and D. Knipp, Opt. Express **17**, 23058 (2009).

[7] J. Zhu, C.-M. Hsu, Z. Yu, S. Fan, and Y. Cui, Nano Letters **10**, 1979 (2010).

[8] J. Mutitu, S. Shi, C. Chen, T. Creazzo, A. Barnett, C. Honsberg, and D. Prather, Optics express **16**, 15238 (2008).

[9] Z. Yu, A. Raman, and S. Fan, Opt. Express **18**, A366 (2010).

[10] J. Zhao, A. Wang, and M. Green, Progress in photovoltaics: research and applications **7**, 471 (1999).

[11] G. Hayward, *BP statistical review of world energy* (British Petroleum. London, UK, 2008).

[12] S. Wenham, *Applied photovoltaics* (Earthscan/James & James, 2007).

[13] D. Almond and P. Patel, *Photothermal science and techniques* (Kluwer Academic Publishers, 1996).

[14] R. Alkire, D. Kolb, and J. Lipkowski, *Photoelectrochemical Materials and Energy Conversion Processes* (Wiley-VCH, 2011).

[15] A. Luque and S. Hegedus, *Handbook of photovoltaic science and engineering* (Wiley, 2011).

[16] K. Chopra, P. Paulson, and V. Dutta, Progress in photovoltaics: research and applications **12**, 69 (2004).

[17] J. Poortmans and V. Arkhipov, *Thin film solar cells: fabrication, characterization and applications* (John Wiley & Sons Inc, 2006).

[18] M. A. Green, K. Emery, Y. Hishikawa, W. Warta, and E. D. Dunlop, Progress in Photovoltaics: Research and Applications **19**, 565 (2011).

[19] S. Honda, H. Takakura, Y. Hamakawa, R. Muhida, T. Kawamura, T. Harano, T. Toyama, and H. Okamoto, Japanese journal of applied physics **43**, 5955 (2004).

[20] S. Hegedus and R. Kaplan, Progress in Photovoltaics: Research and Applications **10**, 257 (2002).

[21] L. Zeng, P. Bermel, Y. Yi, B. A. Alamariu, K. A. Broderick, J. Liu, C. Hong, X. Duan, J. Joannopoulos, and L. C. Kimerling, Applied Physics Letters **93**, 221105 (2008).

[22] S. Guldin, S. Huttner, M. Kolle, M. Welland, P. Muller-Buschbaum, R. Friend, U. Steiner, and N. Tetreault, Nano letters **10**, 2303 (2010).

[23] E. Yablonovitch, Journal of the Optical Society of America **72**, 899 (1982).

[24] W. Shockley and H. Queisser, Journal of Applied Physics **32**, 510 (1961).

[25] J. N. W. John D. Joannopoulos, Steven G. Johnson and R. D. Meade, *Photonic crystals: molding the flow of light* (Princeton Univ Pr, 2008).

[26] L. Rayleigh, Proceedings of the Royal Society of London. Series A **93**, 565 (1917).

[27] M. Born, E. Wolf, and A. Bhatia, *Principles of optics: electromagnetic theory of propagation, interference and diffraction of light* (Cambridge Univ Pr, 1999).

[28] S. G. Johnson and J. D. Joannopoulos, Opt. Express **8**, 173 (2001).

[29] E. Palik, *Handbook of optical constants of solids* (Academic Press, 1998).

[30] A. A. Asatryan, K. Busch, R. C. McPhedran, L. C. Botten, C. Martijn de Sterke, and N. A. Nicorovici, Phys. Rev. E **63**, 046612 (2001).

[31] A. Taflove, S. Hagness *et al.*, *Computational electrodynamics: the finite-difference time-domain method* (Artech House Boston, 2000).

[32] A. F. Oskooi, D. Roundy, M. Ibanescu, P. Bermel, J. D. Joannopoulos, and S. G. Johnson, Computer Physics Communications **181**, 687 (2010).

[33] *ASTMG173-03, Standard Tables for Reference Solar Spectral Irradiances: Direct Normal and Hemispherical on 37 degree Tilted Surface* (ASTM International, West Conshohocken, Pennsylvania, 2005).

[34] L. Zeng, *High efficiency thin film silicon solar cells with novel light trapping: principle, design and processing* (PhD Thesis, Massachusetts Institute of Technology, 2008).

[35] N.-N. Feng, J. Michel, L. Zeng, J. Liu, C.-Y. Hong, L. Kimerling, and X. Duan, Electron Devices, IEEE Transactions on **54**, 1926 (2007).

[36] P. Sheasby, R. Pinner, and S. Wernick, *The surface treatment and finishing of aluminium and its alloys*, vol. 2 (ASM International, 2001).

[37] S. Chu, K. Wada, S. Inoue, M. Isogai, Y. Katsuta, and A. Yasumori, Journal of the Electrochemical Society **153**, B384 (2006).

[38] H. Masuda, K. Yada, and A. Osaka, Japanese journal of applied physics **37**, L1340 (1998).

[39] D. Mitchell and B. Schaffer, Ultramicroscopy **103**, 319 (2005).

[40] D. Marchal and B. Deme, Journal of applied crystallography **36**, 713 (2003).

[41] X. Sheng, J. Liu, N. Coronel, A. Agarwal, J. Michel, and L. Kimerling, Photonics Technology Letters, IEEE **22**, 1394 (2010).

[42] X. Sun, J. Hu, C. Hong, J. Viens, X. Duan, R. Das, A. Agarwal, and L. Kimerling, Applied physics letters **89**, 223522 (2006).

[43] K. Libbrecht, E. Black, and C. Hirata, American Journal of Physics **71**, 1208 (2003).

[44] X. Sheng, J. Liu, I. Kozinsky, A. M. Agarwal, J. Michel, and L. C. Kimerling, Advanced Materials **23**, 843 (2011).

[45] R. Schropp and M. Zeman, *Amorphous and microcrystalline silicon solar cells: modeling, materials, and device technology* (Kluwer Academic Publishers, 1998).

[46] R. Brendel and A. Goetzberger, *Thin-film crystalline silicon solar cells* (Wiley Online Library, 2003).

[47] B. Yan, G. Yue, and S. Guha, MATERIALS RESEARCH SOCIETY SYMPOSIUM PROCEEDINGS **989**, 335 (2007).

[48] J. Yang, A. Banerjee, and S. Guha, Applied physics letters **70**, 2975 (1997).

[49] O. Berger, D. Inns, and A. Aberle, Solar energy materials and solar cells **91**, 1215 (2007).

[50] H. Sai, H. Fujiwara, M. Kondo, and Y. Kanamori, Applied Physics Letters **93**, 143501 (2008).

[51] X. Sheng, S. G. Johnson, J. Michel, and L. C. Kimerling, Opt. Express **19**, A841 (2011).

[52] P. Campbell and M. Green, Electron Devices, IEEE Transactions on **33**, 234 (1986).

[53] K. Sato, Y. Gotoh, Y. Wakayama, Y. Hayasahi, K. Adachi, and H. Nishimura, Rep. Res. Lab. Asahi Glass Co. Ltd **42**, 129 (1992).

[54] C. Heine and R. H. Morf, Appl. Opt. **34**, 2476 (1995).

[55] M. Powell, Acta Numerica **7**, 287 (1998).

[56] T. Runarsson and X. Yao, Systems, Man, and Cybernetics, Part C: Applications and Reviews, IEEE Transactions on **35**, 233 (2005).

[57] W. Chew, E. Michielssen, J. Song, and J. Jin, *Fast and efficient algorithms in computational electromagnetics* (Artech House, Inc., 2001).

[58] G. Strang, *Computational science and engineering* (Wellesley-Cambridge Press, 2007).

[59] S. Cox and D. Dobson, SIAM Journal on Applied Mathematics **59**, 2108 (1999).

[60] C. Henry, Journal of applied physics **51**, 4494 (1980).

[61] O. Miller, E. Yablonovitch, and S. Kurtz, Arxiv preprint arXiv:1106.1603 (2011).

[62] I. Schnitzer, E. Yablonovitch, C. Caneau, and T. J. Gmitter, Applied Physics Letters **62**, 131 (1993).

[63] T. Trupke, J. Zhao, A. Wang, R. Corkish, and M. Green, Applied physics letters **82**, 2996 (2003).

[64] M. Green, Progress in Photovoltaics: Research and Applications **10**, 235 (2002).

[65] J. Yoon, A. Baca, S. Park, P. Elvikis, J. Geddes, L. Li, R. Kim, J. Xiao, S. Wang, T. Kim, M. Motala, B. Ahn, E. Duoss, J. Lewis, R. Nuzzo, P. Ferreira, Y. Huang, A. Rockett, and J. Rogers, Nature Materials **7**, 907 (2008).

[66] M. Kelzenberg, D. Turner-Evans, M. Putnam, S. Boettcher, R. Briggs, J. Baek, N. Lewis, and H. Atwater, Energy and Environmental Science **4**.

[67] A. Yang, S. Moore, B. Schmidt, M. Klug, M. Lipson, and D. Erickson, Nature **457**, 71 (2009).

[68] J. Wang, J. Hu, X. Sun, A. Agarwal, and L. C. Kimerling, Opt. Lett. **35**, 742 (2010).

[69] R. Kirchain and L. Kimerling, Nature Photonics **1**, 303 (2007).

[70] X. Sheng, L. Z. Broderick, J. Hu, L. Yang, A. Eshed, E. A. Fitzgerald, J. Michel, and L. C. Kimerling, Opt. Express **19**, A701 (2011).

[71] M. R. Krames, O. B. Shchekin, R. Mueller-Mach, G. Mueller, L. Zhou, G. Harbers, and M. G. Craford, J. Display Technol. **3**, 160 (2007).

[72] E. Schubert, *Light Emitting Diodes* (Cambridge University Press, 2006).

[73] C. J. Nuese, J. J. Tietjen, J. J. Gannon, and H. F. Gossenberger, Journal of The Electrochemical Society **116**, 248 (1969).

[74] O. B. Shchekin, J. E. Epler, T. A. Trottier, T. Margalith, D. A. Steigerwald, M. O. Holcomb, P. S. Martin, and M. R. Krames, Applied Physics Letters **89**, 071109 (2006).

[75] H. S. Yang, S. Y. Han, K. H. Baik, S. J. Pearton, and F. Ren, Applied Physics Letters **86**, 102104 (2005).

[76] S. Fan, P. R. Villeneuve, J. D. Joannopoulos, and E. F. Schubert, Phys. Rev. Lett. **78**, 3294 (1997).

[77] E. Matioli, E. Rangel, M. Iza, B. Fleury, N. Pfaff, J. Speck, E. Hu, and C. Weisbuch, Applied Physics Letters **96**, 031108 (2010).

[78] J. Wierer, A. David, and M. Megens, Nature Photonics **3**, 163 (2009).

[79] D. Delbeke, P. Bienstman, R. Bockstaele, and R. Baets, Journal of the Optical Society of America A **19**, 871 (2002).

[80] C.-F. Lai, J.-Y. Chi, H.-C. Kuo, H.-H. Yen, C.-E. Lee, C.-H. Chao, W.-Y. Yeh, and T.-C. Lu, Selected Topics in Quantum Electronics, IEEE Journal of **15**, 1234 (2009).

[81] T. Egawa, Y. Niwano, K. Fujita, K. Nitatori, T. Watanabe, T. Jimbo, and M. Umeno, Japanese Journal of Applied Physics **34**, 1270 (1995).

[82] T. Fujii, Y. Gao, R. Sharma, E. L. Hu, S. P. DenBaars, and S. Nakamura, Applied Physics Letters **84**, 855 (2004).

[83] C.-C. Liu, S.-X. Lin, C.-C. Wang, K.-K. Chong, C.-I. Hung, and M.-P. Houng, Japanese Journal of Applied Physics **48**, 082102 (2009).

[84] W. Koo, S. Jeong, F. Araoka, K. Ishikawa, S. Nishimura, T. Toyooka, and H. Takezoe, Nature Photonics **4**, 222 (2010).

[85] D. Shir, J. Yoon, D. Chanda, J. Ryu, and J. Rogers, Nano letters **10**, 3041 (2010).

[86] C. Battaglia, K. Soderstrom, J. Escarré, F. Haug, D. Dominé, P. Cuony, M. Boccard, G. Bugnon, C. Denizot, M. Despeisse, F. A., and B. C., Applied Physics Letters **96**, 213504 (2010).

[87] D. Xia, Z. Ku, S. Lee, and S. Brueck, Advanced Materials **23**, 147 (2011).

[88] H. Atwater and A. Polman, Nature materials **9**, 205 (2010).

[89] J. Grandidier, D. Callahan, J. Munday, and H. Atwater, Advanced Materials **23**, 1272 (2011).

[90] E. Yablonovitch and G. Cody, Electron Devices, IEEE Transactions on **29**, 300 (1982).

[91] Z. Yu and S. Fan, Applied Physics Letters **98**, 011106 (2011).

[92] H. Haus, *Waves and fields in optoelectronics*, vol. 1 (Prentice-Hall Englewood Cliffs, NJ, 1984).